Modelling of dense stellar systems with central black holes

Samuel Richard Bonsor

Doctor of Philosophy
University of Edinburgh
2024

Declaration

I declare that this thesis has been composed solely by myself and that it has not been submitted, in whole or in part, in any previous application for a degree. Except where stated otherwise by reference or acknowledgement, the work presented is entirely my own.

(*Samuel Richard Bonsor*)

Acknowledgements

I would like to thank my supervisor Anna Lisa Varri, and Jacques Vanneste for providing me with so much support throughout my PhD. It has been a privilege to learn from you over these past years. Our meetings were often the high point of any week and without those conversations, this thesis would not have been possible.

To my friends in Britannia XIV, you were incredibly welcoming when I first arrived here and I've met so many wonderful people as a result. Whether it's at a show or training session I've always left in good spirits after spending time with you all.

Thank you as well to my old friends in TPAM. I look forward to seeing you all a little more regularly and hopefully enjoying more holidays like our trip to Iceland.

Finally, I also thank my family. You have always been there for me and I can't overstate how much your unconditional love and support has meant to me.

I count myself a very fortunate man to have so many people who have helped me over the course of this PhD.

Samuel Richard Bonsor was supported by the EPSRC Centre for Doctoral Training in Mathematical Modelling, Analysis and Computation (MAC-MIGS) funded by the UK Engineering and Physical Sciences Research Council (grant EP/S023291/1), Heriot-Watt University and the University of Edinburgh.

Lay summary

Globular clusters are large, dense collections of tens of thousands, or millions, of stars, bound together by their mutual gravity. They are also one of the main candidates as hosts of intermediate-mass black holes (IMBH). As the name suggests, these are black holes with masses higher than those formed from the collapse of individual stars, called stellar-mass black holes (typically around 10^2 times the mass of the sun), but significantly smaller than the supermassive black holes which are typically found in the centres of galaxies (typically 10^6 times the mass of the sun).

Until recently, there was no direct observational evidence of the existence of an IMBH, let alone one within a globular cluster. The recent signal GW190521, detected by the gravitational wave observatories LIGO and Virgo, is consistent with a merger of two stellar-mass black holes to leave a remnant with a mass of 150 solar masses, just within the mass range to be considered an IMBH. This is the first, and only, observation of an IMBH by direct means.

With this general lack of direct observational evidence, indirect approaches using the motion of the stars within a globular cluster are important in the search for IMBHs. In these approaches, we use macroscopic properties of the star cluster to infer the presence of the gravity of a black hole, rather than "seeing" it directly. This strategy relies on having accurate dynamical models of a globular cluster, which is the focus of this thesis.

Traditionally, globular clusters have been well-modelled as non-rotating spheres of stars. However, recent high-quality data, especially from the Hubble Space Telescope and the Gaia satellite, has allowed the determination of the motion of the stars within many globular clusters, in detail, for the first time. This has revealed that many globular clusters exhibit both significant amounts of internal rotation and anisotropy in velocity space (i.e., the fact that the random motion of stars in certain directions is larger than in others). These effects have not yet been included, in a self-consistent manner, throughout much of the literature examining the presence of IMBHs in globular clusters.

This thesis develops new families of models which include the presence of a black hole at the centre of a dense stellar system. First, we begin by placing a central mass within a commonly used model for globular clusters, the King (1966) model. Even this simplified family displays an interesting behaviour when the central mass is added by accounting for the combined gravitational potential from both the black hole and surrounding stars. We will then apply the same method to include a central mass within a rotating globular cluster.

We then conclude by examining how we can compare these models to the kind of observational data that is now available, looking to improve upon methods that do not take advantage of the fact that we now have access to the three-dimensional velocity and positions of many stars in our own Galaxy.

Abstract

The presence of a black hole in a stellar system can be inferred from its gravitational interaction with the surrounding stars. This detection approach is often the only viable one, particularly in the case of a black hole of intermediate mass embedded in a dense cluster of stars. Such a regime, which is key for numerous astrophysical open questions, is notoriously difficult to attack. This difficulty arises from a number of factors, from a challenging observational environment (large amounts of crowding, lack of gas to produce significant accretion signatures etc.), to degeneracies in the effects of various observable properties of globular clusters (mass-anisotropy degeneracy, or centrally concentrated clusters of stellar remnants for example). This thesis develops mathematical and statistical tools to address this dynamical inference problem.

First, we introduce a family of self-consistent equilibria for spherically symmetric, isotropic stellar systems with a central black hole. The family is defined by a truncated isothermal distribution function in phase space, suitably modified to allow for the presence of a central point mass. We compute self-consistent solutions of the Poisson equation for the mean-field potential, which we then characterise using matched asymptotic expansions over three nested regimes of the dimensionless parameter space. This approach reveals a sharp transition between equilibria dominated by the mass of the host stellar system or by the mass of the central black hole. A thermodynamic characterisation using caloric curves shows that the black hole-dominated equilibria populate a new branch, connected, via a first-order microcanonical phase transition, to the classic truncated isothermal spheres. We also provide a numerical implementation in Python (LoKi - Loaded King Models) for the computation of the intrinsic and projected properties of the models and the sampling from the distribution function.

This class of models is then extended to the case of a rigidly rotating star cluster. We define a distribution function taking the same functional form as the LoKi models, but with the relevant Jacobi integral as the argument. This breaks the spherical symmetry of the problem, and the resulting equilibria represent axisymmetric, isotropic configurations that contain a central black hole. The resulting Poisson equation is then solved via a spectral iteration method, based on the Legendre expansion of the density and the mean-field potential, and via matched asymptotic expansions. These models are then compared to previous rotating equilibria without a central black hole. First, we note the suppression of the maximum rotation strength that may be sustained. Second, we note a change

in the morphology of the central region of the system to become increasingly spherical as the black hole mass increases. The transitional behaviour in the properties of the equilibria observed in the LoKi models persists in the presence of non-vanishing global angular momentum, with an additional discontinuity in the caloric curve.

We then detail a framework for fitting the model parameters when discrete single-star data in configuration and velocity space is available. Specifically, we define a Bayesian approach that allows us to work with the discrete star data directly, without binning. We test this framework on the traditional King (1966) models, which do not contain any central black hole. We also present extensions to the framework to accommodate missing data. We then illustrate the difficulties in applying this methodology to the LoKi models, where we show the requirement for a better understanding of the parameter space to make further progress.

Finally, we examine the constraining power provided by the truncation in phase space employed in the King (1966) models, in conjunction with physically motivated bounds on each parameter. We note that this combination provides a considerable reduction in the admissible parameter space, compared to the bounds on the individual parameters alone. In turn, such a reduction allows for increased computational efficiency in model fitting, whether by designing a better prior for Bayesian inference, or by limiting the calculation of the likelihood function only to the optimal portions of its domain.

Data distribution

The codes used in this thesis may be found on the following Github repositories:

- Chapt. 2: https://github.com/Sbonsor/LoKi
- Chapt. 3: https://github.com/Sbonsor/RLoKi
- Chapt. 4: https://github.com/Sbonsor/LoKi-fit

Contents

Chapter 1

Introduction

Globular clusters are among the oldest stellar structures in the universe, with ages on the order of billions of years, i.e. comparable to the age of the universe itself. They consist of large collections of stars, with typical masses in the range of $M = 10^4$-10^6 times the mass of the sun ($M_\odot$). This mass is all contained in a relatively compact spherical volume with typical half-light radii in the range $r_{1/2}$ = 3-5 parsecs [1]. This results in globular clusters being very dense, and bright, stellar systems. The question of what is a globular cluster does not necessarily have as simple an answer as this, with alternative views based on the chemical properties of the population of stars (see Gratton et al. 2019 for a review) also being proposed. Further, there is an increasing body of observations indicating that the boundary between a globular cluster and other types of stellar system, particularly ultracompact dwarfs, is more blurred than originally thought (see, e.g. Fig. 1.1). However, for the purposes of this thesis, this initial view of a globular cluster will suffice. Globular clusters present as ideal test beds for our understanding of stellar dynamics in a Newtonian setting.

1.1 Kinetic description of a self-gravitating system

We will now introduce the basic concepts that we use in the dynamical modelling of a stellar system. This is only a summary, for more detail we would refer the reader to Binney & Tremaine (2008), Heggie & Hut (2003), and Ciotti (2021) from which much of the following is adapted.

1.1.1 Distribution functions in phase space

The most intuitive way to represent a self-gravitating stellar system is to treat it as a system of N point particles, the size of a star being negligible compared to the typical interstellar distance. Each star has a mass, m, and interacts with the

---

[1] The half-light radius is the radius of a sphere which contains half of the total luminosity of a stellar system. The effective radius R_e, usually used in a galactic context, has a similar interpretation as the radius of the circle on the plane of the sky which contains half of the total luminosity of a galaxy. A parsec (pc) is a unit of length corresponding to the distance at which 1 astronomical unit (the Sun-Earth distance) subtends an angle of 1 arcsecond (1/3600 of a degree). For scale, the nearest star to Earth is located at a distance of 1.3 pc, so the stellar density of a globular cluster is many times greater than that in the solar neighbourhood.

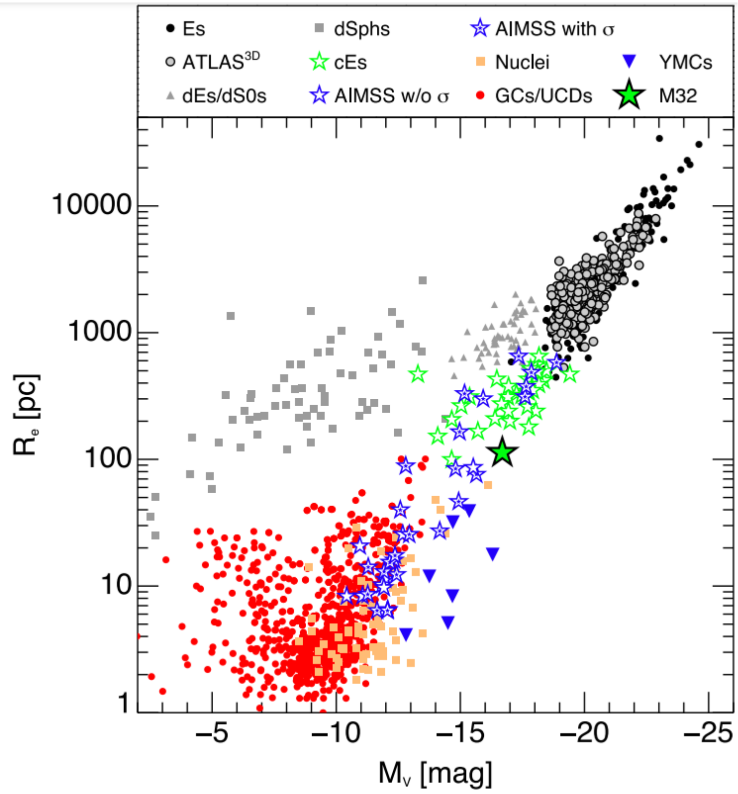

Figure 1.1: Effective radius R_e, and absolute magnitude M_V (lower values indicate a more luminous object) for selected examples of stellar systems. The red points indicate the globular clusters and ultracompact dwarfs. Orange squares indicate nuclear star clusters. The other points indicate various types of galaxies. Blue triangles indicate young massive clusters. Blue stars represent the compact stellar systems newly found in Norris et al. (2014) that span a range between star clusters and galaxies. Especially note the overlap between many of these categories in the lower left region. Taken from Norris et al. (2014).

other stars via gravity. The equations of motion governing the dynamics of the stars in the Newtonian regime are formulated as

$$\ddot{\boldsymbol{r}}_i = -mG \sum_{j=1, j\neq i}^{n} \frac{\boldsymbol{r}_i - \boldsymbol{r}_j}{\left|\boldsymbol{r}_i - \boldsymbol{r}_j\right|^3}, \tag{1.1}$$

where $\boldsymbol{r}_i$ is the position of the i^{th} star.

This is a simple formulation, but no closed-form solution exists for $N \geq 3$, which is significantly fewer than the number of stars required to model a globular cluster. A numerical solution is therefore needed, however, calculating the pairwise interactions between a large number of stars carries a high computational cost as a direct N-body calculation scales as $O(N^3)$ (Heggie & Hut, 2003). Even given such costs, with the large amount of effort put into developing ever-improved codes, and the advent of GPU computing enabling increased parallelisation, we have reached the point where direct N-body simulations with

$N = 10^6$ stars, suitable for the simulation of a globular cluster, are possible (see, e.g. Heggie 2014; Wang et al. 2015).

However, these simulations are still large undertakings and, for many purposes, are still impractical. We can instead take a different view of a stellar system. We may replace the collection of N discrete point masses with a smooth stellar density distribution, ρ, that approximates the discrete distribution of stars. The stars are then assumed to move under the influence of the mean-field gravitational potential, Φ, related to this density distribution via the Poisson equation

$$\nabla^2\Phi(\boldsymbol{r},t) = 4\pi G\rho(\boldsymbol{r},t). \tag{1.2}$$

In this way, we neglect collisional interactions between stars, as they interact only via the mean-field potential. Such a system is said to be collisionless and, provided that the timescale on which two-body encounters strongly influence the structure of the system (often referred to as the two-body relaxation time, see Heggie & Hut 2003) is sufficiently long compared to the timescale of interest, then this collisionless approximation can well describe a stellar system.

To begin modelling a collisionless stellar system, we first introduce the notion of a distribution function, $f(\boldsymbol{r},\boldsymbol{v})$. The distribution function represents the physical mass within a volume $\mathrm{d}^3\boldsymbol{r}\mathrm{d}^3\boldsymbol{v}$ centred at a point $(\boldsymbol{r},\boldsymbol{v})$ in six-dimensional phase space. Thus, if the total mass of the stellar system is M, then

$$\int f(\boldsymbol{r},\boldsymbol{v})\mathrm{d}^3\boldsymbol{r}\mathrm{d}^3\boldsymbol{v} = M. \tag{1.3}$$

This interpretation as a physical density in phase space is not unique: we could alternatively interpret the distribution function as a probability density or a number density, depending on the problem at hand.

We can then obtain the corresponding density distribution in configuration space from the distribution function by integrating over the velocity space,

$$\rho(\boldsymbol{r}) = \int f(\boldsymbol{r},\boldsymbol{v})\mathrm{d}^3\boldsymbol{v}. \tag{1.4}$$

The associated probability density on configuration space is obtained by normalising equation (1.4) as

$$p(\boldsymbol{r}) = \frac{\rho(\boldsymbol{r})}{M}. \tag{1.5}$$

By attributing a statistical interpretation to this zeroth-order velocity moment, we can define a probability density on the stellar velocities, at a fixed position, as

$$p_{\boldsymbol{r}}(\boldsymbol{v}) = \frac{f(\boldsymbol{r},\boldsymbol{v})}{p(\boldsymbol{r})}. \tag{1.6}$$

The first and second moments of the probability density (1.6) provide two further quantities of interest. First, the mean velocity at a given position

$$\bar{v}(\boldsymbol{r}) = \frac{1}{\rho(\boldsymbol{r})} \int \boldsymbol{v} f(\boldsymbol{r}, \boldsymbol{v}) \mathrm{d}^3\boldsymbol{v}. \tag{1.7}$$

Second, the components of the velocity dispersion tensor

$$\begin{aligned} \sigma_{ij}^2(\boldsymbol{r}) &= \frac{1}{\rho(\boldsymbol{r})} \int (v_i - \bar{v}_i)(v_j - \bar{v}_j) f(\boldsymbol{r}, \boldsymbol{v}) \mathrm{d}^3\boldsymbol{v}, \\ &= \overline{v_i v_j} - \bar{v}_i \bar{v}_j. \end{aligned} \tag{1.8}$$

The quantities

$$P_{ij}(\boldsymbol{r}) = p(\boldsymbol{r}) \sigma_{ij}^2(\boldsymbol{r}) \tag{1.9}$$

are the components of the pressure tensor at a given position. If the velocity dispersion tensor may be written in the form $\sigma_{ij}^2 = \sigma^2 \delta_{ij}$, then we say that the velocity dispersion is isotropic. We can define the anisotropy parameter as

$$\beta = 1 - \frac{\sigma_\theta^2 + \sigma_\phi^2}{2\sigma_r^2}, \tag{1.10}$$

where we are making use of spherical coordinates. This parameter denotes the magnitude and type of anisotropy present in velocity space. If the system is isotropic then $\sigma_\theta^2 = \sigma_\phi^2 = \sigma_r^2$, so we have $\beta = 0$. For a radially anisotropic system we have $\beta > 0$, and $\beta < 0$ denotes tangential anisotropy. The degree of velocity anisotropy present in a stellar system has a large impact on the structure and dynamics of the system; we defer further remarks about this topic until Sect. 1.3.1.

1.1.2 Collisionless Boltzmann equation

We continue by presenting the partial differential equation that governs the evolution of the distribution function in phase space. First, recall that the equations of motion in a gravitational potential, $\Phi(\boldsymbol{r}, t)$, are given by

$$\frac{\mathrm{d}\boldsymbol{r}}{\mathrm{d}t} = \boldsymbol{v}, \qquad \frac{\mathrm{d}\boldsymbol{v}}{\mathrm{d}t} = -\frac{\partial \Phi(\boldsymbol{r}, t)}{\partial \boldsymbol{r}}. \tag{1.11}$$

We also consider the equation of conservation of mass in phase space given by

$$\frac{\partial f}{\partial t} + \frac{\partial}{\partial \boldsymbol{r}} \cdot \left(f \frac{\partial \boldsymbol{r}}{\partial t} \right) + \frac{\partial}{\partial \boldsymbol{r}} \cdot \left(f \frac{\partial \boldsymbol{v}}{\partial t} \right) = 0, \tag{1.12}$$

analogous to the conservation of mass in a fluid.

Taking the relevant derivatives, and substituting equation (1.11) into equation (1.12), then provides

$$\frac{\partial f}{\partial t} + \boldsymbol{v} \cdot \frac{\partial f}{\partial \boldsymbol{r}} - \frac{\partial \Phi(\boldsymbol{r}, t)}{\partial \boldsymbol{r}} \frac{\partial f}{\partial \boldsymbol{v}} = 0. \tag{1.13}$$

Equation (1.13) is the collisionless Boltzmann equation. The right-hand side of this equation is posed to zero because we are considering a collisionless system. Modifications to the right-hand side of equation (1.13) can be made to include the influence of two-body encounters (see, e.g.Binney & Tremaine 2008, Sect. 7.2 and Ciotti 2021, Sect. 9.2.2), but for this thesis, we limit our consideration only to collisionless systems. Along with the collisionless Boltzmann equation we recall the Poisson equation (1.2), and the definition of the density in configuration space in terms of the distribution function (1.4) to write

$$\nabla^2\Phi(\boldsymbol{r},t) = 4\pi G\int f(\boldsymbol{r},\boldsymbol{v})\mathrm{d}^3\boldsymbol{v}. \tag{1.14}$$

To obtain a self-consistent model of a collisionless stellar system both the collisionless Boltzmann equation (1.13) and the Poisson equation (1.14) must be solved together. In practice, we make use of a well-known result, Jeans theorem, which enables us to work with the Poisson equation only.

1.1.3 Jeans theorem

To discuss the Jeans theorem, we must first introduce the notion of an integral of motion. These are functions of the phase space coordinates, $I(\boldsymbol{r},\boldsymbol{v})$, such that I is conserved along any orbit, i.e. for a star at any two times t_1 and t_2 the following statement holds true

$$I(\boldsymbol{r}(t_1),\boldsymbol{v}(t_1)) = I(\boldsymbol{r}(t_2),\boldsymbol{v}(t_2)). \tag{1.15}$$

As a consequence, we thus have

$$\frac{\mathrm{d}}{\mathrm{d}t}I(\boldsymbol{r}(t),\boldsymbol{v}(t)) \equiv \frac{\partial I}{\partial t} + \frac{\mathrm{d}\boldsymbol{r}}{\mathrm{d}t}\frac{\partial I}{\partial \boldsymbol{r}} + \frac{\mathrm{d}\boldsymbol{v}}{\mathrm{d}t}\frac{\partial I}{\partial \boldsymbol{v}} = 0. \tag{1.16}$$

The Jeans theorem is then stated in Binney & Tremaine (2008) as

Theorem 1 (Jeans theorem)**.** *Any steady-state solution of the collisionless Boltzmann equation depends on the phase space coordinates only through integrals of motion in the given potential, and any function of the integrals yields a steady-state solution of the collisionless Boltzmann equation.*

This theorem is crucial. If we can write down a distribution function that depends only on integrals of motion, then we are guaranteed that this distribution function solves the collisionless Boltzmann equation.

In general, orbits may have up to five integrals of motion (Binney & Tremaine 2008), but not all of them have closed-form expressions that are useful for this form of dynamical modelling. However, in many geometries, there are a handful of important quantities that are integrals of motion that can be used in this manner.

The dynamical modelling task is then to define a distribution function, as a function of integrals of motion, that well models the stellar system that we wish to describe, including any particular physical properties (intermediate-mass black holes, internal rotation, velocity anisotropy etc.). We must then solve the Poisson equation (1.14) associated with the chosen distribution function in order to obtain a self-consistent model of a stellar system.

In this thesis, we limit our consideration to two classes of distribution functions. First, in Chapt. 2 we consider distribution functions that depend only on the single-star energy, $E = v^2/2 + \Phi$, which is an integral of motion provided that the potential is time-invariant (Ciotti 2021).

In Chapt. 3, we consider a class of distribution function that is dependent on both E and J_z, where J_z is the z-component of the angular momentum. These two quantities are integrals of motion provided that the potential is time-invariant, and axisymmetric (Ciotti 2021). These choices of distribution function have large implications for the symmetries of the resulting models.

1.1.4 Symmetries of the distribution function

Let us first examine distribution functions, $f(E)$, dependent only on the single-star energy. In this case, the mean velocity (1.7) vanishes

$$\bar{\boldsymbol{v}} = \frac{1}{\rho(\boldsymbol{r})} \int \boldsymbol{v} f \left(\frac{v^2}{2} + \Phi(\boldsymbol{r}) \right) \mathrm{d}^3 \boldsymbol{v} = 0, \tag{1.17}$$

because the integrand is an odd function of the velocity and the region of integration (the entire velocity space) is symmetric about the origin.

The velocity dispersion tensor (1.8) is given by

$$\sigma_{ij}^2 = \overline{v_i v_j} = \sigma^2 \delta_{ij}, \tag{1.18}$$

where the first equality follows via equation (1.17), and the second follows via similar symmetry arguments with

$$\sigma^2 = \frac{4\pi}{3\rho(\boldsymbol{r})} \int_0^\infty v^4 f \left(\frac{v^2}{2} + \Phi(\boldsymbol{r}) \right) \mathrm{d}v. \tag{1.19}$$

Thus, these models are isotropic in velocity space. Further, we can show that an isolated, finite stellar system with a distribution function dependent only on E, must be spherically symmetric (Binney & Tremaine 2008). A set of important distribution functions in this class are truncated isothermal spheres, discussed in Sect. 1.1.5, which form the basis of the models considered in this thesis.

For distribution functions of the form $f(E, J_z)$, we assume that the potential is axisymmetric. Therefore, we guarantee that J_z is an integral of motion. Then, in cylindrical coordinates (r, z, ϕ), where $J_z = r v_\phi$, we note that the mean velocity vector is given by the following components

$$\bar{v}_r = \frac{1}{\rho(\boldsymbol{r})} \int \mathrm{d}v_r v_r \int \mathrm{d}v_z \int \mathrm{d}v_\phi f \left(\frac{v_r^2 + v_z^2 + v_\phi^2}{2}, r v_\phi \right) = 0, \tag{1.20}$$

$$\bar{v}_z = \frac{1}{\rho(\boldsymbol{r})} \int \mathrm{d}v_z v_z \int \mathrm{d}v_r \int \mathrm{d}v_\phi f \left(\frac{v_r^2 + v_z^2 + v_\phi^2}{2}, r v_\phi \right) = 0, \tag{1.21}$$

$$\bar{v}_\phi = \frac{1}{\rho(\boldsymbol{r})} \int \mathrm{d}v_\phi v_\phi \int \mathrm{d}v_r \int \mathrm{d}v_z f \left(\frac{v_r^2 + v_z^2 + v_\phi^2}{2}, r v_\phi \right), \tag{1.22}$$

where the first two equalities are motivated by symmetry arguments, as the integrands are odd functions of v_r and v_z, respectively. The mean azimuthal component may be non-vanishing. This is the case that we are primarily interested in. Such a model may be used to describe a system that displays internal rotation (see Sect. 1.3.2) as we will compute in Chapt. 3.

In cylindrical coordinates, the velocity dispersion tensor is diagonal, with components given by

$$\sigma_r^2 = \frac{1}{\rho(r,z)} \int \mathrm{d}v_r v_r^2 \int \mathrm{d}v_z \int \mathrm{d}v_\phi f \left(\frac{v_r^2 + v_z^2 + v_\phi^2}{2}, r v_\phi \right), \tag{1.23}$$

$$\sigma_z^2 = \sigma_r^2, \tag{1.24}$$

$$\sigma_\phi^2 = \frac{1}{\rho(r,z)} \int \mathrm{d}v_\phi (v_\phi - \bar{v}_\phi)^2 \int \mathrm{d}v_r \int \mathrm{d}v_z f \left(\frac{v_r^2 + v_z^2 + v_\phi^2}{2}, r v_\phi \right). \tag{1.25}$$

These models are, in general, anisotropic in velocity space. In Chapt. 3, we consider stellar systems that are rigidly rotating with constant angular velocity, ω. In such a case, we further specify that the distribution function takes the form $f(E, J_z) = f(H)$, where $H = E - \omega J_z$ is the Jacobi integral (Landau & Lifshitz 1976). The Jacobi integral is itself an integral of motion for such a system (Vandervoort 1980) and in this case the velocity dispersion tensor is isotropic.

1.1.5 Truncated isothermal spheres

The inner regions of a globular cluster are expected to be approximately isothermal as a result of two-body relaxation (Heggie & Hut 2003). However, defining a distribution function as an isothermal sphere, following a Maxwellian distribution, results in a configuration with infinite extent and mass (Binney & Tremaine 2008).

A commonly used solution to this problem is to truncate (or "lower") the Maxwellian distribution for stars with energies above a certain cut-off energy, thus accounting for the fact that stars above the escape velocity for a cluster cannot remain bound to the cluster.

This class of truncated isothermal spheres contains a number of classical models for a globular cluster. These include the isotropic Prendergast & Tomer (1970a) (see also Woolley 1954), King (1966), and Wilson (1975) models defined by distribution functions of the form

$$f_{PT}(E) = Ae^{-aE}, \qquad \text{for } E \leq E_0, \tag{1.26}$$

$$f_K(E) = Ae^{-aE_0}\left[e^{-a(E-E_0)} - 1\right], \qquad \text{for } E \leq E_0, \tag{1.27}$$

$$f_{WT}(E) = Ae^{-aE_0}\left[e^{-a(E-E_0)} - 1 + a(E - E_0)\right], \qquad \text{for } E \leq E_0, \tag{1.28}$$

respectively. Here a is a velocity scale (in units of $1/\text{velocity}^2$), A provides the overall phase space normalisation (whether a physical, probability, or number density), and E_0 provides the energy truncation (per unit mass) in phase space, above which the distribution function is set to zero.

Each of these distribution functions is dependent only on the single-star energy, so the resulting models are all spherically symmetric.

In all three cases, the resulting configuration is almost isothermal in the central regions for strongly bound stars. However, the truncation prescription can have a significant impact on the structure of the system near its outskirts (see, e.g. Davoust 1977; Gieles & Zocchi 2015). In particular, as the truncation in phase space becomes smoother (see Fig. 1.2), the radial extent of the system increases, providing a shallower slope in density (see Fig. 2.19).

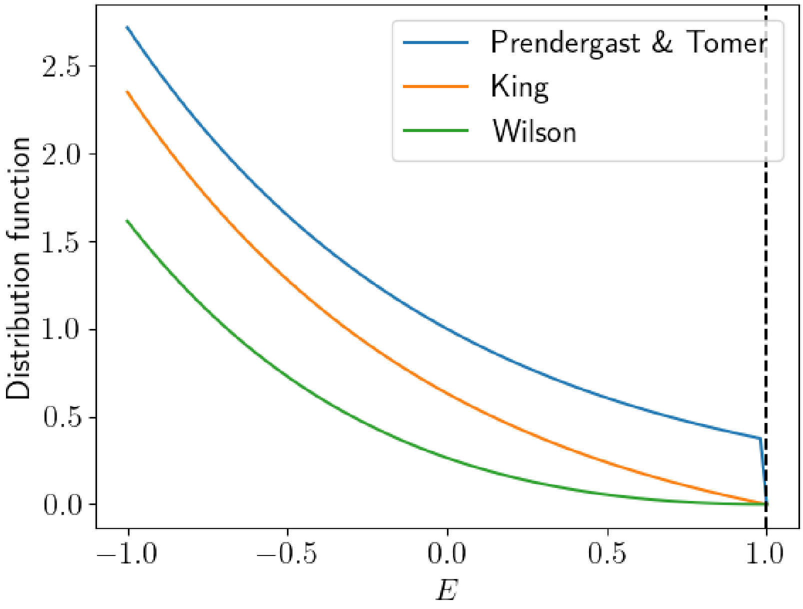

Figure 1.2: The distribution functions (1.26)-(1.28) plotted for $A = a = E_0 = 1$. Note the increasing smoothness at the truncation energy E_0 (indicated by the vertical dashed line) with the Prendergast & Tomer model being discontinuous, the King model being continuous with a discontinuous first derivative, and the Wilson model having being continuous along with its first derivative.

In this thesis, we primarily focus on the King (1966) models. We first define the dimensionless escape energy,

$$\psi(r) = a\left[E_0 - \Phi(r)\right]. \tag{1.29}$$

This definition provides that the outer radius of the system is located at a radius, r_t, such that $\psi(r_t) = 0$. The density corresponding to the distribution function is obtained via equation (1.4) as

$$\rho(\psi) = \hat{A}e^{\psi}\gamma\left(\frac{5}{2}, \psi\right) = \hat{A}\hat{\rho}(\psi), \tag{1.30}$$

where $\hat{A} = 8\sqrt{2}\pi A e^{-aE_0}/(3a^{\frac{3}{2}})$, and γ denotes the lower incomplete gamma function (Olver et al., 2022). The Poisson equation may then be expressed in a dimensionless form by introducing an appropriately scaled radial variable $\hat{r} = r/r_K$, where r_K is a scale length given by

$$r_K = \sqrt{\frac{9}{4\pi G\rho_0 a}}. \tag{1.31}$$

Here, ρ_0 denotes the density (1.30), evaluated at the origin. The Poisson equation (1.14) is then written as

$$\nabla_{\hat{r}}\psi = -9\frac{\hat{\rho}(\psi)}{\hat{\rho}_0}. \tag{1.32}$$

Boundary conditions must then be set for this equation. These are provided by setting the value of ψ and imposing regularity at the origin. The full initial value problem for the King (1966) models is thus given by

$$\nabla_{\hat{r}}\psi = -9\frac{\hat{\rho}(\psi)}{\hat{\rho}(\Psi)}, \tag{1.33}$$

$$\psi(0) = \Psi, \tag{1.34}$$

$$\psi'(0) = 0. \tag{1.35}$$

The structure of the King (1966) models is therefore determined by a single dimensionless parameter, Ψ, the central concentration, along with two physical scales a and A.

These models have been widely used to describe the structure of globular clusters (see, e.g. Peterson & King 1975; Djorgovski & Meylan 1994). They have also been extended to include many further physical ingredients such as anisotropy (Michie 1963; Gieles & Zocchi 2015), multiple mass components (Da Costa & Freeman 1976; Gunn & Griffin 1979), and internal rotation (Varri & Bertin 2012).

1.2 Intermediate-mass black holes

Intermediate-mass black holes (IMBH) are black holes that are too massive to have formed from the gravitational collapse of a single star ($M_{BH} \lesssim 10^2 M_\odot$),

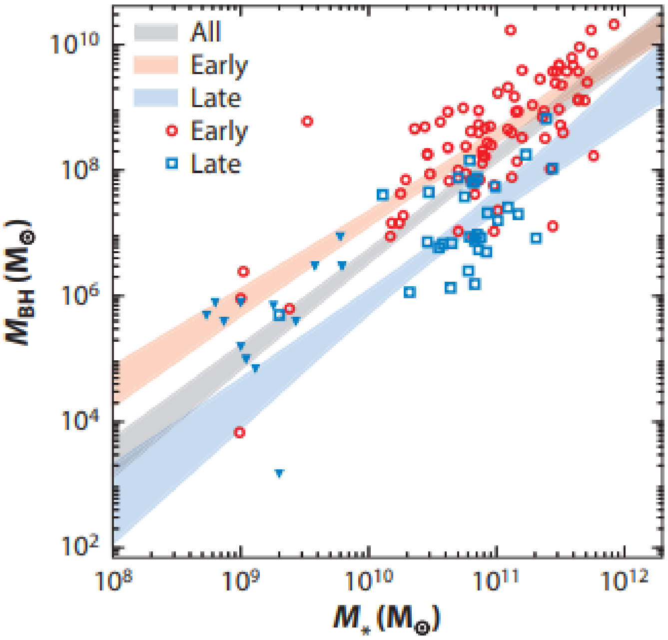

Figure 1.3: Illustration of the relationship between black hole mass, M_{BH}, and the host galaxy stellar mass, M^*. Here blue and red represent different types of galaxies, early- and late-type respectively. The shading represents the power-law fits for the $M_{BH} - M_*$ relationship, for the indicated galaxy type. Taken from Greene et al. (2020)

but not as massive as the supermassive black holes found in the centres of many galaxies ($M_{BH} \gtrsim 10^6 M_\odot$). Black holes in this mass range are often invoked as a crucial step in the formation of the supermassive black holes found at the centres of galaxies (see, e.g. Volonteri 2010, 2012). Consequently, they may be important in the understanding of galaxy evolution.

Globular clusters are one of the most promising candidates for the stellar systems hosting an IMBH. Indeed, well-established scaling laws correlating the mass of the black holes to several properties of the host stellar systems (see Fig. 1.3) are often extrapolated into the IMBH mass range (for a recent review of the phenomenological context, see Greene et al. 2020). In this regime, the hosts may be expected to have characteristics comparable to several Galactic and extragalactic globular star clusters. Further, several theoretical formation scenarios for IMBHs in globular clusters have been proposed, broadly falling into two classes of process. First, a fast process, where runaway growth via stellar collisions in the dense central regions of a globular cluster may lead to the formation of an IMBH (see Portegies Zwart et al. 2004, and, more recently, Fujii et al. 2024). Second, a process of slow growth via dynamical interactions of binary systems containing a stellar-mass black hole, with other stars and binaries (see Giersz et al. 2015).

1.2.1 Modelling a central mass

Several approaches may be adopted in modelling stellar systems with a central black hole, usually striving to provide a physical interpretation of the central gradients of the surface brightness (see Fig. 1.4) and velocity dispersion profiles of the system (see Fig. 1.5), which, in the presence of a massive central object, may display various degrees of steepness.

Some of the most common methods for modelling a central mass in a globular cluster, especially within the body of current putative IMBH detections (see Sect. 1.2.2), are those based on the solutions of the Jeans equations. These are a set of equations, obtained by taking velocity moments of the collisionless Boltzmann equation (1.13), relating the observable quantities such as the density, mean velocity, and velocity dispersion tensor (Binney & Tremaine 2008). Generally, Jeans modelling-based approaches accomplish the inclusion of a central mass by first defining the underlying model of interest. This is usually a density-potential pair, a Plummer (1911) sphere for example. The potential due to a central mass is then added in superposition with the underlying potential and the resulting velocity moments are calculated via the Jeans equations. This approach enables the relatively straightforward parametrisation of many further physical characteristics, such as multiple mass components (see, e.g. Ciotti & Ziaee Lorzad 2018), velocity anisotropy (see, e.g. Cappellari 2008, 2020), and breaking of spherical symmetry (see, e.g. Ciotti et al. 2021). As a result, this velocity moments-based approach is quite popular to model the presence of a central mass within a stellar system when fitting observational data to models (see, e.g. Tremaine et al. 1994; van der Marel & Anderson 2010; Göttgens et al. 2021; Vitral et al. 2023 for a non-exhaustive list). However, there are drawbacks to this approach. First, for spherical systems, the distribution function corresponding to a particular density and potential may be obtained using Eddington's formula (Binney & Tremaine 2008). There is no guarantee that the distribution function corresponding to a given solution of the Jeans equations will be non-negative everywhere, a condition often referred to as phase-space consistency. Therefore, care should be taken that a given model is consistent with such a constraint. Second, these approaches are not self-consistent, i.e. the resulting density and potential of the combined central mass and stellar system are not solutions to the Poisson equation.

The study of the distribution function in the vicinity of a central mass is a classical one, with the landmark study of Bahcall & Wolf (1977) deriving an approximate equilibrium solution to the Fokker-Planck equation in the Keplerian approximation where a tracer density is considered around a central mass. The resulting power law distribution function takes the form $f(E) = cE^{1/4}$ and corresponds to a physical density of the form $\rho \sim r^{-7/4}$. This expectation for the structure of a system in the vicinity of a central mass has been used by Miocchi (2007) to construct a distribution function that conforms to the Bahcall & Wolf (1977) expectation for tightly bound stars near the cluster centre, and the King (1966) model for less tightly bound stars. This is one self-consistent way to include the influence of a central mass within a King (1966) model at the level of the distribution function.

One further physically motivated class of dynamical models aims to describe a stellar system in which a central black hole is allowed to grow adiabatically (see, e.g. Young 1980; Lee & Goodman 1989; Cipollina & Bertin 1994). In these models, a black hole was adiabatically grown within an isothermal sphere. The resulting density profiles near the centre of the cluster exhibited cuspy behaviour, but generally exhibited shallower central density slopes than the Bahcall & Wolf (1977) cusp, with power law densities $\rho \sim r^{-3/2}$ for low mass black holes, and a region with $\rho \sim r^{-5/2}$ for high mass black holes (Cipollina & Bertin 1994).

In this thesis, we primarily build on the work of Huntley & Saslaw (1975). They construct polytropic models of galaxies that include the influence of a central mass by retaining the same form of distribution function as the corresponding models with no central mass. The influence of the central mass is then added at the level of the Poisson equation, by modifying the boundary conditions to ensure hydrostatic equilibrium is maintained. This approach has seen success at multiple astrophysical scales in describing galaxies (Huntley & Saslaw 1975) and quasi-stars (see, e.g. Ball et al. 2011). In this thesis, we will then apply the same considerations to King (1966) models of globular clusters, providing a self-consistent methodology for the inclusion of a central black hole within a King (1966) model.

1.2.2 Observational searches for intermediate-mass black holes

The question of whether IMBHs may exist in globular clusters is still an open one, with uncontentious detections remaining elusive.

One observational approach is the direct observation of radio wave emission resulting from the accretion of gas by the IMBH. Unfortunately, globular clusters are generally gas-poor, thus making these observations extremely challenging. No positive electromagnetic detection of an IMBH within a globular cluster currently exists (see, e.g. Strader et al. 2012; Tremou et al. 2018; Wrobel & Nyland 2020).

A second possibility is the detection of gravitational waves resulting from black hole binaries merging. Searches based on gravitational wave missions offer a promising new avenue. The detection of the event GW190521 (Abbott et al. 2020) by LIGO has been interpreted as originating from a binary black hole merger in the low mass IMBH regime, and more such events are expected to follow in forthcoming LIGO observation periods, as well as from the future mission LISA. However, this field is still in its infancy.

The primary channel by which current promising IMBH candidates are identified is based on the forms of dynamical modelling introduced in Sect. 1.2.1. In these searches, the presence of an IMBH is inferred indirectly via its effect on the surrounding stars, with the presence of an IMBH having various implications for the structure of its host system. The primary observational signature is the presence of a central kinematic gradient, see Fig. 1.4 and Fig. 1.5.

The most recent data release of the astrometric observations conducted by the Gaia satellite (Gaia Collaboration et al. 2023) provides us with two-dimensional kinematic data in the plane of the sky for many Galactic globular clusters. This has allowed the community to compute velocity dispersion profiles and, for the first time, velocity anisotropy profiles in extended radial regions of several Galactic star clusters (see, e.g. Bianchini et al. 2018; Sollima et al. 2019; Cordoni

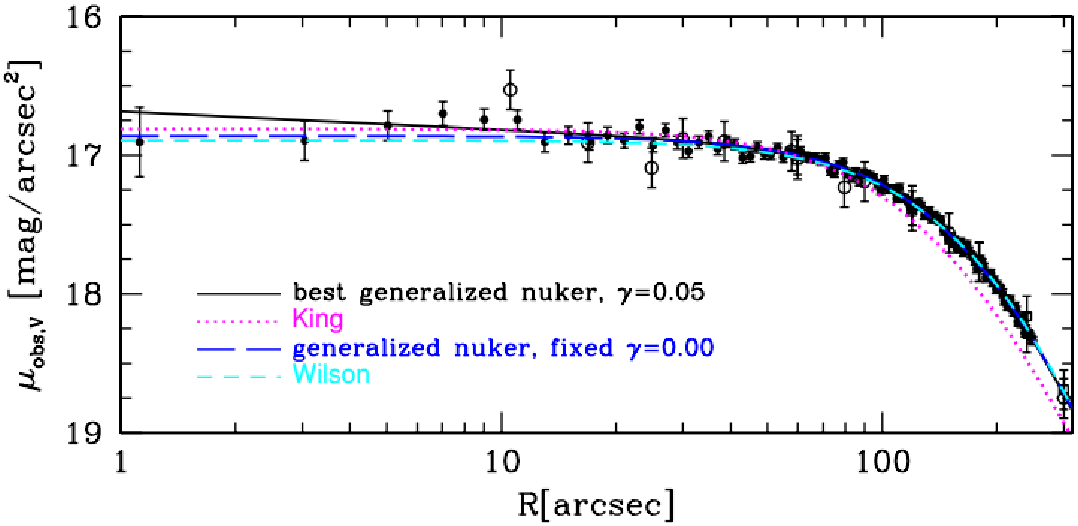

Figure 1.4: Radial profile of the projected surface brightness of the Galactic globular cluster ω Centauri. The points are a compilation of data from various sources (see van der Marel & Anderson 2010). The dotted cyan line and dashed magenta line denote the best fit King (1966) and Wilson (1975) presented in McLaughlin & van der Marel (2005). The solid black line shows the best fit of a further dynamical profile ("generalised Nuker") containing a cusp of slope $\gamma = 0.05$. This cusp is one of the primary indicators used to propose the existence of an IMBH. Taken from van der Marel & Anderson (2010).

et al. 2020; Vasiliev & Baumgardt 2021), with limitations in the central regions due to crowding effects determined by the high stellar densities. For selected objects, the kinematics of such central regions are provided by high-resolution astrometric and photometric data from the Hubble Space Telescope (see, e.g. Anderson & King 2003; Bellini et al. 2015; Libralato et al. 2018). This space-based data can then be supplemented by ground-based spectroscopic surveys which provide star velocity measurements along the line of sight (see Gaia-ESO survey by Gilmore et al. 2012 and more targeted initiatives, e.g. MIKiS survey by Ferraro et al. 2018).

When all this kinematic information is available, then the three-dimensional velocity space of a globular cluster can be fully characterised. These conditions offer the best setting to assess the possible presence of an IMBH based on inference from dynamical models.

Notable examples include ω Centauri (e.g., see Noyola et al. 2008; van der Marel & Anderson 2010; Miocchi 2010), NGC 6388 (e.g, see Lützgendorf et al. 2011; Lanzoni et al. 2013), and 47 Tucanae (Kızıltan et al. 2017) among others (for an exhaustive list, see Table 3 in Greene et al. 2020); yet, so far, uncontentious detections remain elusive. Current dynamical estimates of the mass of black holes at the centres of dense stellar systems are commonly obtained by velocity moment-based approaches using the Jeans equations (e.g., see van der Marel & Anderson 2010; Göttgens et al. 2021; Vitral et al. 2023 among others). Here, the inclusion of an IMBH component is relatively straightforward, but any degree of kinematic complexity is usually parameterised crudely. Even in this

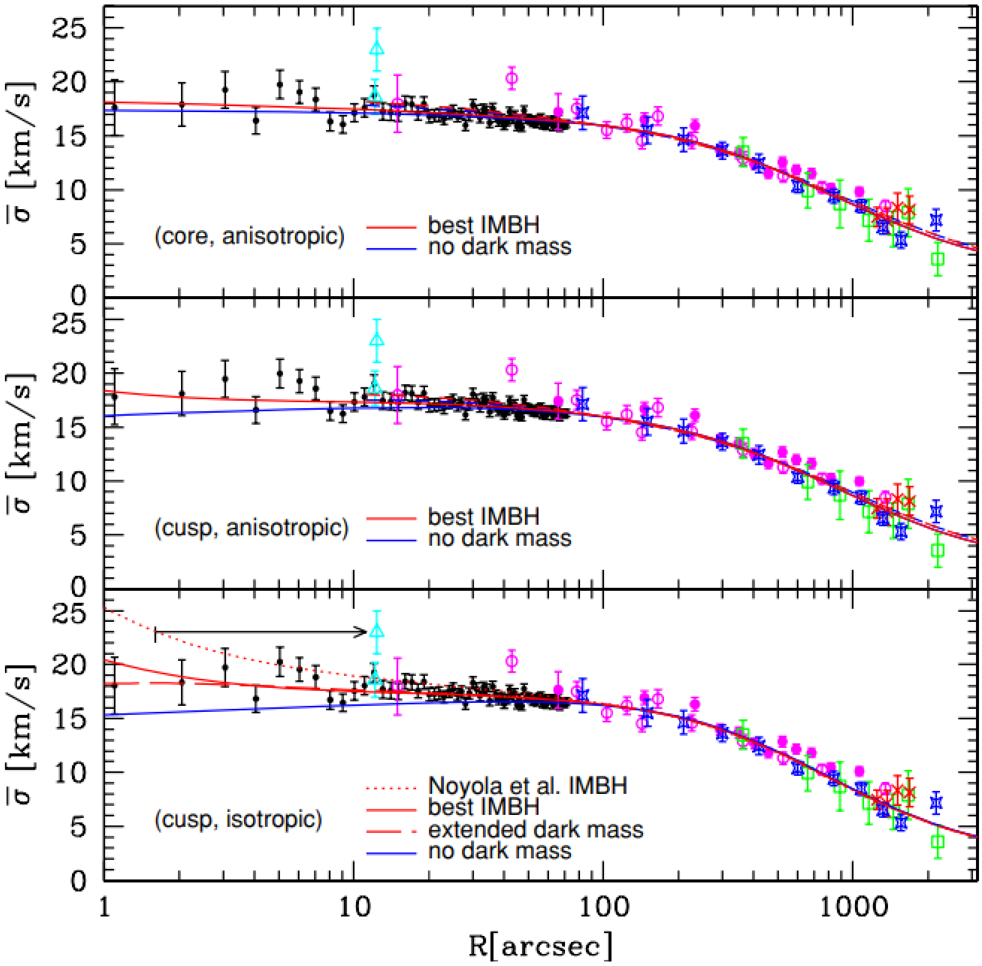

Figure 1.5: Radial profiles of the projected velocity dispersion of the Galactic globular cluster ω Centauri, compared to the profiles resulting from three dynamical models considered in van der Marel & Anderson (2010). The observational data is indicated by the points, and the model predictions by the curves. Solid curves indicate the line of sight component, and short dash lines the component on the plane of the sky. **Top**: Anisotropic models with no central cusp. The best fit IMBH has mass $M_{BH} = 4.1 \times 10^3 M_\odot$ **Middle**: As the top panel, but for a profile with a central cusp. The best fit IMBH has mass $M_{BH} = 8.7 \times 10^3 M_\odot$. **Bottom**: The arrow denotes where one of the data points considered in Noyola et al. (2008) is moved if a different cluster centre, advocated in van der Marel & Anderson (2010), is adopted. Each line indicates a different type of dark mass used within the model. The best fitting IMBH has a mass $M_{BH} = 1.8 \times 10^4 M_\odot$, compared to the $M_{BH} = 4.0 \times 10^4 M_\odot$ IMBH proposed by Noyola et al. (2008). The best fit extended dark mass has $M_{\rm dark} = 2.0 \times 10^4 M_\odot$. Both dynamical mass estimates are significantly higher than those predicted by the anisotropic models in the top two panels. Taken from van der Marel & Anderson (2010).

case, the reconstruction of the underlying distribution function (and, hence, any assessment of its well-posedness) is unfeasible.

One additional practical factor making the dynamical detection of an IMBH controversial is the challenge of accurately identifying where the centre of a star cluster is located. This task is made challenging both by the possibility of multiple definitions for the cluster centre (e.g. kinematic centre, photometric centre etc.), and also by uncertainty in the determination of the centre when a given definition is adopted (see Göttgens et al. (2021) for example). This effect can be seen in Fig. 1.5, where a relatively minor change in the cluster centre may lead to a significantly different inferred IMBH mass (for a more extreme example, see Göttgens et al. (2021) where a change in the cluster centre may completely eliminate the need for an IMBH to fit the data).

Finally, matters are further complicated by the fact that a central IMBH is not a unique source of central kinematic gradients, and many alternative explanations for these observations have been identified in globular clusters, as we will discuss in the next sections.

1.3 Kinematic complexity in globular clusters

Traditionally globular clusters have been treated as spherical, non-rotating, and isotropic stellar systems. However, this set of simplifying assumptions is now thoroughly disputed by numerous observational studies. Globular clusters have emerged as systems containing rich kinematics. This has large implications regarding the interpretation of central gradients in the density, surface brightness, or velocity dispersion profiles, and subsequent statements on the existence of an IMBH. Here, we focus primarily on three sources of kinematic complexity: velocity anisotropy, internal rotation, and the presence of centrally concentrated stellar remnants.

1.3.1 Anisotropy in velocity space

First, the assumption of isotropy is inaccurate for many globular clusters (see Fig. 1.6). Velocity anisotropy may appear in a globular cluster as imprinted by its formation process (see, e.g. van Albada 1982; Vesperini et al. 2014). For isolated clusters, this generally results in an anisotropy profile characterised by an isotropic central region that becomes increasingly radial towards the outer portions of the system. The internal dynamical evolution of a globular cluster, as driven by two-body relaxation effects, may also result in the growth of radial anisotropy in the outer regions of the system, as a result of stars on radial orbits being preferentially ejected into this region from the core (Giersz & Heggie 1994). Globular clusters also undergo evolutionary processes due to their interaction with the tidal field of their host galaxy. Due to the preferential tidal stripping of stars on radial orbits, radial anisotropy develops in the intermediate regions, with the outer parts of the system being characterised by isotropy, or even tangential anisotropy depending on the strength of the tidal environment in which the cluster is found (see, e.g. Baumgardt & Makino 2003; Tiongco et al. 2015, 2016). For an illustration of some representative observational anisotropy profiles, see Fig. 1.6 and Fig. 1.7.

The presence of velocity anisotropy in a globular cluster can significantly impact the dynamical evolution of the cluster itself. For example, Breen et al. (2017) found that the presence of tangential anisotropy caused an acceleration of

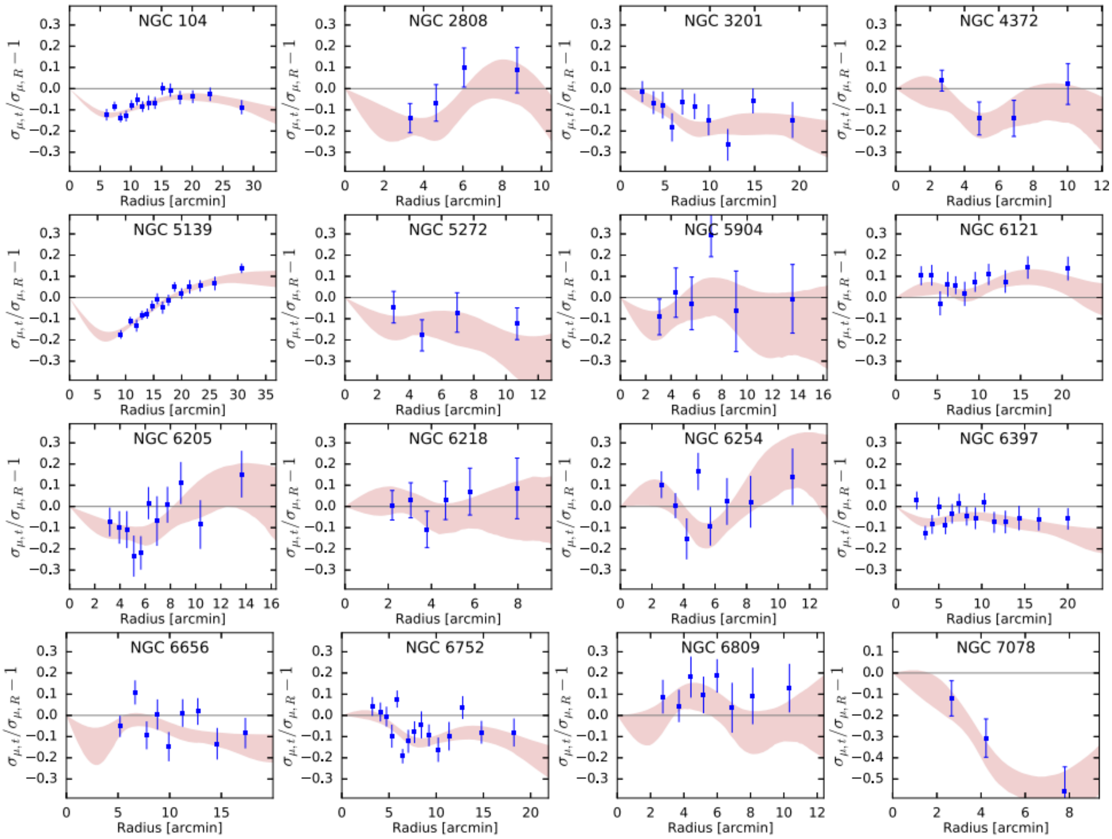

Figure 1.6: Anisotropy profiles for selected Galactic globular clusters, computed from Gaia Data Release 2 astrometry; $\sigma_{\mu,R}$ and $\sigma_{\mu,t}$ indicate the radial and tangential components of the proper motion velocity dispersion. Note the -1 factor in the definition of the anisotropy parameter used here compared to our stated definition in equation (1.10); this implies that negative values indicate radial anisotropy and vice verse for tangential anisotropy. Taken from Vasiliev & Baumgardt (2021)

.

the early dynamical evolution of a cluster, with tangentially anisotropic clusters reaching core collapse (see Heggie & Hut 2003) earlier than their isotropic, or radially anisotropic counterparts. Such an effect can then have implications for the formation of an IMBH via either the fast (Portegies Zwart et al. 2004) or slow (Giersz et al. 2015) scenarios discussed earlier.

To further complicate matters, dynamical models of globular clusters with anisotropy in the velocity space (e.g., the families proposed by Bertin & Stiavelli 1984; Merritt 1985; Dejonghe 1987; Dehnen 1993; Tremaine et al. 1994) can display steep central structural and kinematic gradients; more recently, Zocchi et al. 2017 have specifically inspected the impact of radial anisotropy. This mass-anisotropy degeneracy makes it difficult to distinguish, by inspecting the velocity moments only, between the presence of an IMBH or radial anisotropy in a spherically symmetric stellar system (see, e.g. Aros et al. 2020; Zocchi et al. 2017). This degeneracy is one of the main conceptual bottlenecks in the dynamical detection of an IMBH (see, e.g., Fig. 1.5 where we note that the presence of velocity

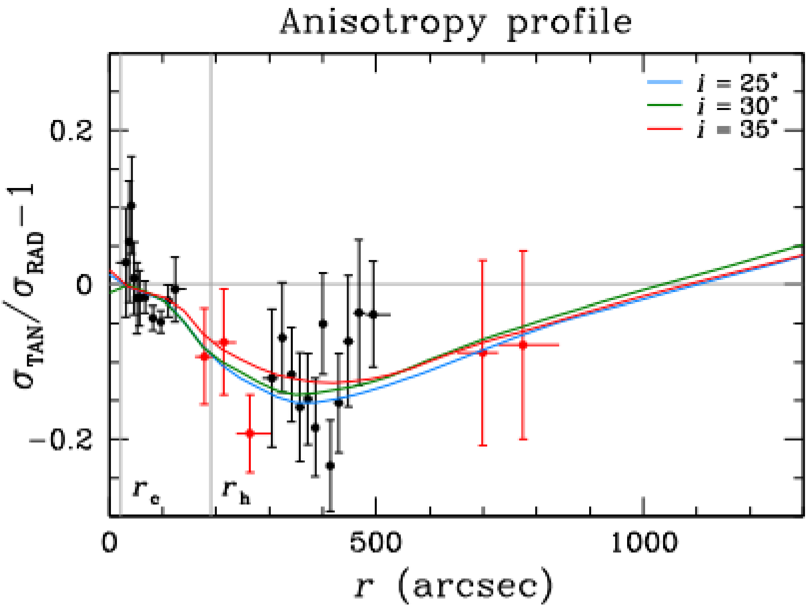

Figure 1.7: Anisotropy profiles predicted by the Varri & Bertin (2012) models (solid lines) when fitted to observational data of 47 Tuc (points). Each solid curve corresponds to a different inclination angle, *i*. The values of σ_{RAD} and σ_{TAN} indicate the radial and tangential components of the proper motion velocity dispersion. As in Fig. 1.6 note the -1 factor in the definition of the anisotropy parameter used here compared to our stated definition in equation (1.10). Note that the central region is characterised by isotropy and mild radial anisotropy in the outer regions. Taken from Bellini et al. (2017).

anisotropy decreases the dynamical mass estimate of the IMBH by an order of magnitude).

Some theoretical progress has been made in examining this degeneracy, at least in selected classes of equilibria. Recall that the magnitude and flavour of velocity anisotropy in a system is described via the anisotropy parameter (1.10), repeated here as

$$\beta(r) = 1 - \frac{\sigma_T^2(r)}{2\sigma_r^2(r)}, \tag{1.36}$$

where $\sigma_T^2(r)$ and $\sigma_r^2(r)$ are the velocity dispersions in the tangential and radial directions. An & Evans (2006) proved an inequality relating the slope of the density profile of the form $r^{-\gamma}$, and the anisotropy parameter. They showed that for constant anisotropy systems, as well as the centre of systems with radially varying velocity anisotropy, the following inequality holds true

$$\gamma \geq 2\beta_0, \tag{1.37}$$

where $\beta_0 = \lim_{r\to 0} \beta(r)$. This cusp slope-central anisotropy theorem was shown to apply to a wide class of spherical distribution function based models. Subsequent work has shown that a global density slope-anisotropy theorem, where equation (1.37) applies over the full radial extent of the system, holds for many spherical anisotropic equilibria of various forms (see, e.g. Ciotti & Morganti

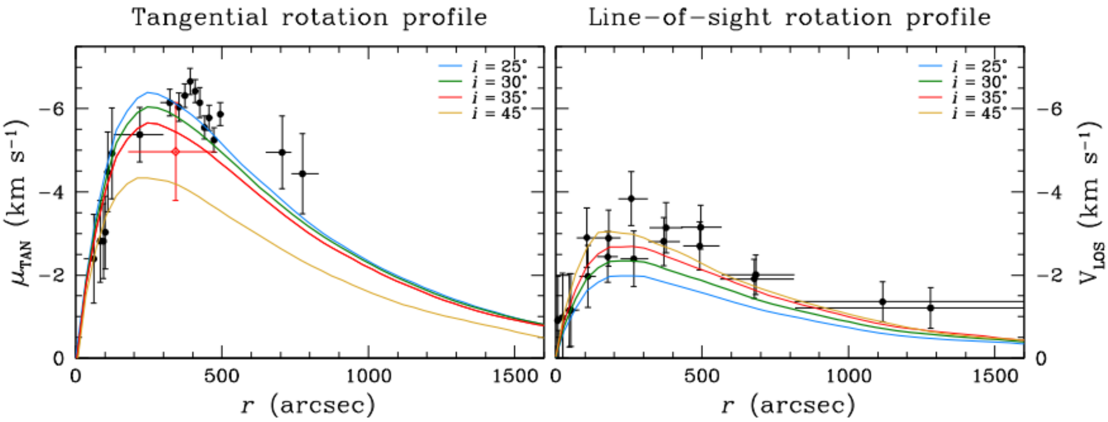

Figure 1.8: Rotation profiles in the plane of the sky (left, from Bellini et al. 2017) and along the line of sight (right, from Bianchini et al. 2013) of the Galactic globular cluster 47 Tucanae. Solid lines denote the best fit Varri & Bertin (2012) models, calculated for various inclination angles. Taken from Bellini et al. (2017).

(2009, 2010a); Ciotti & Morganti (2010b)). While this statement is not a universal property of all spherical systems,Van Hese et al. (2011) show that it holds for all spherical systems in which the augmented density is a separable function of radius and potential, with $\beta_0 \leq 1/2$; they also note that counterexamples exist for $\beta_0 > 1/2$. Nonetheless, this global density slope-anisotropy theorem applies to several dynamical equilibria used to model clusters with velocity anisotropy. This result therefore offers the opportunity to disentangle the effects of velocity anisotropy from a central mass. In particular, An & Evans (2006) presents an extension of their cusp slope-central anisotropy theorem to the case where a central mass is present.

1.3.2 Internal rotation

Theoretical investigations have shown that some degree of internal rotation may be expected in globular clusters as a result of their formation process (Mapelli 2017), or via interactions with an external tidal field during violent relaxation (Lynden-Bell 1967; Vesperini et al. 2014). Angular momentum distribution in a globular cluster can broadly be considered of two types. If the angular velocity is dependent upon the position vector, then the rotation is differential. Alternatively, if the whole system rotates at a constant angular velocity, then the rotation is akin to the one experienced by a rigid body. The latter behaviour may be expected from a rotating system allowed to reach thermodynamic equilibrium (Landau & Lifshitz 2013).

The modelling of rigidly rotating fluids has a distinguished history in theoretical astrophysics. Initially, Milne (1923) and Chandrasekhar (1933) investigated polytropic models of rigidly rotating stars using asymptotic methods (i.e., the Chandrasekhar-Milne expansion; for a description, see Tassoul 1978). A mathematically satisfactory solution to this problem was then obtained by Smith (1975), using matched asymptotic expansions. This method enabled the formal singularity occurring in the outer region of the system to be addressed (see Sect.

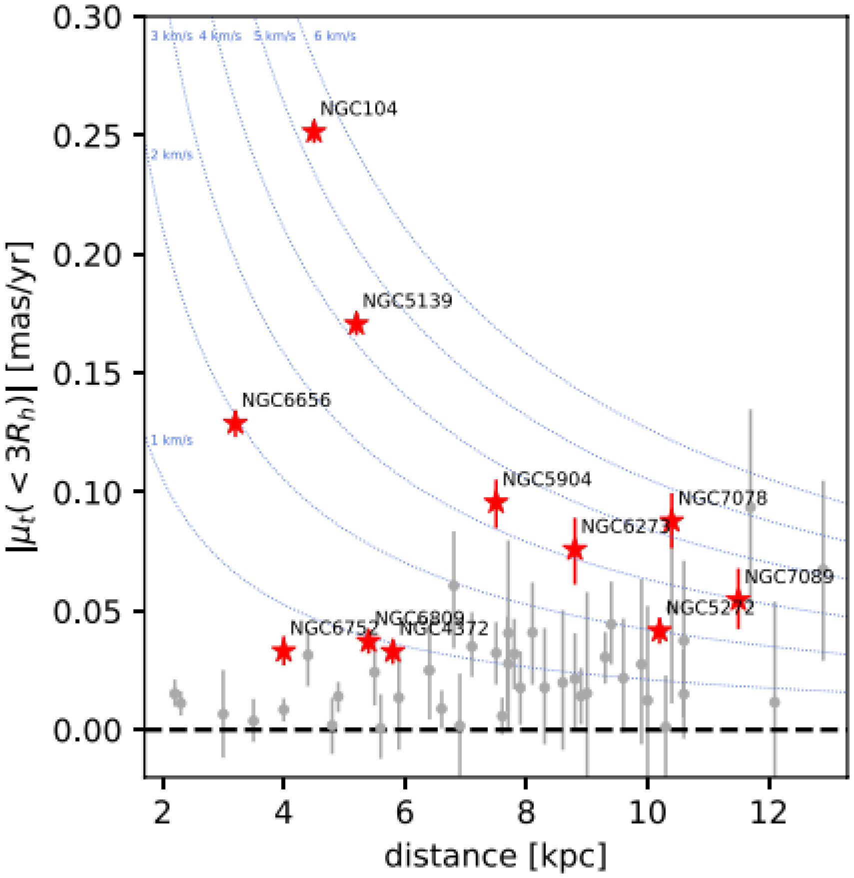

Figure 1.9: Mean tangential proper motion (from Gaia Data Release 2) in the plane of the sky against Galactocentric distance to a cluster, illustrated for selected Galactic globular clusters. Red points indicate those clusters with a statistically significant detection of internal rotation. The dotted lines indicate the level curves corresponding to mean tangential proper motions in $\mathrm{km\,s^{-1}}$. Taken from Bianchini et al. (2018).

3.4). Similar methods have then been used to construct models describing rigidly rotating globular clusters (Varri & Bertin 2012). These equilibria then form the basis of the models we construct in Chapt. 3.

Regarding the modelling of differential rotation in globular clusters, a smaller body of work is available in the literature. Distribution function based approaches often refer back to the work done by Wilson (1975) and Prendergast & Tomer (1970a), originally intended to describe elliptical galaxies (see, e.g. Sollima et al. 2009). More recently Varri & Bertin (2012) constructed models describing differentially rotating globular clusters (see, e.g. Bianchini et al. (2013); Bellini et al. (2017)). Each of these types of model includes the effect of internal rotation as an extension of the truncated isothermal spheres introduced in Sect. 1.1.5, either by modifying the form of the distribution function, as in Wilson (1975); Prendergast & Tomer (1970a), or as in Varri & Bertin (2012) by modifying the integral of motion used within the distribution function.

Several alternative modelling approaches have also been used to investigate internal rotation. As discussed in Sect. 1.2.1, it is possible to add the effect of rotation within a Jeans modelling framework (see, e.g. Sollima et al. 2019; Kamann et al. 2020). For example, by parametrising the rotation curve of a cluster as that derived by Lynden-Bell (1967), for a configuration that has undergone violent relaxation (see, e.g. Bianchini et al. 2018; Kamann et al. 2020). There are also approaches based on the orbit superposition method introduced by Schwarzschild (1979) (see, e.g. van den Bosch et al. 2006; van de Ven et al. 2006). Finally, there is also the approach used recently by Mancino et al. (2023) relying on the homeoidal expansion of ellipsoidal density distributions to provide density-potential pairs that solve the Poisson equation and which may be used in the solutions of the corresponding Jeans equations.

Observationally, many Galactic globular clusters have been found to exhibit signatures of internal rotation (see, e.g. Kamann et al. 2017; Vasiliev & Baumgardt 2021 in addition to the references already mentioned in the previous Sections). For a visual summary of the rotation signatures observed in several Galactic globular clusters, we report Fig. 1.9 from Bianchini et al. (2018). These clusters also tend to exhibit some flattening and breaking of spherical symmetry, as expected from the presence of non-vanishing global angular momentum. We especially note that typical rotation profiles for Galactic globular clusters exhibit a differential nature (see Fig. 1.8 for an example of such a rotation profile).

The breaking of spherical symmetry can itself provide a non-trivial behaviour for the velocity dispersion near the centre of a cluster (see, e.g. Prendergast & Tomer 1970a; Wilson 1975; Varri & Bertin 2012). This effect is of particular interest when investigating the presence of an IMBH inside a rotating cluster, in which both influences will certainly be present. It is not clear how the interplay between rotation and the presence of a central IMBH will manifest when considered in a self-consistent manner. We will address this point in further detail in Chapt. 3.

As well as shaping the observed structure of globular clusters, internal rotation also has important consequences for the dynamical evolution of a globular cluster. In particular, the presence of rotation has been shown to accelerate the dynamical evolution of a cluster (Einsel & Spurzem 1999), with long-term dynamical evolution acting to transport and spatially re-distribute a cluster's angular momentum content (Tiongco et al. 2017). Thus, internal rotation may have played a crucial role in the earlier evolution of a globular cluster and may have a part to play in the internal collisional processes proposed as possible mechanisms for the formation of IMBHs (see, e.g. Webb et al. 2019).

1.3.3 Centrally concentrated stellar remnants

Due to two-body relaxation, globular clusters may be expected to display some degree of energy equipartition (Heggie & Hut 2003). When components with different masses are present in a stellar system, this tends to cause those with higher masses to have lower velocities. These high-mass components then preferentially migrate towards the cluster centre. This effect is often referred to as mass segregation, and it can be an important consideration for the formation of an IMBH via dynamical interactions between high-mass stars or stellar-mass black holes, which are among the highest-mass objects in a globular cluster. These would then be expected to concentrate towards the centre, due to the effect of mass segregation.

However, as a result of their formation, dynamical encounters, and merger events, black holes may experience large velocity kicks (see, e.g. Favata et al. 2004; Merritt et al. 2004; Webb et al. 2019 and references therein). The magnitude of these kicks can be sufficiently large to eject the black hole from the cluster, thus leading to the eventual depletion of the black hole population over a relatively short timescale (the so-called Spitzer (1969) instability). However, more recent N-body simulations have shown that a system of stellar mass black holes may persist for an extended period of time (see, e.g. Breen & Heggie 2013). We may then expect many globular clusters to host such a system of stellar-mass black holes (e.g., see Dickson et al. (2024), where models with mass fractions of 1-5% in stellar-mass black holes well describe several Galatic globular clusters). These systems of stellar-mass black holes then present the possibility that the kinematic gradients sometimes attributed to an IMBH may be the result of a centrally concentrated system of dark stellar remnants (see, e.g. Peuten et al. 2016; Gieles et al. 2018; Zocchi et al. 2019; Hénault-Brunet et al. 2020).

It is then difficult to distinguish between an IMBH or a system of stellar-mass black holes. One proposed method to do so uses the fact that both scenarios impact the dynamical evolution of a globular cluster, slowing the effect of mass segregation (see, e.g. Mackey et al. 2008). Aros & Vesperini (2023) investigate this effect and find that clusters containing systems of stellar-mass black holes have different radial profiles in the degree of energy equipartition when compared to those with high mass IMBHs. The effect for IMBHs with masses $\sim 2\%$ of the cluster mass is similar to the one of a system of stellar-mass black holes.

Chapter 2

Loaded King Models

2.1 Introduction

In this chapter, we first address the key issue of the role of self-consistency in the evaluation of the potential of a dynamical model describing an idealised, spherically symmetric, isotropic stellar system harbouring a central massive object (which may be interpreted as a single point mass or as a sub-system of smaller particles of various nature). This black hole is located at the barycentre of the stellar system, at the origin of our coordinate system. Two main regimes can be identified. First, when the mass of the central object is considerably smaller than the overall mass of the host system, it is often modelled as a component of a multi-mass self-consistent equilibrium. In this context, several distribution function-based studies have been conducted, usually as applications of the approach established by Michie 1963 (e.g., see most recently Gieles & Zocchi 2015). Second, when the contribution of the central object dominates the overall potential well, the potential is often treated in a Keplerian approximation, and tracer density arguments are invoked in the description of any further mass component, avoiding any requirement of self-consistency.

The intermediate regime, where self-consistency of the solution of the relevant Poisson equation is of particular importance, is often discounted. Only a few contemporary studies of individual stars and stellar systems have considered this fundamental aspect (see Miocchi 2007; Begelman et al. 2008; Ball et al. 2011), and our inspiration has been provided by some classic studies of self-consistent equilibria with a polytropic equation of state (i.e., the "loaded polytropes" by Huntley & Saslaw 1975).

Initially, we consider the generalisation of the well-known family of King (1966) models in the presence of a central massive object. This is by no means a unique choice, and the methods detailed in this chapter can be readily extended for use with alternative prescriptions for the phase space truncation.

By formulating this construction as an initial value problem, several interesting results emerge, both concerning the mathematical treatment and its physical interpretation. This chapter is organised as follows: the problem is stated in Sects. 2.2-2.3 the details of its asymptotic description are provided in Sects. 2.4-2.6, the physical characterisation is presented in Sects. 2.7-2.8, and some concluding remarks are offered in Sect. 2.10. We also present an outline of the extension to alternative choices of phase space truncation in Sect. 2.9.

2.2 Construction of the models

2.2.1 Distribution function

We consider an idealised, spherically symmetric, isotropic stellar system with a central black hole. The black hole is modelled as a point mass, M_{BH}, located at the origin of a frame of reference centred on the barycentre of the system.

Given the overall symmetry of the problem, we adopt a spherical coordinate system, where r denotes the radial variable. The family of equilibria of interest is defined by the King (1966) distribution function

$$f_K(E) = \begin{cases} Ae^{-aE_0}\left[e^{-a(E-E_0)} - 1\right], & E \leq E_0, \\ 0, & E > E_0, \end{cases} \tag{2.1}$$

where $E = v^2/2 + \Phi(r)$ denotes the single-star energy. The positive dimensional constants A, a correspond to the physical scales of the models and can be interpreted as a global phase space normalisation and an energy scale. The further constant E_0 represents the cut-off value of the single-star energy, which can be considered as an idealised representation of the truncation imposed by the tidal environment in which the stellar system is located. The total gravitational mean-field potential, $\Phi = \Phi(r)$, consists of a component due to the black hole, given by $\Phi_{\mathrm{BH}}(r) = -GM_{\mathrm{BH}}/r$, and the potential due to the host stellar system, $\Phi_{\mathrm{C}} = \Phi_{\mathrm{C}}(r)$, to be determined self-consistently.

The main variable of interest is the dimensionless escape energy, defined as

$$\psi(r) = a\left[E_0 - \Phi_{\mathrm{C}}(r) - \Phi_{\mathrm{BH}}(r)\right]. \tag{2.2}$$

The radius at which the outer boundary of the system is located, r_t, is then defined implicitly by the condition $\psi(r_t) = 0$.

The fluid moments of the chosen distribution function, i.e. the density ρ and pressure P defined by equations (1.4) and (1.9), are obtained by computing the zeroth and second-order moments in the velocity space of the distribution function indicated in equation (2.1). The first-order velocity moment vanishes by construction. The expression for the density can be cast as a function of ψ,

$$\rho(\psi) = \hat{A}e^{\psi}\gamma\left(\frac{5}{2}, \psi\right) = \hat{A}\hat{\rho}(\psi), \tag{2.3}$$

where $\hat{A} = 8\sqrt{2}\pi A\, e^{-aE_0}/(3a^{3/2})$ and γ denotes the lower incomplete gamma function (Olver et al., 2022). The symmetry of the problem guarantees isotropy in velocity space so that the pressure tensor is diagonal, i.e. $P_{ij} = P\delta_{ij}$, with δ_{ij}

the identity matrix and P a scalar function of ψ,

$$P(\psi) = \frac{\hat{A}}{a}\frac{2}{5}e^{\psi}\gamma\left(\frac{7}{2},\psi\right) = \frac{\hat{A}}{a}\hat{P}(\psi). \tag{2.4}$$

The corresponding scalar velocity dispersion is given by

$$\sigma^2(\psi) = \frac{P(\psi)}{\rho(\psi)} = \frac{1}{a}\frac{2}{5}\frac{\gamma\left(7/2,\psi\right)}{\gamma\left(5/2,\psi\right)} = \frac{1}{a}\hat{\sigma}^2(\psi). \tag{2.5}$$

2.2.2 Poisson equation and boundary conditions

To construct self-consistent equilibria, we require that the potential $\Phi_{\mathrm{C}} = \Phi_{\mathrm{C}}(r)$ satisfies the Poisson equation

$$\nabla_r^2\Phi_{\mathrm{C}}(r) = \frac{\mathrm{d}^2\Phi_{\mathrm{C}}}{\mathrm{d}r^2} + \frac{2}{r}\frac{\mathrm{d}\Phi_{\mathrm{C}}}{\mathrm{d}r} = 4\pi G\rho(r). \tag{2.6}$$

To define a well-posed second-order initial value problem, we must also specify two boundary conditions for equation (2.6), imposed at a minimum radius r_{min}. The condition on the potential itself can be formulated by using the analogue to that used for the King (1966) models

$$\Phi_{\mathrm{C}}(r_{\mathrm{min}}) = \frac{\Psi}{a} - \frac{GM_{\mathrm{BH}}}{r_{\mathrm{min}}} - E_0, \tag{2.7}$$

where Ψ denotes the dimensionless escape energy evaluated at r_{min}.

The second condition requires further consideration: following Huntley & Saslaw (1975), we require hydrostatic equilibrium between the massive central object of mass M_{BH} and its stellar host of density $\rho = \rho(r)$, which can be expressed as

$$\frac{1}{\rho}\frac{\mathrm{d}P}{\mathrm{d}r} = -\frac{GM_{BH}}{r^2} - \frac{4\pi G}{r^2}\int_{r_{\mathrm{min}}}^{r} s^2\rho(s)\mathrm{d}s. \tag{2.8}$$

Note that we have made the assumption that interior to $r = r_{\mathrm{min}}$ the black hole dominates the potential of the system. This must necessarily be true for a sufficiently small r_{min} for any finite mass system. Mathematically, this is equivalent to considering all of the mass interior to r_{min} to be concentrated at the origin, in an analogous manner to Huntley & Saslaw (1975). This statement can be formulated as an explicit condition on the first derivative of the potential.

The problem is expressed in fully dimensionless form, with hats representing a dimensionless quantity, using the escape energy introduced at equation (2.2) and by defining the dimensionless radial variable $\hat{r} = r/r_K$, where r_K is a scale radius given by

$$r_K = \left(\frac{9}{4\pi G\rho_0 a}\right)^{1/2}, \tag{2.9}$$

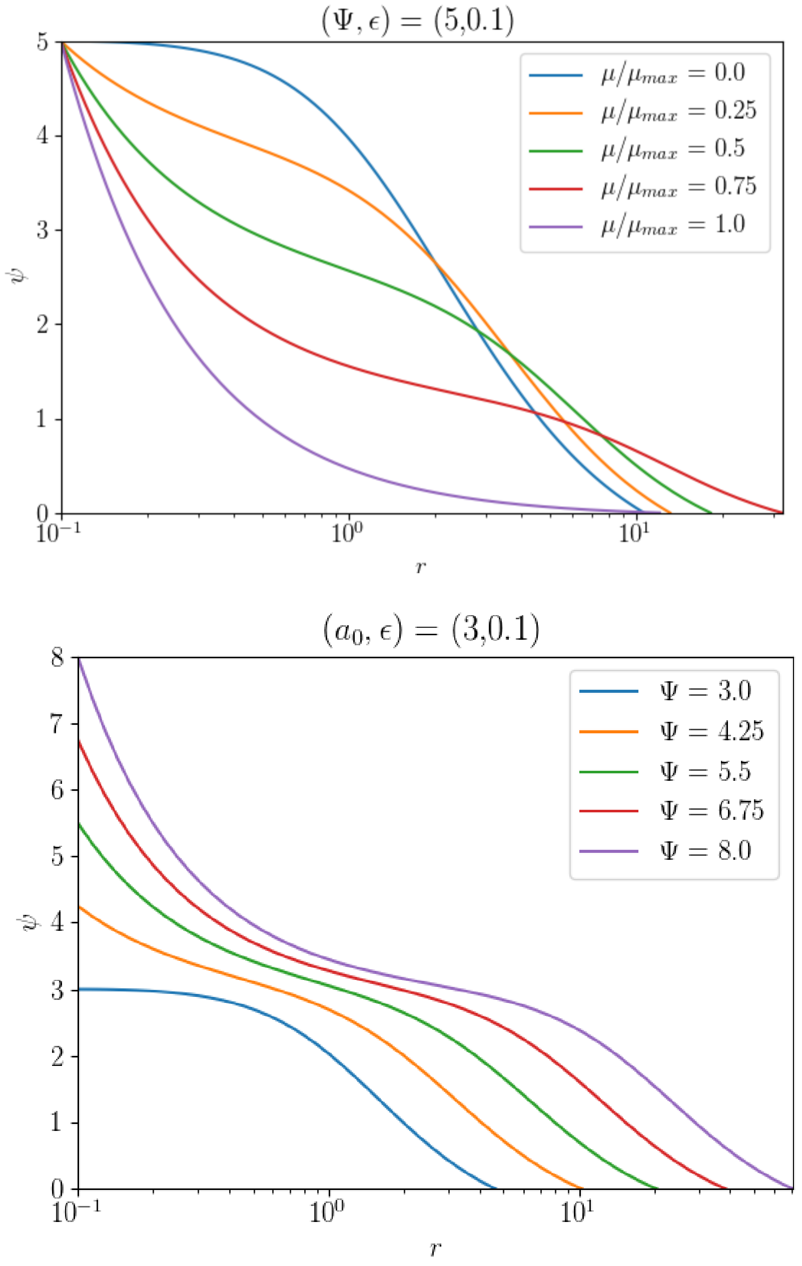

Figure 2.1: Dimensionless escape energy profiles as functions of the dimensionless radius, obtained via numerical solution of the Poisson equation (2.16). **Top:** The central dimensionless escape energy Ψ, and minimum radius ϵ have been kept constant while varying the dimensionless black hole mass μ. **Bottom:** The quantity $a_0 = \Psi - 9\mu/(4\pi\epsilon)$ and ϵ have been kept constant while varying Ψ; this is a way of indirectly increasing the dimensionless black hole mass μ. For details about a_0, see Sect. 2.2.2; for a discussion of the two parametrisations, see Sect. 2.7.1.

with ρ_0 denoting the density evaluated at $r_{\min}$. The Poisson equation (2.6) then reads

$$\nabla^2_{\hat{r}}\psi(\hat{r}) = -9\frac{\hat{\rho}(\psi)}{\hat{\rho}_0}. \tag{2.10}$$

Substituting equations (2.3) and (2.4) into the left hand side of equation (2.8), it is obtained that

$$\frac{1}{\rho}\frac{\mathrm{d}P}{\mathrm{d}\hat{r}} = \frac{\hat{A}}{a}\frac{1}{\rho}\left(\mathrm{e}^{\psi}\gamma\left(\frac{7}{2},\psi\right) + \psi^{5/2}\right)\frac{\mathrm{d}\psi}{\mathrm{d}\hat{r}} = \frac{1}{a}\frac{\mathrm{d}\psi}{\mathrm{d}\hat{r}}, \tag{2.11}$$

where, in the second equality, we have used the recurrence relation for the lower incomplete gamma function (Olver et al., 2022)

$$\gamma\left(n+1,\psi\right) = n\gamma(n,\psi) - \psi^n \mathrm{e}^{-\psi}. \tag{2.12}$$

The hydrostatic condition posed in equation (2.8) can therefore be rescaled via equation (2.9), and expressed as

$$\frac{\mathrm{d}\psi}{\mathrm{d}\hat{r}} = -\frac{9\mu}{4\pi\hat{r}^2} - \frac{9}{4\pi\hat{r}^2}\int_{\epsilon}^{\hat{r}} 4\pi s^2 \frac{\hat{\rho}}{\hat{\rho}_0}\mathrm{d}s, \tag{2.13}$$

where

$$\mu \equiv \frac{M_{BH}}{\rho_0 r_K^3} \tag{2.14}$$

and

$$\epsilon \equiv \frac{r_{\min}}{r_K} \tag{2.15}$$

emerge as the appropriate definitions of two of the key parameters of the models under consideration: the dimensionless mass of the black hole and the dimensionless minimum radius.

The boundary conditions introduced above are, therefore, set at the minimum radius $\hat{r} = \epsilon$. The first condition stated at equation (2.7), therefore, becomes $\psi(\epsilon) = \Upsilon$, so that $\hat{\rho}_0 = \hat{\rho}(\Upsilon)$. The positive constant Υ corresponds to the central dimensionless escape energy of a given equilibrium, and it defines the third and last parameter of this family of models.

We then set the condition on the derivative via equation (2.13).

The initial value problem in dimensionless form is, therefore, fully specified as

$$\begin{aligned}
\nabla^2_{\hat{r}}\psi &= -9\frac{\hat{\rho}(\psi)}{\hat{\rho}(\Upsilon)} \equiv -K(\psi,\Upsilon),\\
\psi(\epsilon) &= \Upsilon,\\
\psi'(\epsilon) &= -\frac{9\mu}{4\pi\epsilon^2}.
\end{aligned} \tag{2.16}$$

To recapitulate, the equilibria examined here are characterised by two physical scales (i.e., A, a) and three parameters: the dimensionless mass of the central black hole μ, the central dimensionless escape energy Ψ, and the dimensionless minimum radius ϵ.

An immediate consequence of the second boundary condition is the existence of a constraint on the central dimensionless escape energy, such that $\Psi - 9\mu/(4\pi\epsilon) > 0$. This expression is required to be positive because, physically, it represents the difference between the depth (with respect to the cut-off energy E_0) of the total dimensionless escape energy at the minimum radius and the contribution attributed to the presence of the central black hole at that location, i.e., the dimensionless escape energy of the host stellar system at the minimum radius is required to be well-posed (see equations (2.2) and (2.7)). Mathematically, this combination of parameters will also assume a key role in the asymptotic description of the equilibria (see Sect. 2.4). Consequently, there is a maximum value of the dimensionless black hole mass that we consider, defined by

$$\mu_{\max} = \frac{4\pi\Psi\epsilon}{9}, \tag{2.17}$$

such that $a_0(\Psi, \epsilon, \mu_{\max}) = \Psi - 9\mu_{\max}/4\pi\epsilon = 0$.

When $\mu = \epsilon = 0$, the initial value problem formulated at equation (2.16) reduces to the problem which defines the King (1966) models, without any central object.

When $\mu = 0$, it is then possible to set $\epsilon \neq 0$ but For simplicity of notation, for the remainder of this chapter, the 'hat' symbol will be omitted from all dimensionless quantities, unless otherwise specified.

2.3 Parameter space

2.3.1 Numerical exploration

We solve the second-order nonlinear ordinary differential equation (2.16) with standard numerical methods; we have adopted a 4th order Runge-Kutta scheme (see App. B.1 for a description of an implementation in Python). In Fig. 2.1, we show the resulting radial profiles of the dimensionless escape energy $\psi = \psi(r)$. The main feature which emerges from this numerical exploration is the steepening of the central slope of the solutions as the value of the parameter μ increases, directly or indirectly.

A second characteristic concerns the radial extension of solutions. As illustrated in Fig. 2.2, equilibria characterised by increasing values of dimensionless black hole mass, μ, with fixed values of central dimensionless escape energy, Ψ, and minimum radius ϵ, show a sharp transition in their structure over a relatively small range of μ, at a value $\mu = \mu_c$ near, but not equal to, $\mu = \mu_{\max}$.

This transition manifests itself in the values of the dimensionless truncation radius, r_t, and of the dimensionless mass of the cluster, M_C, which can be computed straightforwardly as

$$M_C = 4\pi \int_{\epsilon}^{r_t} r^2 \frac{\rho(\psi(r))}{\rho(\Psi)} \mathrm{d}r. \tag{2.18}$$

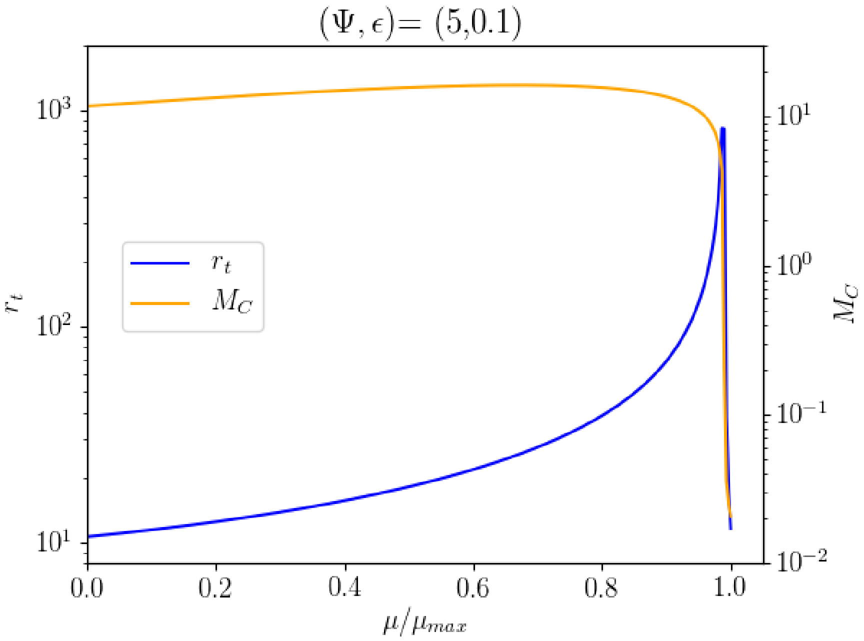

Figure 2.2: Dimensionless truncation radius, r_t, and stellar mass, M_C, for models with increasing values of the dimensionless black hole mass μ, and fixed values of central dimensionless escape energy Ψ and minimum radius ϵ. There is a sharp transition between equilibria dominated by the mass of the host stellar system or by the mass of the central black hole, which is located to the left and right of the maximum of $r_t(\mu)$.

Noting equation (2.13) allows us to extract M_C directly from the solution to the Poisson equation (2.16), avoiding further integration, via

$$M_C = -\mu - \frac{4\pi}{9} r_t^2 \left.\frac{\mathrm{d}\psi}{\mathrm{d}r}\right|_{r=r_t} . \tag{2.19}$$

This behaviour defines a transition between two distinct cases, corresponding to equilibria which are dominated by the mass of the host stellar system or by the mass of the central black hole. A similar sharp transition has been noted in other families of self-consistent dynamical models with central black holes (Huntley & Saslaw, 1975; Miocchi, 2007), but, so far, has never been studied in detail. This transition is the focus of this chapter.

After this numerical exploration, we now formally introduce the parameter space of the equilibria, and we identify three distinct regimes, defined based on a specific scaling of the main parameters, which require different mathematical treatments.

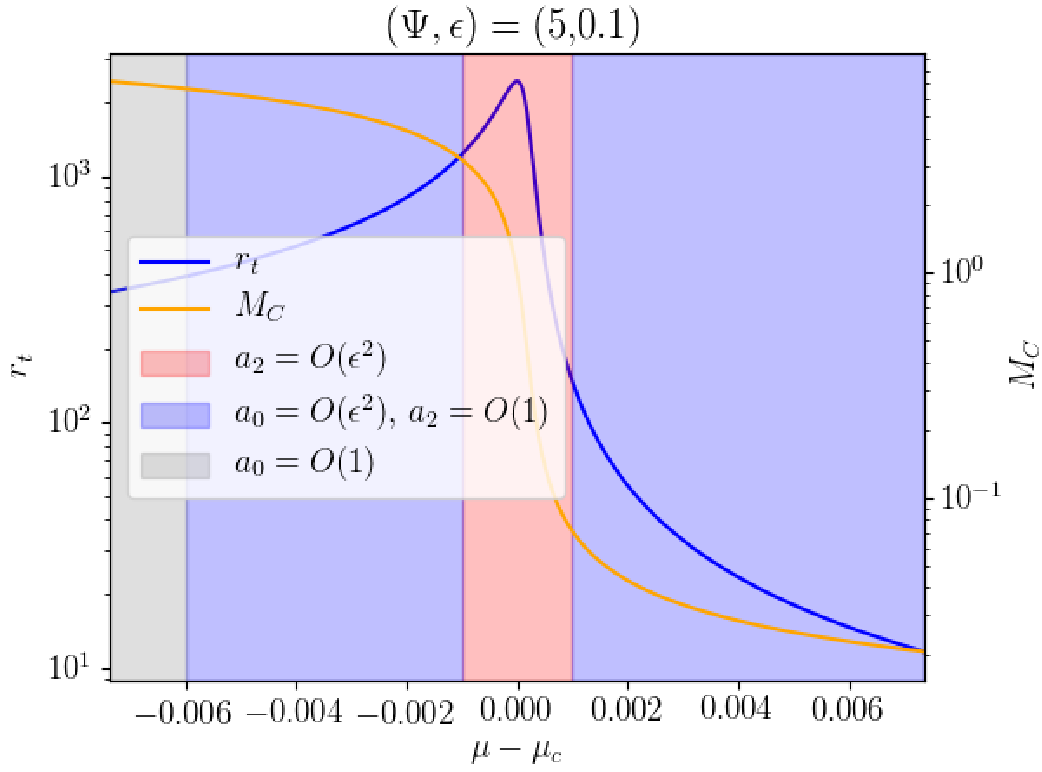

Figure 2.3: A magnified view of the models depicted in Fig. 2.2, with a schematic illustration of the three nested asymptotic regimes (see Sect. 2.3.2). The critical μ_c corresponds to the value at which $r_t(\mu)$ reaches the maximum. The asymptotic solution in Regime 3 (see Sect. 2.6) provides an expression for μ_c as an explicit function of Ψ and ϵ.

2.3.2 Three nested asymptotic regimes

We consider the dimensionless minimum radius, ϵ, as the small parameter of reference. Physically, this is appropriate given the approximation that the mass interior to that boundary is treated as being part of the central object. It is then desirable for the excluded region to be sufficiently small that this approximation is valid.

The asymptotic regimes of interest are defined via three scaling conditions with respect to ϵ, as schematically illustrated in Fig. 2.3. The quantities a_0 and a_2 appearing there are the constants of integration arising from the solution of the $O(1)$ and $O(\epsilon^2)$ equations, which are obtained when considering equation (2.16) in a region close to the centre of the system. These constants will be directly related to the initial parameters in the following sections. For fixed ϵ and Ψ, these three regimes correspond to values of μ that are ever closer to the critical value of μ at which the previously noted transitional behaviour is observed. Within each regime, the solution is non-uniform in r, and as such we require multiple regions with different radial scalings (again in terms of ϵ) to accurately describe the solution.

2.4 Regime 1: $\mathbf{a_0 = O(1)}$

Regime 1 is defined by

$$a_0 = \Psi - \frac{9\mu}{4\pi\epsilon} = O(1), \tag{2.20}$$

and corresponds to equilibria in which the contribution of the central black hole to the total dimensionless escape energy is subdominant compared to that due to the star cluster. The reason for keeping control of this particular combination of parameters will be made clear below.

Proper treatment of the solution to equation (2.16) in this regime requires two asymptotic regions. One to describe the behaviour of the solution towards the centre, defined by taking $r = O(\epsilon)$; this is Region I. The second region, Region II, describes the behaviour far from the central part of the domain with $r = O(1)$.

2.4.1 Region I

To examine the behaviour of the dimensionless escape energy in the vicinity of the central black hole we let $r_1 = \epsilon^{-1} r$. Under this rescaling, equation (2.16) becomes

$$\begin{aligned} \nabla^2_{r_1} \psi^{(\mathrm{I})} &= -\epsilon^2 K(\psi, \Psi), \\ \psi^{(\mathrm{I})}(1) &= \Psi, \\ \psi^{(\mathrm{I})\prime}(1) &= -\frac{9\mu}{4\pi\epsilon}. \end{aligned} \tag{2.21}$$

Keeping $\mu/\epsilon = O(1)$ constant allows us to achieve a well-posed definition of the boundary condition on the gradient, in its limit for $\epsilon \to 0$. This then makes clear the choice of scaling chosen in equation (2.20).

We now look for a solution to equation (2.21) as an expansion in ϵ with

$$\psi^{(\mathrm{I})}(r_1) = \psi_0^{(\mathrm{I})}(r_1) + \epsilon\psi_1^{(\mathrm{I})}(r_1) + \epsilon^2\psi_2^{(\mathrm{I})}(r_1) + \cdots . \tag{2.22}$$

Substituting equation (2.22) into equation (2.21) provides a series of initial value problems at each order in ϵ; at leading-order we have

$$\begin{aligned} &\nabla^2_{r_1}\psi_0^{(\mathrm{I})}(r_1) = 0, \\ &\psi_0^{(\mathrm{I})}(1) = \Psi, \\ &\psi_0^{(\mathrm{I})\prime}(1) = -\frac{9\mu}{4\pi\epsilon}. \end{aligned} \tag{2.23}$$

This problem is integrated to give

$$\psi^{(\mathrm{I})}(r_1) = \left(\Psi - \frac{9\mu}{4\pi\epsilon}\right) + \frac{9\mu}{4\pi\epsilon}\frac{1}{r_1} = a_0 + \frac{9\mu}{4\pi\epsilon}\frac{1}{r_1}. \tag{2.24}$$

Intuitively, this expression corresponds to the case of a point mass located at the origin, i.e., at leading-order, we neglect any contribution from the surrounding stars. The definition of the constant a_0, which was anticipated in Sect. 2.3.2, emerges naturally from this leading-order solution. The positivity requirement $a_0 > 0$ has been posed and discussed at the end of Sect. 2.2.2.

By evaluating, via direct substitution in equation (2.21), the subsequent terms of the expansion at equation (2.22), at $O(\epsilon)$ we obtain that $\psi_1^{(\mathrm{I})}(r_1) = 0$, which implies that also higher-order odd terms in the series expansion will vanish; at $O(\epsilon^2)$, however, the associated problem reads

$$\begin{aligned} &\nabla^2_{r_1}\psi_2^{(\mathrm{I})}(r_1) = -K\left(\psi_0^{(\mathrm{I})}, \Psi\right), \\ &\psi_2^{(\mathrm{I})}(1) = 0, \\ &\psi_2^{(\mathrm{I})\prime}(1) = 0. \end{aligned} \tag{2.25}$$

This problem states that the first non-vanishing correction to the leading-order behaviour is given by the response of the system due to the potential generated by the central object, and, in practice, in the inner region, the stars behave as a tracer density distribution. The term $\psi_2^{(\mathrm{I})}$ can be shown to grow quadratically as $r_1 \to \infty$; as a result, the expansion (2.22) becomes disordered for $r_1 = O(\epsilon^{-1})$.

This means that the leading and second-order terms eventually become of comparable size and the expansion breaks down. To push our solution further out from the inner region, we return to the original radial variable and consider a more extended portion of the domain, denoted as region II.

2.4.2 Region II

In this region, the main statement of the problem is unchanged from equation (2.16), however, we must obtain an appropriate pair of boundary conditions. This is achieved by applying Van Dyke's asymptotic matching principle (Van Dyke, 1975), to match the leading-order solution in Region II, $\psi_0^{(\mathrm{II})}(r)$, to the leading-order solution in Region I. The $O(1)$ region II problem, therefore, is given by

$$\begin{aligned}
\nabla_r^2 \psi_0^{(\mathrm{II})} &= -K\left(\psi_0^{(\mathrm{II})}, \Psi\right), \\
\psi_0^{(\mathrm{II})}(0) &= \lim_{r_1 \to \infty} \psi_0^{(\mathrm{I})} = a_0, \\
\psi_0^{(\mathrm{II})\prime}(0) &= \lim_{r_1 \to \infty} \psi_0^{(\mathrm{I})\prime} = 0,
\end{aligned} \tag{2.26}$$

which corresponds to the problem for a classic King (1966) model, with a modification of the first boundary condition, which is set as a_0, rather than the usual Ψ.

In Fig. 2.4, we present the comparison between the numerical solution of an equilibrium in Regime 1 and the approximate solutions derived in the two asymptotic regions described above. This depiction shows that the slope in the innermost region is well captured by the inner solution (region I), while the behaviour in the remainder of the domain (region II) is well approximated by the solution to equation (2.26), which can be dealt with numerically via standard methods. An overall solution in Regime 1, therefore, physically corresponds to the composition of a small region at the centre of the system, where the black hole is dominant, surrounded by a much larger region, where the effect of the black hole is limited to a modification of the central value of dimensionless escape energy.

We also assess whether this asymptotic description already captures the sharp transition identified via the numerical parameter space exploration (see Sect. 2.3.1). In Fig. 2.5, we examine the values of the truncation radius resulting from the numerical solution of the region II problem stated at equation (2.26). This asymptotic description predicts the observed increase in the size of the equilibria. We quantify this increase by rescaling equation (2.26) for sufficiently small a_0, where we also approximate the behaviour of $\gamma(a, \psi)$ for small values of the argument ψ (e.g., see Bender & Orszag 1999, equation [6.2.5]). Posing $\tilde{r} = r a_0^{3/4}$ and $\phi = \psi^{(\mathrm{II})}/a_0$, we obtain

$$\begin{aligned}
\nabla_{\tilde{r}}^2 \phi &= -\frac{18}{5\rho(\Psi)} \phi^{5/2} \equiv -\kappa(\Psi)\phi^{5/2}, \\
\phi(1) &= 1, \\
\phi\prime(1) &= 0,
\end{aligned} \tag{2.27}$$

and from the two scaling conditions introduced above, we conclude that $r_t \propto a_0^{-3/4}$. This predicts that the vertical asymptote in Fig. 2.5 is located at a value of μ such that $a_0 = 0$. However, this estimate of the critical value does not fully agree with the location of the transition observed in Fig. 2.5, nor do we obtain any

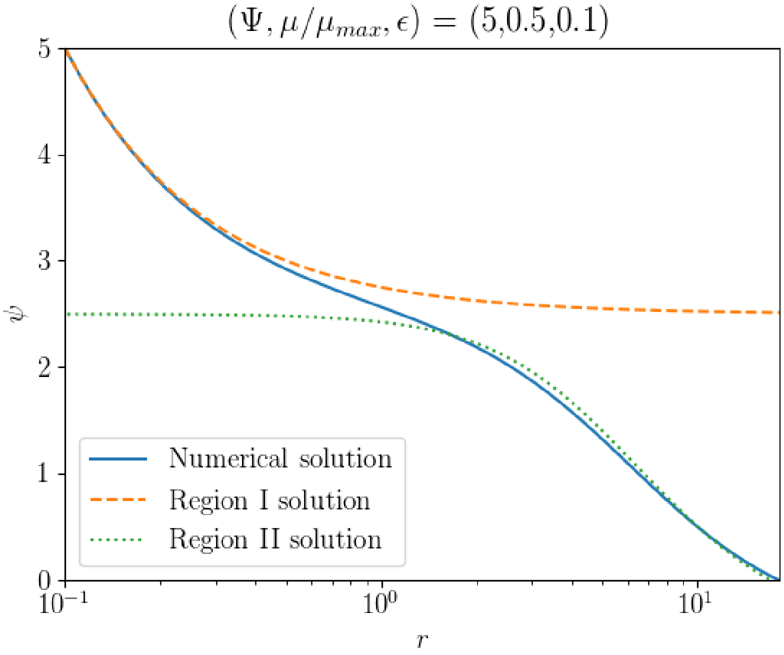

Figure 2.4: Numerical solution (solid) of the full Poisson equation (2.16) for a model in Regime 1, compared with the asymptotic solutions for the region I problem (dashed) stated at equation (2.24) and the region II problem (dotted) stated at equation (2.26).

insight on the equilibria beyond the critical value itself, for which the prediction via this asymptotic description is much too large. To access the next portion of the parameter space, in closer proximity to the sharp transition, we must allow $a_0 = 0$. This condition breaks the defining assumption of the current Regime 1 (i.e., $a_0 = O(1)$), hence a new regime is needed.

2.5 Regime 2: $a_0 = O(\epsilon^2)$, $a_2 = O(1)$

Examining equation (2.16) at the subsequent order $a_0 = O(\epsilon)$, the same set of effective problems just discussed in Sect. 2.3 is recovered, hence, for conciseness, we omit them. The next order of interest is, therefore, given by $a_0 = O(\epsilon^2)$ which admits smaller values of a_0 than Regime 1. Thus, Regime 2 is defined by $a_0 = O(\epsilon^2)$, with $a_2 = O(1)$. This regime will require three asymptotic regions for a full treatment: a region describing the inner and outer behaviour as before, along with an intermediate region. This will allow us to assess that $a_2 = 0$ is a key condition for predicting the location of the transition.

We start, once again, by examining the problem in the vicinity of the central object (region I).

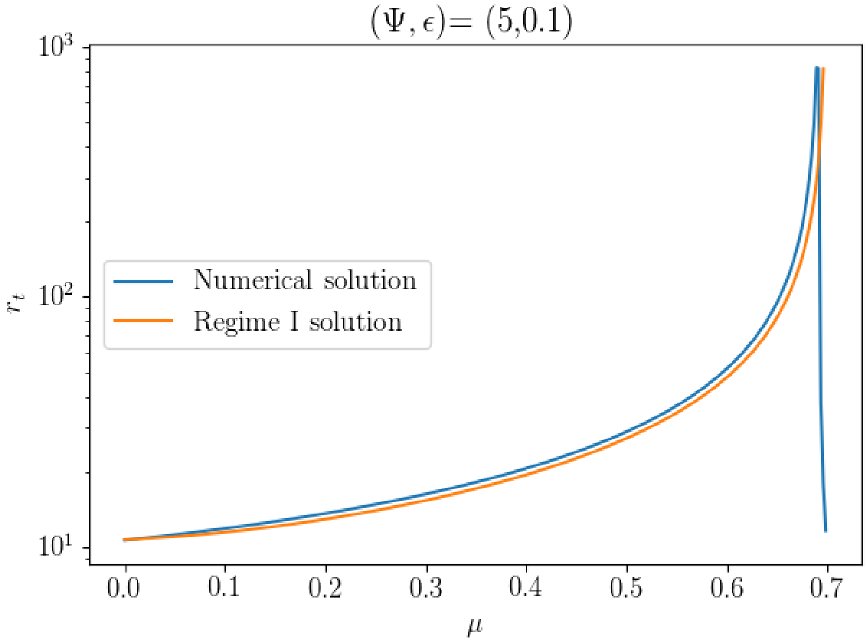

Figure 2.5: Comparison of the values of the truncation radius of the models obtained by numerically solving the full Poisson equation (2.16), and those determined in Regime 1, by solving the region II problem stated at equation (2.26).

2.5.1 Region I

Adopting the same radial scaling employed in Sect. 2.4.1, $r_1 = \epsilon^{-1} r$, equation (2.16) takes the form

$$\begin{aligned} &\nabla^2_{r_1} \psi^{(\mathrm{I})}(r_1) = -\epsilon^2 K\left(\psi^{(\mathrm{I})}, \Psi\right), \\ &\psi^{(\mathrm{I})}(1) = \Psi, \\ &\psi^{(\mathrm{I})\prime}(1) = -\Psi + A_0 \epsilon^2, \end{aligned} \tag{2.28}$$

where the only difference compared to the equivalent problem in Regime 1 (as stated at equation (2.21)) is the rewriting of the second boundary condition to make explicit the relevant scaling, $a_0 = \epsilon^2 A_0$. We then look for a solution to equation (2.28) as an expansion in ϵ

$$\psi^{(\mathrm{I})}(r_1) = \psi_0^{(\mathrm{I})}(r_1) + \epsilon^2 \psi_2^{(\mathrm{I})}(r_1) + \epsilon^4 \psi_4^{(\mathrm{I})}(r_1) + \ldots, \tag{2.29}$$

where, as in Regime 1, only even terms are of interest. At leading-order we thus have

$$\begin{aligned} &\nabla^2_{r_1} \psi_0^{(\mathrm{I})}(r_1) = 0, \\ &\psi_0^{(\mathrm{I})}(1) = \Psi, \\ &\psi_0^{(\mathrm{I})\prime}(1) = -\Psi, \end{aligned} \tag{2.30}$$

which is integrated to provide

$$\psi_0^{(\mathrm{I})}(r_1) = \frac{\Upsilon}{r_1}. \tag{2.31}$$

By using this expression, the relevant problem at $O(\epsilon^2)$ becomes

$$\begin{aligned} &\nabla_{r_1}^2 \psi_2^{(\mathrm{I})}(r_1) = -K\left(\frac{\Upsilon}{r_1}, \Upsilon\right) \\ &\psi_2^{(\mathrm{I})}(1) = 0, \\ &\psi_2^{(\mathrm{I})\prime}(1) = A_0. \end{aligned} \tag{2.32}$$

whose solution is written in integral form as

$$\psi_2^{(\mathrm{I})}(r_1) = A_0 - \frac{A_0}{r_1} - \frac{9}{\rho(\Upsilon)} \int_1^{r_1} \frac{1}{t^2} \int_1^t s^2 \rho\left(\frac{\Upsilon}{s}\right) \mathrm{d}s \, \mathrm{d}t. \tag{2.33}$$

where we have explicitly expressed K in terms of the dimensionless density ρ (see equation (2.16)). Integrating by parts reduces the double integral at the right-hand-side of equation (2.33) to a sum of two integrals. To evaluate the behaviour of the solution in the limit of large r_1, we use the power-law approximation for the incomplete gamma function

$$\gamma\left(\frac{5}{2}, \frac{\Upsilon}{r_1}\right) = \frac{2}{5}\Upsilon^{5/2} r_1^{-5/2}, \tag{2.34}$$

as Υ/r_1 is small. Thus, the integral term in equation (2.33) is given by

$$\begin{aligned} &\int_1^{r_1} \frac{1}{t^2} \int_1^t s^2 \rho\left(\frac{\Upsilon}{s}\right) \mathrm{d}s \, \mathrm{d}t = \\ &= -\frac{1}{r_1} \int_1^{r_1} s^2 \left(\rho\left(\frac{\Upsilon}{s}\right) - \frac{2}{5}\Upsilon^{5/2} s^{-5/2}\right) \mathrm{d}s \\ &- \frac{2\Upsilon^{5/2}}{5r_1} \int_1^{r_1} s^{-1/2} \mathrm{d}s + \int_1^{r_1} s\rho\left(\frac{\Upsilon}{s}\right) \mathrm{d}s. \end{aligned} \tag{2.35}$$

We then note that

$$\begin{aligned} \int_1^{r_1} s^2 \left(\rho\left(\frac{\Upsilon}{s}\right) - \frac{2}{5}\Upsilon^{5/2} s^{-5/2}\right) \mathrm{d}s = &\int_1^{\infty} s^2 \left(\rho\left(\frac{\Upsilon}{s}\right) - \frac{2}{5}\Upsilon^{5/2} s^{-5/2}\right) \mathrm{d}s - \\ &\int_{r_1}^{\infty} s^2 \left(\rho\left(\frac{\Upsilon}{s}\right) - \frac{2}{5}\Upsilon^{5/2} s^{-5/2}\right) \mathrm{d}s. \end{aligned}$$

With the subtraction of the $r^{-5/2}$ part of the density the resulting expression has leading-order terms of $O(r^{-7/2})$ and so the first of the above integrals converges to a finite value, while the second converges to zero. A similar operation with the final integral in equation (2.35) allows us to obtain the large radius behaviour of $\psi_2^{(\mathrm{I})}$ as

$$\psi_2^{(\mathrm{I})}(r_1) \sim a_2 + \frac{b_2}{r_1} + 4\kappa\Psi^{5/2} r_1^{-1/2}, \tag{2.36}$$

as $r_1 \to \infty$, where

$$a_2 = A_0 - \frac{9}{\rho(\Psi)} \int_1^\infty s\rho\left(\frac{\Psi}{s}\right) \mathrm{d}s \equiv A_0 + C(\Psi), \tag{2.37}$$

and

$$b_2 = -A_0 + \frac{9}{\rho(\Psi)} \left[\int_1^\infty s^2 \left(\rho\left(\frac{\Psi}{s}\right) - \frac{2}{5}\Psi^{5/2} s^{-5/2}\right) \mathrm{d}s\right] - \frac{4}{5}\Psi^{5/2}. \tag{2.38}$$

The second term in equation (2.37) depends only on the central dimensionless escape energy, Ψ. Another important observation is that this term is negative, and thus a_2 can become negative for sufficiently small values of A_0.

To capture the sharp transition noted in Fig. 2.2, we must also examine the $O(\epsilon^4)$ term in the expansion given by equation (2.29). At this order, the problem at equation (2.28) reads

$$\begin{aligned} &\nabla_{r_1}^2 \psi_4^{(\mathrm{I})}(r_1) = -\frac{9}{\rho(\Psi)} \left(\rho\left(\frac{\Psi}{r_1}\right) + \Psi^{3/2} r_1^{-3/2}\right) \psi_2^{(\mathrm{I})}, \\ &\psi_4^{(\mathrm{I})}(1) = 0 \\ &\psi_4^{(\mathrm{I})\prime}(1) = 0. \end{aligned} \tag{2.39}$$

In the limit of large r_1, we obtain an explicit expression for $\psi_4^{(\mathrm{I})}$ using both the power-law approximation to the incomplete gamma function (see equation (2.34)), and equation (2.36). This expression is written in compact form as

$$\psi_4^{(\mathrm{I})}(r_1) = a_4 - \frac{10}{3}\kappa a_2 \Psi^{3/2} r_1^{1/2} - 10\kappa^2\Psi^4 \ln r_1 + o(r_1^{1/2}), \tag{2.40}$$

where only the terms of interest are reported and a_4 denotes a constant which is obtained, in closed form, in a similar manner to a_2. The exact form of a_4 is not important for Regime 2, so we defer the explicit expression until we consider Regime 3, in the next section.

With the asymptotic behaviour of the solution in Region I now in hand, it becomes apparent that the expansion at equation (2.29) will not, in general, be valid over the entire domain. As in the previous Regime 1, the series will become disordered at the location where higher-order terms in the expansion become of comparable size to the leading-order term. This necessitates further rescaling and subsequent asymptotic matching between the relevant regions. In view of the large r_1 approximations stated at equations (2.36) and (2.40), three possibilities exist:

1. if $a_2 > 0$ and $a_2 = O(1)$, then the region I expansion breaks down for

$r_1 = O(\epsilon^{-2})$. This location is obtained by considering when the constant term in equation (2.36) becomes as large as the leading-order solution. In this case, a further asymptotic region is required to push the solution further out from the centre. This case is considered immediately below, in Sect. 2.5.2.

2. if $a_2 < 0$ and $a_2 = O(1)$, then $\psi^{(\mathrm{I})}(r_1)$ reaches zero before any breakdown in the asymptotic expansion occurs. In this case, the region I solution is sufficient to fully describe the system.

3. if $|a_2| = O(\epsilon^2)$, then the region I expansion breaks down for $r_1 = O(\epsilon^{-4})$, when the leading-order solution, equation (2.36), and equation (2.40) all become comparable in magnitude. This defines the third, and final, regime of interest to us, and we defer its discussion until Sect. 2.6.

2.5.2 Region II

When the region I solution breaks down, we expect, by the leading-order estimate, that $\psi = O(\epsilon^2)$. Consequently, the necessary rescaling to examine the next region from the centre is given by $r_2 = \epsilon^2 r_1$, and $\psi^{(\mathrm{II})}(r_2) = \epsilon^2 \phi(r_2)$. Under this rescaling, the Poisson equation becomes

$$\nabla^2_{r_2}\phi(r_2) = -\kappa(\Psi)\epsilon\phi^{5/2}, \tag{2.41}$$

where we have again made use of the power-law approximation of the incomplete gamma function for small argument ψ. We seek a solution to equation (2.41) as an expansion in ϵ; the resulting free coefficients will be determined via the usual matching procedure with the region I solution. At leading-order, we have

$$\nabla^2_{r_2}\phi_0(r_2) = 0, \tag{2.42}$$

which simply provides that

$$\phi_0(r_2) = c_0 + \frac{d_0}{r_2}, \tag{2.43}$$

where c_0, d_0 are constants of integration. Then, the next-to-leading order problem reads

$$\nabla^2_{r_2}\phi_1(r_2) = -\kappa(\Psi)\left(c_0 + \frac{d_0}{r_2}\right)^{5/2}. \tag{2.44}$$

Matching with the region I solution gives $c_0 = a_2$ and $d_0 = \Psi$ (see App. A for details).

From the large r_2 behaviour of the solution in this region, we conclude that the expansion here breaks down for $r_2 = O(\epsilon^{-1/2})$. We then require one final region to fully describe the solution to equation (2.16) in the current Regime 2.

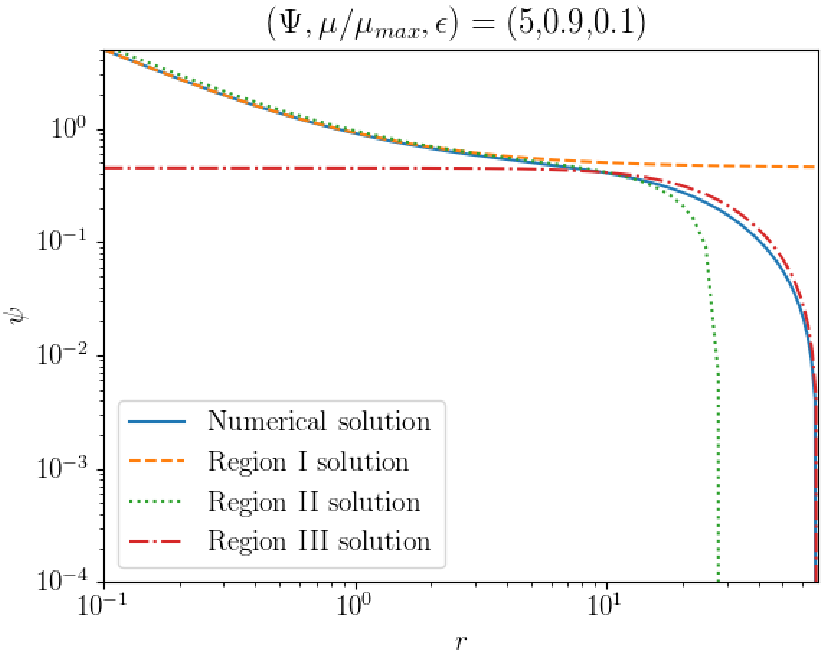

Figure 2.6: Numerical solution (solid) of the full Poisson equation (2.16) for a model in Regime 2, compared with the asymptotic solutions for the region I problem (dashed) stated at equation (2.28), the region II problem (dotted) stated at equation (2.41), and the region III problem (dot-dashed) stated at equation (2.45).

2.5.3 Region III

The final region that we consider requires the rescaling conditions $\psi^{(\mathrm{III})}(r_3) = \epsilon^2\phi(r_3)$, and $r_3 = \epsilon^{1/2}r_2$. We expand the Region II solution in terms of the new radial variable in order to set the relevant boundary conditions. This provides the leading-order problem for the region III as

$$\begin{aligned} \nabla^2_{r_3}\phi &= -\kappa(\Psi)\phi^{5/2}, \\ \phi(0) &= a_2, \\ \phi'(0) &= 0, \end{aligned} \tag{2.45}$$

which we solve numerically, with standard methods. A comparison between the numerical solution of the full Poisson equation (2.16) and the asymptotic solutions derived in Regions I, II, and III is illustrated in Fig. 2.6, for a model in the current Regime 2.

The region III problem stated at equation (2.45) should also be recognised as having the form of a King (1966) model (in the limit of small Ψ), with a_2 as the value of the central dimensionless escape energy. Thus, the physical interpretation formulated in Sect. 2.4.2 for the inner and outer solutions in Regime 1 applies to regions I and II (for the inner solution), and region III (for the outer solution) in the current Regime 2. The key difference here consists in the modification to the first boundary condition, where the constant a_2, defined

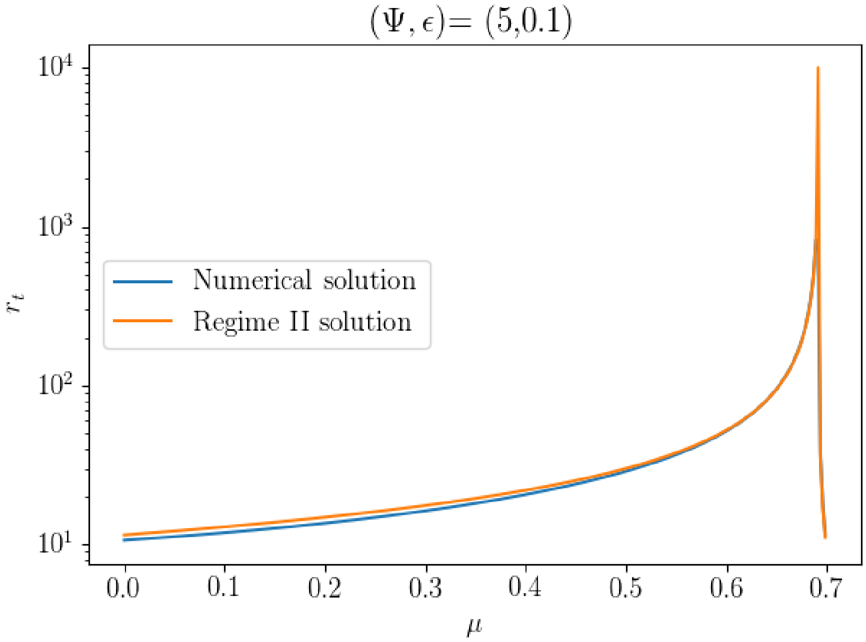

Figure 2.7: Comparison of the values of the truncation radius of the models obtained by numerically solving the full Poisson equation (2.16), and those determined in Regime 2, by solving either the region III problem (for $a_2 > 0$) as stated at equation (2.45) or the region I problem (for $a_2 < 0$) as stated at equation (2.28); for details about the two cases, see Sect. 2.5.1.

by equation (2.37), appears.

The constant a_2 now emerges as the most meaningful quantity for describing the sharp transition illustrated in Fig. 2.2. We already noted (at the end of Sect. 2.5.1) the existence of two cases, as distinguished by the sign of a_2. When a_2 is negative, the solution is fully described by the region I asymptotics; when a_2 is positive, the more extensive considerations formulated here and in Sect. 2.5.2 are required. Therefore, we expect the condition $a_2 = 0$ to deliver a well-posed prediction of the location of the sharp transition. In Fig. 2.7, we show that, for models with given values of (Ψ, ϵ), the values of the truncation radius predicted by the Regime 2 asymptotics are in excellent agreement with the ones from the full numerical solution and that, therefore, the condition $a_2 = 0$ captures the transition. In Fig. 2.8 we explore the efficacy of this condition over a more extensive set of values in the (μ, ϵ) plane, as well as for additional values of the central dimensionless escape energy, Ψ. Good agreement is obtained over a significant range of ϵ values, particularly for small ϵ where we expect the asymptotic treatment to be valid.

2.6 Regime 3: $a_2 = O(\epsilon^2)$

The final regime is defined by $a_2 = O(\epsilon^2)$ and requires only two asymptotic regions, again describing the inner and outer behaviour. This scaling will allow us to characterise the solution in the region around $a_2 = 0$. We can then describe

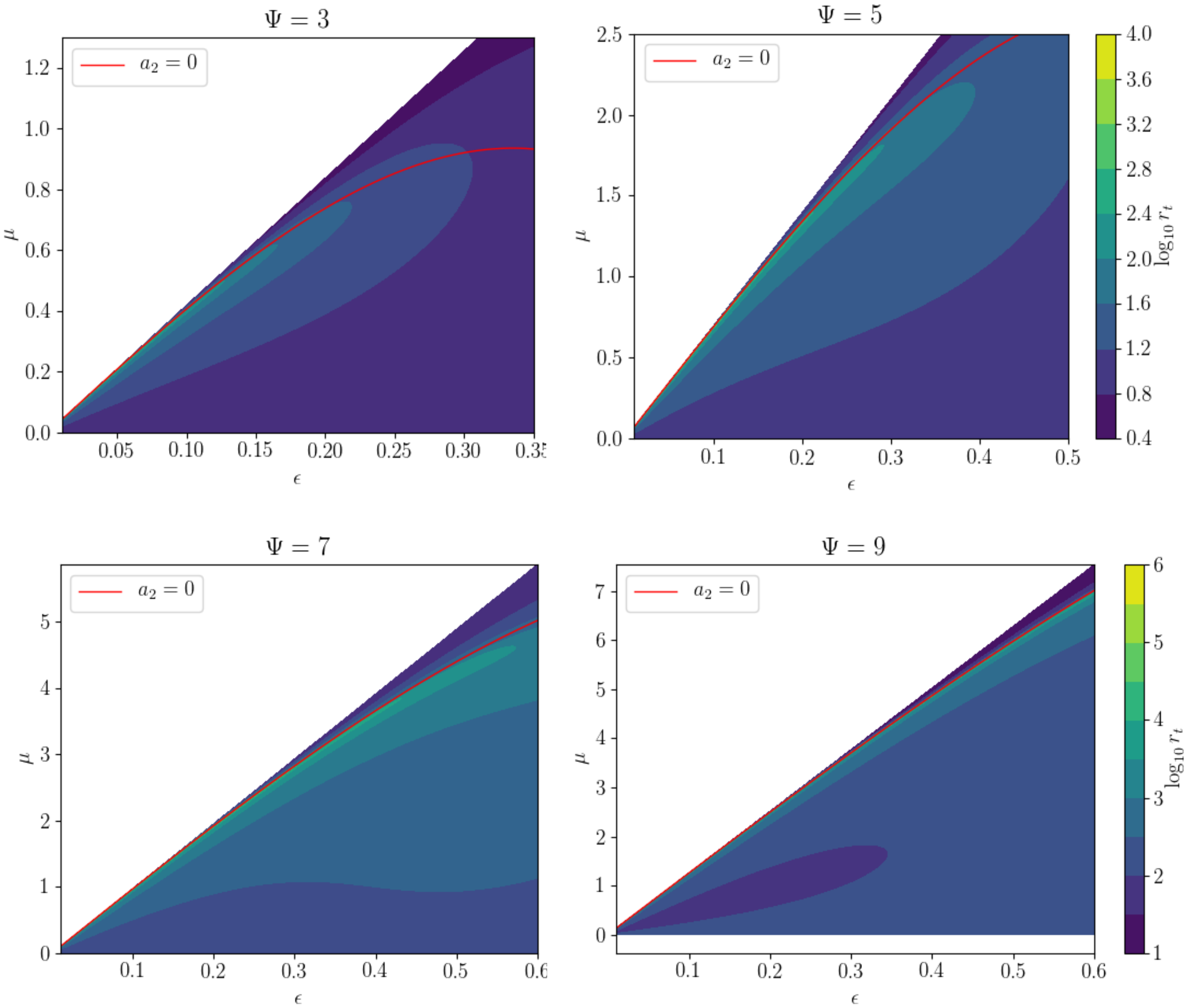

Figure 2.8: Contour plots of the truncation radius obtained by solving numerically the full Poisson equation (2.16). The red line indicates the condition $a_2 = 0$, which captures the sharp transition of the family of solutions over the entire (μ, ϵ) parameter space, also for several values of the central dimensionless escape energy, Ψ. The models depicted in Fig. 2.7 correspond to a vertical section (at $\epsilon = 0.1$) of the top right panel (for $\Psi = 5$).

the transitional peak seen in Fig. 2.2, in terms of its width, which is of $O(\epsilon^2)$ about $a_2 = 0$, and height, which can described as $r_t = O(\epsilon^{-3})$. In addition, this regime provides us with the opportunity to determine explicitly the critical value of μ_c at which the transition occurs, within a sequence of models with given values of ϵ and Υ. More concretely we pose that

$$a_2 = A_0 + C(\Upsilon) \equiv \epsilon^2 A_2 = O(\epsilon^2), \tag{2.46}$$

and begin by considering the behaviour of the solution in the central region.

2.6.1 Region I

We consider the radial scaling, $r_1 = \epsilon^{-1} r$ already employed in both Regimes 1 and 2 (see Sect. 2.4.1, 2.5.1). In Region I, the problem to be solved is then given by

$$\begin{aligned} &\nabla^2_{r_1} \psi^{(\mathrm{I})}(r_1) = -\epsilon^2 K\left(\psi^{(\mathrm{I})}, \Upsilon\right), \\ &\psi^{(\mathrm{I})}(1) = \Upsilon, \\ &\psi^{(\mathrm{I})\prime}(1) = -\Upsilon - C(\Upsilon)\epsilon^2 + A_2\epsilon^4, \end{aligned} \tag{2.47}$$

where we formulate explicitly the contributions at each order to the second boundary condition.

We look for a solution to equation (2.47) as an expansion in ϵ, with only even order terms, as in the previous two regimes. The leading and second-order contributions to $\psi^{(\mathrm{I})}$ are analogous to those seen in Regime 2, with $\psi^{(\mathrm{I})}_0(r_1) = \Upsilon/r_1$, and $\psi^{(\mathrm{I})}_2(r_1)$ obtained as a solution to

$$\begin{aligned} &\nabla^2_{r_1} \psi^{(\mathrm{I})}_2(r_1) = -K\left(\frac{\Upsilon}{r_1}, \Upsilon\right) \\ &\psi^{(\mathrm{I})}_2(1) = 0, \\ &\psi^{(\mathrm{I})\prime}_2(1) = -C(\Upsilon), \end{aligned} \tag{2.48}$$

so that we have

$$\psi_2(r_1) \sim \frac{b_2}{r_1} + 4\kappa\Upsilon^{5/2} r_1^{-1/2}. \tag{2.49}$$

for $r_1 \to \infty$. Compared to the previous derivations, the main difference in the current Regime 3 is the presence of a non-trivial boundary condition in the fourth-order problem, which reads

$$\nabla^2_{r_1} \psi^{(\mathrm{I})}_4(r_1) = -\frac{9}{\rho(\Upsilon)}\left(\rho\left(\frac{\Upsilon}{r_1}\right) + \Upsilon^{3/2} r_1^{-3/2}\right)\psi^{(\mathrm{I})}_2(r_1),$$

$$\psi^{(\mathrm{I})}_4(1) = 0, \tag{2.50}$$

$$\psi^{(\mathrm{I})\prime}_4(1) = A_2. \tag{2.51}$$

As in the case of equation (2.36) in Regime 2, we now consider the large radius behaviour of the solution

$$\begin{aligned}\psi_4^{(\mathrm{I})}(r_1) \sim a_4 - 10\kappa^2\Psi^4 \ln r_1 + \frac{b_4}{r_1} - \frac{10}{3}\kappa\Psi^{5/2}b_2 r_1^{-3/2} \\ + 10\kappa\Psi^{3/2}b_2 r_1^{-1/2} + 10\kappa^2\Psi^5\frac{\ln r_1}{r_1}\end{aligned} \tag{2.52}$$

where

$$\begin{aligned}a_4 &= A_2 + 10\kappa^2\Psi^4 - \frac{5}{2}\kappa\int_1^\infty s\left[\left(\rho\left(\frac{\Psi}{s}\right) + \Psi^{3/2}s^{-3/2}\right)\psi_2^{(\mathrm{I})}\right. \\ &\left.-4\kappa\Psi^4 s^{-2}\right]\mathrm{d}s, \\ &\equiv A_2 + D(\Psi)\end{aligned} \tag{2.53}$$

and

$$\begin{aligned}b_4 = &-A_2 + 5\kappa b_2\left(\Psi^{5/2} - \Psi^{3/2}\right) - 10\kappa^2\Psi^4 \\ &+ \frac{5}{2}\kappa\int_1^\infty s^2\left[\left(\rho\left(\frac{\Psi}{s}\right) + \Psi^{3/2}s^{-3/2}\right)\psi_2^{(\mathrm{I})}\right. \\ &\left.- \left(\Psi^{5/2}s^{-5/2} + \Psi^{3/2}s^{-3/2}\right)\left(\frac{b_2}{s} + 4\kappa\Psi^{5/2}s^{-1/2}\right)\right]\mathrm{d}s,\end{aligned} \tag{2.54}$$

are the relevant integration constants, expressed in closed form, which have been obtained analogously to the constants reported at equations (2.37) and (2.38). This is a complicated expression. However, to obtain the boundary conditions for the Region II problem, only the first two terms are of interest as they dominate the expression for large radii.

2.6.2 Region II

Recall that, in Regime 3, we expect the asymptotic solution in region I to become invalid for $r_1 = O(\epsilon^{-4})$, hence we let $r_2 = \epsilon^4 r_1$ and $\phi(r_2) = \epsilon^{-4}\psi^{(\mathrm{II})}(r_2)$. Under such rescaling conditions, the Poisson equation reads

$$\nabla_{r_2}^2\phi = -\kappa\phi^{5/2}. \tag{2.55}$$

By writing the large radius behaviour of the Region I solution in terms of the Region II variables stated above, we obtain the following small radius behaviour of the leading-order solution in Region II

$$\phi \sim a_4 + 40\kappa^2\Psi^4\ln(\epsilon) + \frac{\Psi}{r_2} + 4\kappa\Psi^{5/2}r_2^{-1/2} - 10\kappa^2\Psi^4\ln r_2, \tag{2.56}$$

as $r_2 \to 0$. The logarithmic term appearing here is a direct consequence of the rescaling of the logarithmic term which emerged in the Region I solution equation (2.52). This expression now acts as the appropriate boundary condition

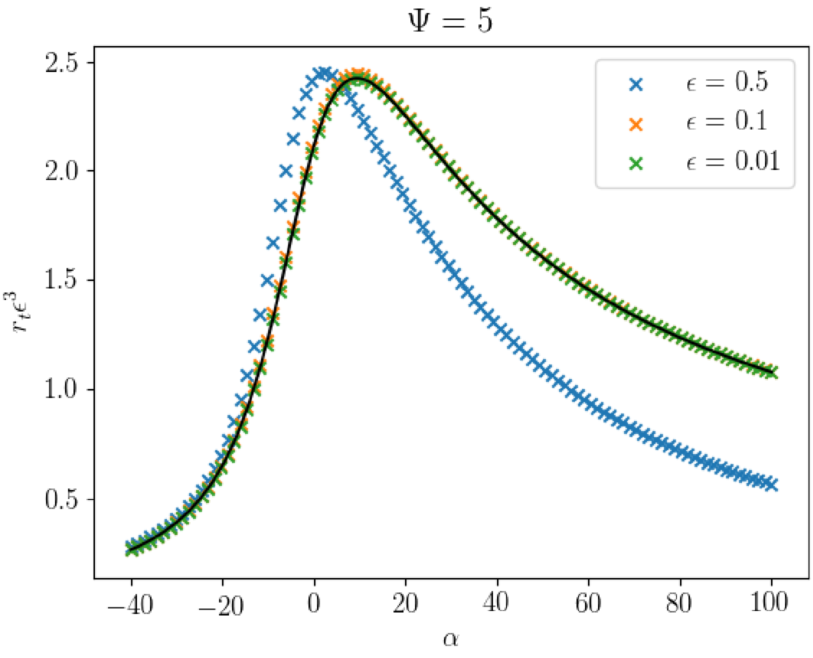

Figure 2.9: Truncation radius (rescaled in ϵ) as a function of $\alpha \equiv a_4 + 40\kappa^2\Psi^4 \ln \epsilon$, for fixed value of Ψ. The values of r_t are obtained via the numerical solution of equation (2.55). Three values of ϵ are considered, with the largest one (blue crosses) deliberately beyond the validity limit of the Regime 3 asymptotics. The ϵ-independent asymptotic result obtained in Regime 3 (see Sect. 2.6.2) is shown by the black line.

for equation (2.55).

To assess the appropriateness of the scaling conditions introduced above, in Fig. 2.9 we examine the behaviour of $r_t\epsilon^{-3}$ against the quantity $\alpha \equiv a_4 + 40\kappa^2\Psi^4 \ln \epsilon$, which is the constant term in equation (2.56), for a fixed value of Ψ and progressively larger values of ϵ, up to the validity limit of the asymptotic description. For small values of ϵ, the behaviour of the truncation radius (as a function of α) becomes independent of ϵ, attesting that the asymptotics introduced in the current Regime 3 accurately capture the solutions at the location of the transition.

This result provides us with the opportunity to determine explicitly the critical value of μ_c at which the transition occurs, within a sequence of models with given values of ϵ and Ψ (e.g., see Fig. 2.11). Now, the Poisson equation (2.55) and associated boundary condition (2.56) defines a two-parameter family of solutions. The boundary condition in compact form reads as $\phi \to \alpha + F(\Psi, r_2)$ for $r_2 \to 0$, where $F(\Psi, r_2) \equiv \Psi/r_2 + 4\kappa\Psi^{5/2}r_2^{-1/2} - 10\kappa^2\Psi^4 \ln r_2$, and $\alpha \equiv a_4 + 40\kappa^2\Psi^4 \ln \epsilon$. In this expression, we do not include any term explicitly depending on ϵ, the dependence is implicit in the value of α.

This problem, therefore, is solved over a range of values of (α, Ψ). For a given value of the central dimensionless escape energy, Ψ, we obtain the critical value of $\alpha = \alpha_c(\Psi, \mu)$, which corresponds to the value at which the maximum of the curve illustrated in Fig. 2.9 occurs.

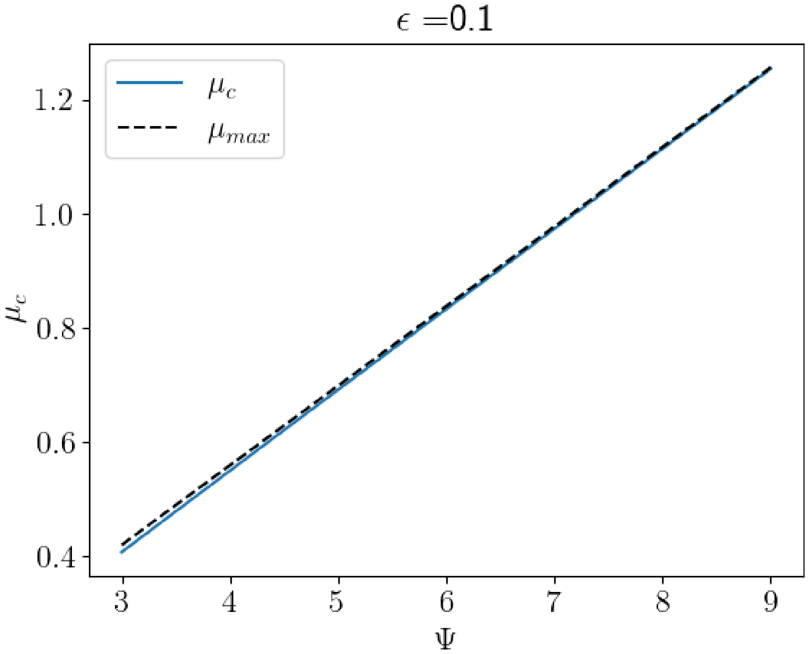

Figure 2.10: Critical values of μ, μ_c, as a function of central concentration Ψ, for fixed ϵ. We also plot the maximum value of μ, μ_{max}, recalling that $\mu_{max} = 4\pi\epsilon\Psi/9$.

Then for any value of ϵ within the validity of the asymptotics, we can calculate the corresponding critical value of A_2 as $A_{2c} = \alpha_c - D(\Psi) - 40\kappa^2\Psi^4 \ln \epsilon$, by using equation (2.53) and the definition of α. Equation (2.37) provides that $A_{0c} = \epsilon^2 A_{2c} - C(\Psi)$, and, finally, we use the definition of a_0 to recover

$$\mu_c = \frac{4\pi\epsilon}{9}(\Psi - A_{0c}\epsilon^2), \tag{2.57}$$

which, expressed explicitly as a power series in ϵ, reads

$$\begin{aligned} \mu_c = \frac{4\pi\epsilon}{9} \Big(&\Psi + \epsilon^2 C(\Psi) + \epsilon^4 \ln \epsilon \, 40\kappa^2\Psi^4 \\ &- \epsilon^4(\alpha_c - D(\Psi)) \Big) . \end{aligned} \tag{2.58}$$

We plot these critical values of μ, for a fixed ϵ, over a range of Ψ values in Fig. 2.10, noting the slight divergence from the maximum value of μ as a result of the higher order corrections in Eq. (2.58). These corrections are comparatively larger in magnitude for lower values of the central concentration Ψ.

In this section, we have achieved a detailed characterisation of the sharp transition observed in this family of LoKi models, as first illustrated in Fig. 2.2. We have shown that such a transition exists. Further, we have derived the scaling in ϵ associated with this transition, specifically that the transition corresponds to systems with large extents of $O(\epsilon^{-3})$ over a very narrow range of parameters. The asymptotic description formulated here allows us to quantify the behaviour of several physical properties of the equilibria, including for cases in close proximity to the transition, as we describe in the next sections.

2.7 Properties of the models

2.7.1 Intrinsic properties

We compute the dimensionless density profiles (see Fig. 2.11), which are given by equation (2.3), and the corresponding dimensionless scalar velocity dispersion profiles (see Fig. 2.12), which we recall are defined by

$$\sigma^2(\psi) = \frac{2}{5}\frac{\gamma\,(7/2,\psi)}{\gamma\,(5/2,\psi)}. \tag{2.59}$$

The models are illustrated as a sequence of equilibria with increasing values of μ and fixed values of $\{\Psi, \epsilon\}$, i.e. as a generalisation of the parametrisation in Ψ which is usually adopted for the classic King (1966) models. An alternative parametrisation can also considered, by defining a sequence of equilibria with fixed values of $\{a_0, \epsilon\}$ and increasing values of Ψ, which, under such conditions, correspond to increasing values of μ. The latter parameterisation enables a more meaningful comparison of the structural and kinematic properties of models as characterised by increasing masses of the central black holes.

Nonetheless, some care is needed in interpreting the sequence with fixed $\{a_0, \epsilon\}$: the outer regions of the models (see bottom panels of Fig. 2.11, 2.12) appear to be evenly spaced as a result of the specific definition of the scale radius, r_K, adopted in the dimensionless formulation of the Poisson equation (2.16); such scale radius indeed depends upon Ψ, through $\rho_0 = \rho(\Psi)$. This further demonstrates that the asymptotic description of the outer region in Regime 1 (see equation (2.26)) appropriately captures the behaviour of the solutions close to the truncation radius, as, in the outer problem, only $\rho(\Psi)$ varies, when a_0 is kept constant.

Indeed, for a large portion of the parameter space, there is little difference between the outer region of a King (1966) model with a given value of Ψ and an equilibrium with a central black hole with a mass such that $a_0 = \Psi$, while, close to the origin, the behaviour of the models is significantly different.

Conversely, the models located beyond the transition at $\mu = \mu_c$ (see Fig. 2.8) show a drastically different structure (e.g., see the model with the largest μ value in the top panels of Fig. 2.11 and 2.12). As noted in Sect. 2.5.1, these models are well described solely by the innermost asymptotic solution of Regime 2, and, as such, they have no discernible core and represent systems that are fully dominated by the central black hole. In both cases, the models are characterised by the steep central gradients in the intrinsic density and velocity dispersion profiles. An approximate expression of their behaviour is obtained by expanding the relevant moment in a Taylor series in the vicinity of the inner boundary. For

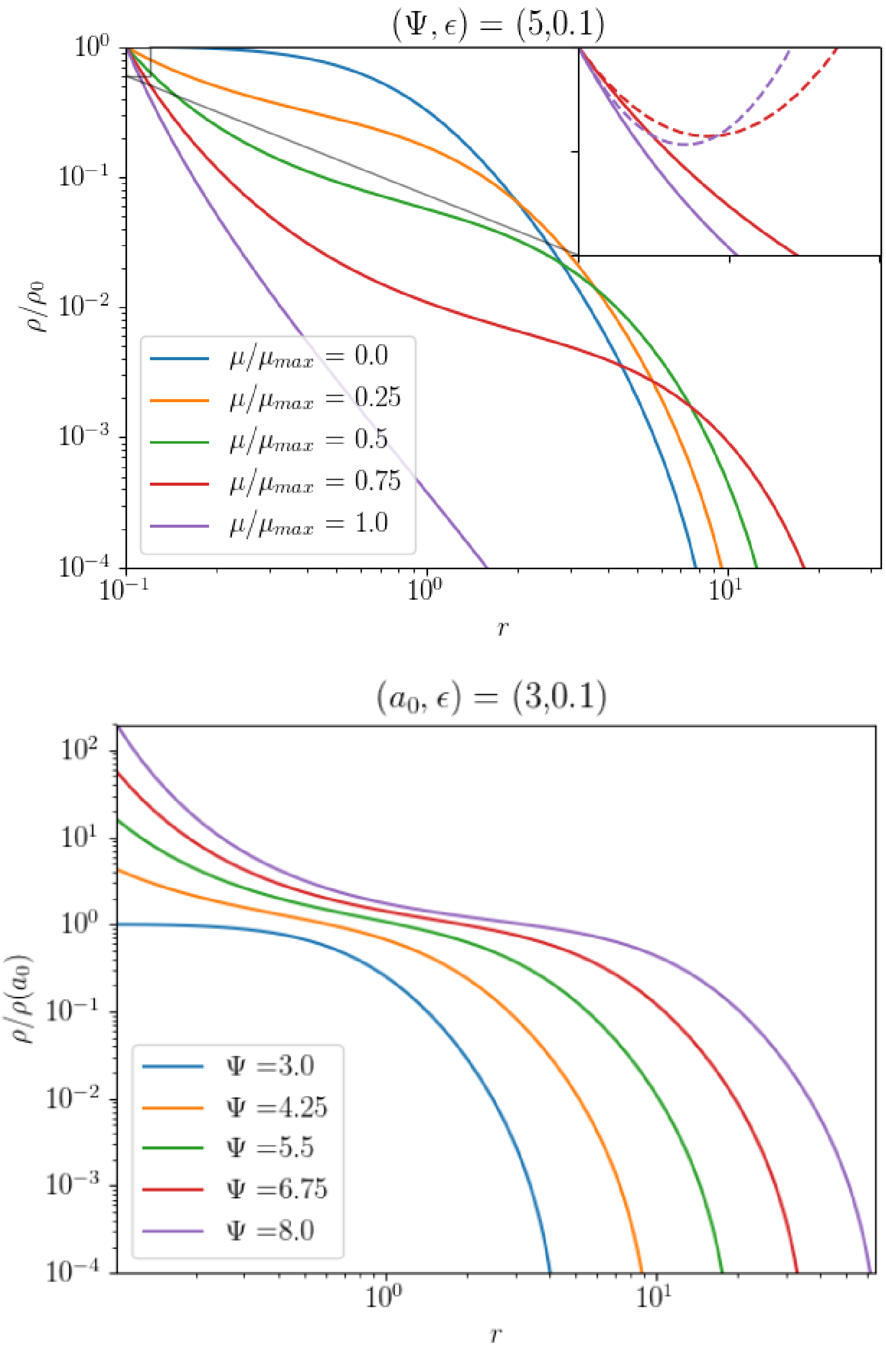

Figure 2.11: Dimensionless intrinsic density profiles as functions of the dimensionless radius. The profiles are obtained via equation (2.3), by using the numerical solution of the full Poisson equation (2.16); for the corresponding dimensionless escape energy profiles, see Fig. 2.1. **Top:** Ψ and ϵ have been held constant, while increasing μ with the range of validity $[0, \mu_{\max}(\Psi, \epsilon)]$; the profiles are normalised to the value $\rho_0 = \rho(\Psi)$. The dashed lines in the inset panel show the approximate behaviour of the density in the central regions, as stated in equation (2.60). The transition observed at μ_c occurs between $0.75\mu_{\max}$ and $\mu_{\max}$. **Bottom:** a_0 and ϵ are held constant while increasing Ψ; the profiles are normalised to the value $\rho(a_0)$. At fixed values of a_0 and ϵ, increasing values of Ψ correspond to higher values of μ and the case with $\mu = 0$ is given by the model with $\Psi = a_0 = 3$ (blue). For consistency, the value $\epsilon = 0.1$ is maintained also for models with $\mu = 0$, in both panels.

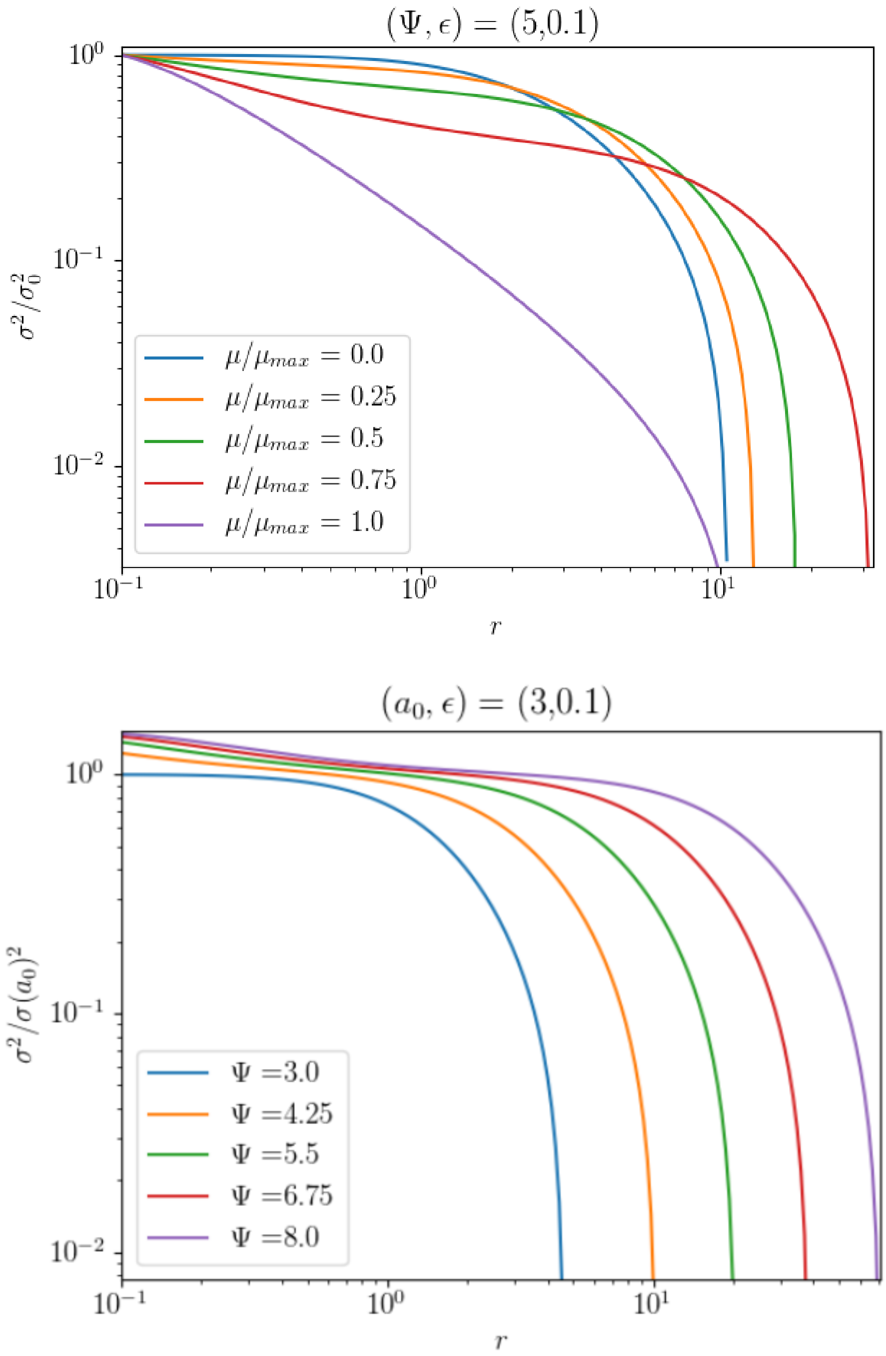

Figure 2.12: Dimensionless intrinsic velocity dispersion profiles as functions of the dimensionless radius. The profiles are obtained via equation (2.5), by using the numerical solution of the full Poisson equation (2.16). The models in the top and bottom panels are the same as in Fig. 2.11.

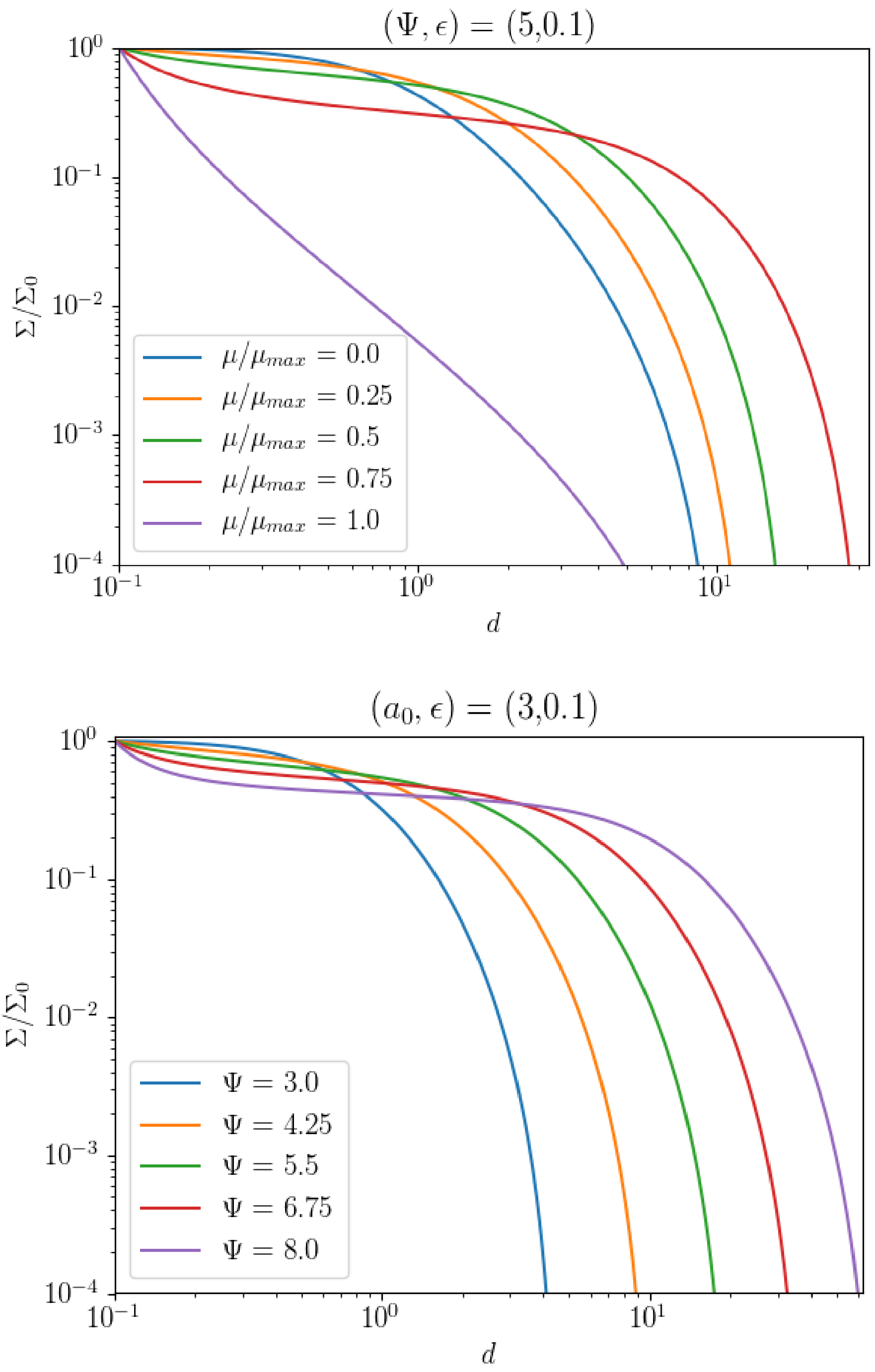

Figure 2.13: Projected density profiles, normalised to their central value, as functions of the dimensionless projected radius, d (see equation (2.61)). As in Figs. 2.11, 2.12, for the models in the top panel, Ψ and ϵ have been held constant, while increasing μ within the range of validity $[0, \mu_{\max}(\Psi, \epsilon)]$. In the bottom panel, we have held a_0 and ϵ constant, while increasing Ψ.

instance, the density profile near $r_1 = 1$ is provided by

$$\rho(r_1) = \rho(\Upsilon) - \frac{9\mu}{4\pi\epsilon}\left(\rho(\Upsilon) + \Upsilon^{3/2}\right)(r_1 - 1) + O\left((r_1 - 1)^2\right). \tag{2.60}$$

This is already a marked departure from the usual King (1966) models for which there is no contribution at first-order; in principle, by adding higher-order terms further deviations from the classical case arise.

For clarity, we remark that, in the limit of vanishing black hole mass, defined by $\mu \to 0$ and $\epsilon \to 0$, the models considered here reduce to the King (1966) models. At the opposite extreme of the parameter space, we emphasise that, for given values of $\{\Upsilon, \epsilon\}$, there exists a maximum value for the black hole mass $\mu = \mu_{\max}(\Upsilon, \epsilon) = (4\pi/9)\Upsilon\epsilon$, such that $a_0 = \Upsilon - 9\mu_{\max}/4\pi\epsilon = 0$. In this case, the equilibrium is characterised by a quasi-Keplerian behaviour, where the surrounding stars act as a tracer density in the potential generated by the central black hole. This can be appreciated by observing that, for cases where Υ/r_1 is the dominant contribution, the Region I asymptotics in Regime 2 well describe the solution, with the second-order correction being provided solely by the response of the system due to this potential (see equation (2.32)).

2.7.2 Projected properties

To facilitate the comparison of the models to observational data, we also compute the projection on the plane of the sky of the intrinsic moments, to characterise the relevant structural and kinematic observables. The projected density profiles, which are illustrated in Fig. 2.13, have been obtained by integrating the intrinsic density along the line of sight

$$\Sigma(d) = \int_{-z_e}^{z_e} \rho(r_p)\mathrm{d}z, \tag{2.61}$$

where d is the projected radius on the plane of the sky, z is the distance along the line of sight, $r_p = \sqrt{d^2 + z^2}$ is the radius corresponding to a given point on the line of sight, and $z_e = \sqrt{r_t^2 - d^2}$ corresponds to the edge of the system along the line of sight. We observe that models with significant black hole masses manifest a substantial central slope also in projection, however, the steepness of such a slope is generally suppressed by the projection process when compared to the intrinsic profiles.

Similarly, the projected velocity dispersion profiles, which are shown in Fig. 2.14, are obtained by direct integration along the line of sight as

$$\sigma_d^2(d) = \frac{1}{\Sigma(d)}\int_{-z_e}^{z_e} \sigma^2(r_p)\rho(r_p)\mathrm{d}z, \tag{2.62}$$

and equivalent remarks about the significance of the steepness of the central slope in projection apply here.

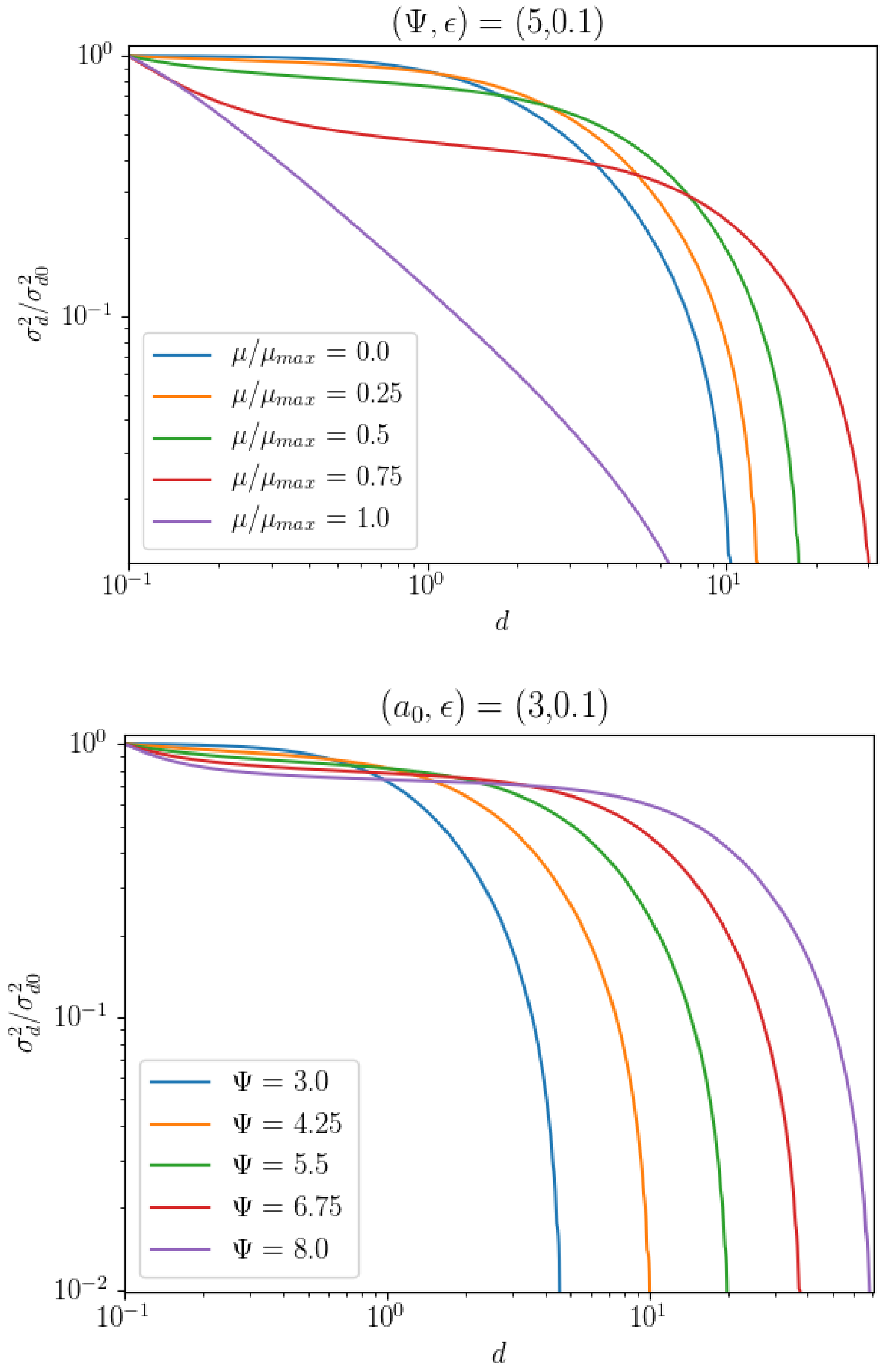

Figure 2.14: Projected velocity dispersion profiles, normalised to their central value, as functions of the dimensionless projected radius, d. The same models illustrated in Fig. 2.13 are displayed here.

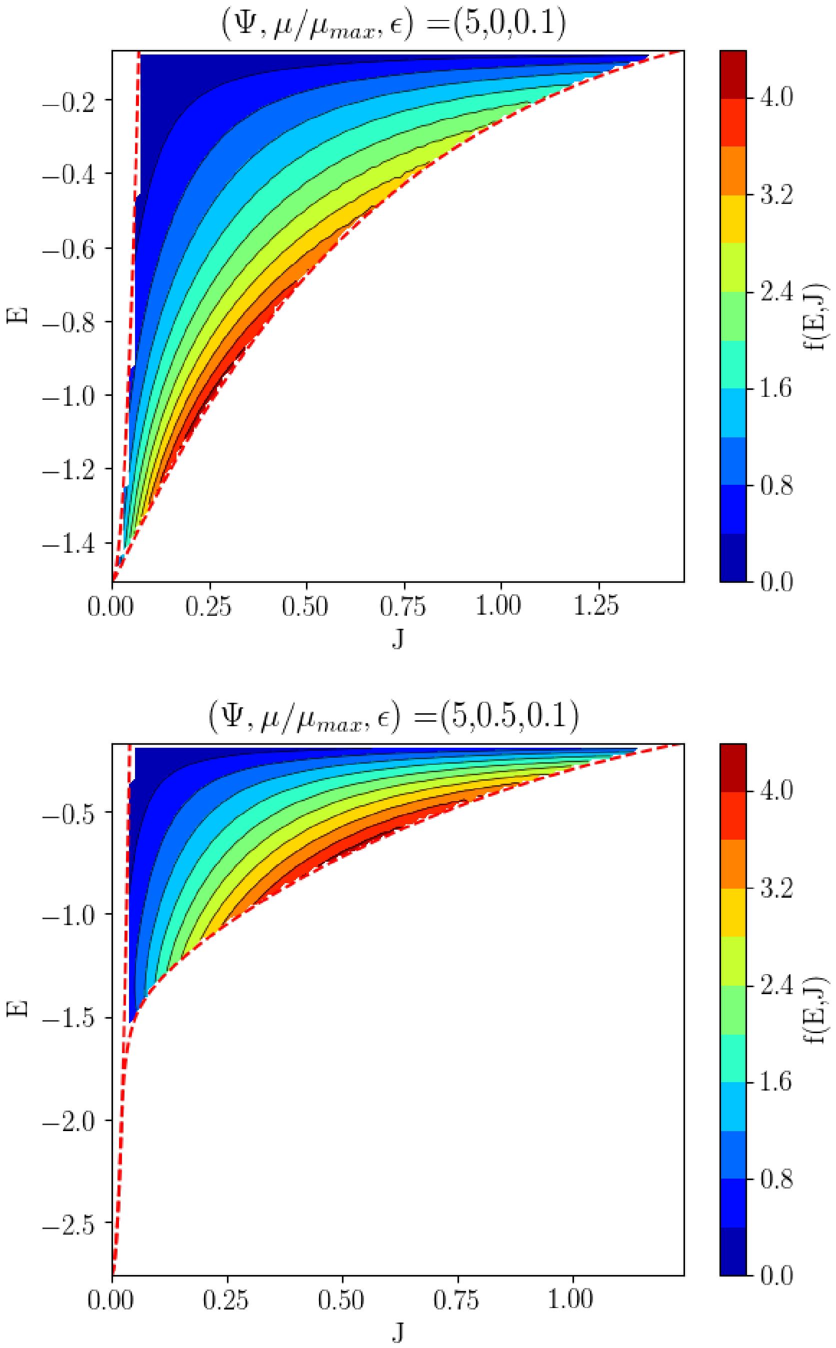

Figure 2.15: Lindblad diagrams for two models with a dimensionless black hole mass $\mu/\mu_{\text{max}} = 0$ (top) and $\mu/\mu_{\text{max}} = 0.5$ (bottom). E and J denote the single-star energy and angular momentum, expressed in dimensional units. The red dashed line on the left represents the inner boundary, which excludes orbits with periapsis smaller than ϵ; the red dashed line on the right denotes the centrifugal barrier determined by circular orbits. For the case of $\mu/\mu_{\text{max}} = 0$, we have maintained the value $\epsilon = 0.1$ to highlight the impact of the location of the boundary conditions in equation (2.16) in determining the existence of the inner boundary on the left of the diagram. The model with $\mu/\mu_{\text{max}} = 0.5$ can penetrate much deeper energy states, at very low values of angular momentum.

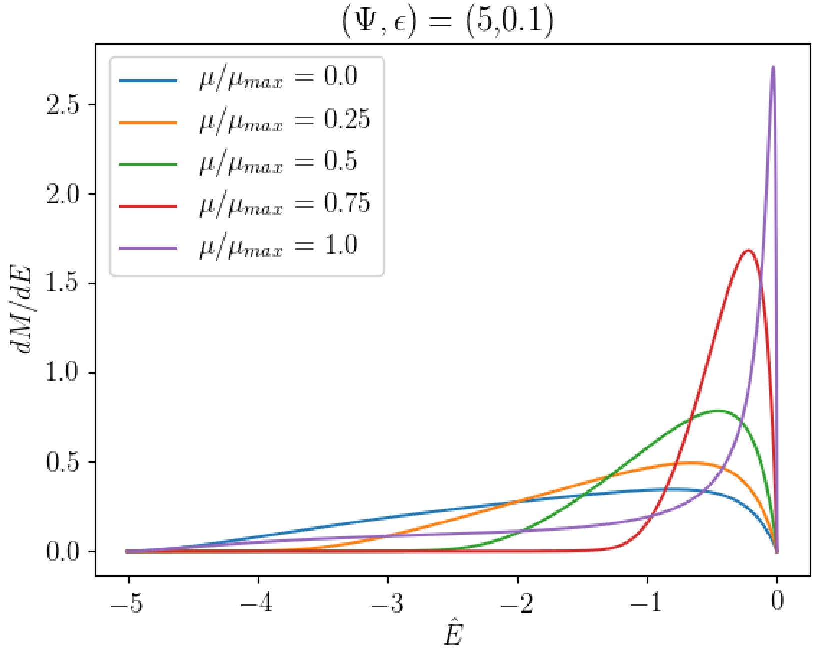

Figure 2.16: Differential energy distribution for models with fixed values of $\{\Psi, \epsilon\}$ and increasing values of μ, as displayed in the top panels of Figs. 2.1, 2.11-2.14. The curves are expressed in physical units on the y-axis, and dimensionless units on the x-axis. They have been further rescaled so that they integrate to unity.

2.7.3 Phase space properties

The presence of a central black hole affects the overall phase space distribution of an equilibrium. To assess the impact on the orbital architecture of a system, we compare the phase space distribution in energy and angular momentum ("Lindblad diagrams") of two models with the same values of $\{\Psi, \epsilon\}$ and dimensionless black hole masses of $\mu/\mu_{\rm max} = 0$ and $\mu/\mu_{\rm max} = 0.5$. In Fig. 2.15, we provide contour plots of

$$\tilde{f}(E, J) = \int \delta\left(E - \left(\frac{1}{2}v^2 + \Phi(r)\right)\right) \delta(J - r v_t) f(\boldsymbol{r}, \boldsymbol{v}) \mathrm{d}^3\boldsymbol{v}\mathrm{d}^3\boldsymbol{r}, \tag{2.63}$$

where v_t is the tangential component of the velocity vector and E and J denote the single-star energy and angular momentum, which, for convenience, are expressed in dimensional units. These quantities are related to the dimensionless single-star energy and angular momentum as $E = \hat{E}/a + E_0$ and $J = r_K \hat{J}/\sqrt{a}$. Integrating over the velocity space and writing the spatial integral in dimensionless units, we obtain that

$$\tilde{f}(E, J) = 16 r_K^2 \pi^2 J f_K(E) \int_{r_{\rm peri}}^{r_{\rm apo}} \left(2(\hat{E} + \psi(r)) - \frac{\hat{J}^2}{r^2}\right)^{-1/2} \mathrm{d}r, \tag{2.64}$$

where r is the dimensionless radius and $r_{\text{apo}}, r_{\text{peri}}$ are the dimensionless apoapsis and periapsis of an orbit indexed by (E, J).

The domain of the equilibria is defined by several demarcations (depicted as red dashed lines in Fig. 2.15). The right boundary is often referred to as the "centrifugal barrier", as it represents the largest possible magnitude of the single-star angular momentum J, for a given single-star energy E, and, therefore, it corresponds to circular orbits. The left boundary is determined by the existence of a minimum radius (at which the boundary conditions of the full Poisson problem at equation (2.16) are applied) and it excludes those orbits whose periapsis lies below ϵ. Finally, there is one further boundary at $E = 0$, which is induced by the presence of the truncation in energy space, as imposed by equation (2.1).

We observe that the presence of a central black hole causes a significant difference in the portion of phase space available to the models, especially concerning the most bound orbits, which, in the case of a system with a central black hole, can reach much deeper energy states. This deep energy penetration at very low values of angular momentum corresponds to preferentially radial orbits, which, in turn, are responsible for sculpting the steep central gradients observed in the intrinsic and projected properties of the models. Conversely, in the proximity of the upper boundary at $E = 0$, the phase space density of the models is similar. For the non-extreme black hole masses plotted here this corresponds to the fact that, close to the truncation radius, the system is only mildly affected by the presence of the central black hole, as discussed also in the analysis of the intrinsic density profiles in Sect. 2.7.1. However, the general character of the phase space distribution is broadly preserved, especially concerning the presence of a concentration of phase space density towards the centrifugal barrier, which is observed in both cases.

To characterise the phase space distribution of models with black hole masses up to the maximum value allowed, we compute the one-dimensional differential energy distribution, which is defined as

$$\frac{\mathrm{d}M}{\mathrm{d}E} \equiv f_K(E)g(E), \tag{2.65}$$

where $g(E)$ is the density of states given by

$$g(E) = 16\pi^2 \int_{r_{\min}}^{r_\Phi} r^2 \sqrt{2(E - \Phi(r)}\mathrm{d}r, \tag{2.66}$$

where r_Φ is the radius at which $\Phi = E$. The models presented in Fig. 2.16 illustrate that systems with larger values of black hole masses can access orbits which are progressively more bound (the differential energy distributions depicted there have been been further rescaled so that they integrate to unity, to facilitate the visual comparison).

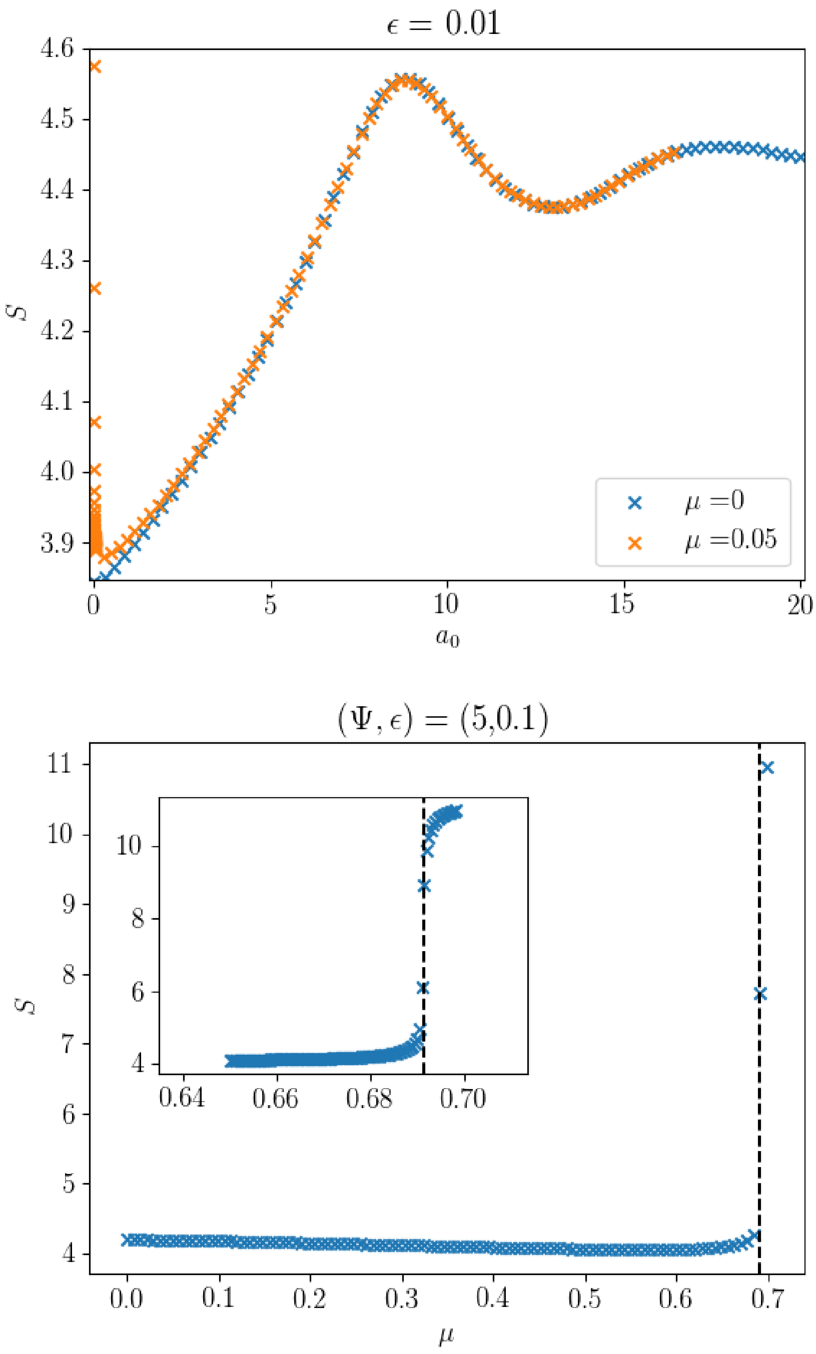

Figure 2.17: Top: Entropy as a function of a_0 for models with non-vanishing black hole mass and fixed ϵ, compared with models with $\mu = 0$. Recall that a_0 is positive definite (see Sect. 2.2.2). The rapid growth at small a_0 indicates proximity to the transition (for details, see Sect. 2.8.1). **Bottom:** Entropy as a function of μ for models with fixed $\{\Psi, \epsilon\}$. The black dashed line indicates the critical dimensionless black hole mass, calculated via equation (2.57); the inset shows a magnified view of the small region around $\mu = \mu_c$.

2.8 Thermodynamical characterisation

2.8.1 Entropy

We compute the Boltzmann entropy of the equilibria by direct integration of the distribution function over the relevant domain in phase space

$$S = -\int f(\boldsymbol{r},\boldsymbol{v}) \ln f(\boldsymbol{r},\boldsymbol{v}) \, \mathrm{d}^3\boldsymbol{v}\mathrm{d}^3\boldsymbol{r}. \tag{2.67}$$

In the top panel of Fig. 2.17, we present the value of the entropy as a function of a_0 for models with a fixed value of ϵ and a non-vanishing value of the black hole mass ($\mu = 0.05$), directly compared with the equivalent models without black holes ($\mu = 0$).

As noted in Sect. 2.4.2, for given values of ϵ and μ, the parameter a_0 can be interpreted here as the appropriate value of the central dimensionless escape energy, which corresponds to the usual parameter Ψ in the case of $\mu = 0$.

Indeed, the behaviour of the entropy as a function of a_0 in the case of the models with $\mu = 0$ is consistent with that of the entropy of the classic King (1966) models, as a function of Ψ (for reference, see, e.g., Fig. 16 in Chavanis et al. 2015a). Now, the parameterisation of the entropy in terms of a_0 has been chosen specifically to highlight one of the key results from Regime 1 asymptotics: in Fig. 2.17, with the exception of small values of a_0, the entropy values of the models are indistinguishable.

This observation further supports our previous conclusion that, in a large portion of the domain (Region II) of an equilibrium in Regime 1, the effect of the black hole is limited to a modification of the central dimensionless escape energy, with a_0 rather than Ψ.

By considering progressively smaller values of a_0, the entropy of the models differ significantly: this is a manifestation of the sharp transition of the family of solutions, where the Regime 1 asymptotics break down, and Regimes 2 and 3 are necessary.

This observation becomes even more evident when the values of the entropy are computed as a function of the black hole mass μ, for models with fixed $\{\Psi, \epsilon\}$.

In the bottom panel of Fig. 2.17, there is a sharp increase of the value of the entropy precisely at the critical value $\mu = \mu_c$. This transition in entropy motivates us to pursue a final layer of physical interpretation of this family of models, in terms of a thermodynamical description.

2.8.2 Caloric curves

Following Chavanis et al. (2015a) (see especially Secs. III, D and E), we introduce the inverse temperature

$$\beta \equiv aG^2 M_C^{4/3} (8\sqrt{2}\pi A e^{-aE_0})^{2/3} = \frac{81 \cdot 3^{2/3}}{16\pi^2} \frac{\hat{M}_C^{4/3}}{\hat{\rho}(\Psi)^{2/3}}, \tag{2.68}$$

and total energy

$$\mathcal{E} \equiv -\frac{E_{tot}}{G^2 M_C^{7/3} (8\sqrt{2}\pi A e^{-aE_0})^{2/3}} = -\frac{2\pi}{3^{8/3}} \frac{\hat{\rho}(\Psi)^{2/3} \hat{U}}{\hat{M}_C^{7/3}}, \tag{2.69}$$

where hats explicitly denote dimensionless quantities. Here, E_{tot} is the total energy defined in the usual manner as

$$E_{tot} = T + U, \tag{2.70}$$

where T and U are the total kinetic energy and gravitational potential energy of the system. To obtain the second equality in (2.69) we also utilise the virial theorem (Heggie & Hut 2003)

$$2T + U = 0, \tag{2.71}$$

to eliminate the need to explicitly calculate the total kinetic energy of the stellar system. The only quantity appearing here which has not been defined yet is $\hat{U}$, the dimensionless total potential energy of the system, which is related to the total potential energy via

$$U \equiv -4\pi G \int_{r_{\min}}^{r_t} r\rho(r) M_C(r) \mathrm{d}r = G r_K^5 \rho_0^2 \hat{U}. \tag{2.72}$$

In Fig. 2.18, we show the caloric curves $\beta = \beta(\mathcal{E})$ for several equilibria. In the top panel, the models are parametrised by a_0, for fixed values of (μ,ϵ); in the bottom panel, the models are parametrised by μ, for fixed values of (Ψ, ϵ), to facilitate a direct comparison with the other structural and kinematic properties of the models, as described in Sect. 2.7. Below we focus on the behaviour of the models parametrised by a_0.

Models with $\mu = \epsilon = 0$ (i.e. classic King 1966 models) behave as truncated isothermal spheres, parameterised by Ψ. For small values of Ψ, the equilibria behave approximately as a polytrope with index $n = 5/2$ (see Chavanis et al. 2015a, equation (86)). For large values of Ψ, the models wrap around a singular point $(\mathcal{E}_S, \beta_S)$, which corresponds to a singular isothermal sphere (i.e. a polytrope with index $n \to +\infty$; for a derivation of this limit, see Hunter 2001). This behaviour is sometimes referred to as a "cold spiral" because it occurs at low temperatures and for non-relativistic self-gravitating systems. The extrema of this spiral encode various stability conditions in the canonical and microcanonical ensemble descriptions (for a comprehensive study of the thermodynamical properties of the King (1966) models, see Chavanis et al. 2015a, extending some early work by Katz 1980). Here we simply recall that equilibrium states exist only above a critical energy $\mathcal{E}_c$ in the microcanonical ensemble, and only above a critical temperature $T_c = 1/\beta_c$ in the canonical ensemble, where $(\mathcal{E}_c, \beta_c)$ corresponds to the rightmost turning point of the spiral. For $\mathcal{E} < \mathcal{E}_c$, the system undergoes a gravothermal catastrophe and, for $T < T_c$, it undergoes an isothermal collapse.

Models with non-vanishing values of μ, parameterised by a_0, show a more

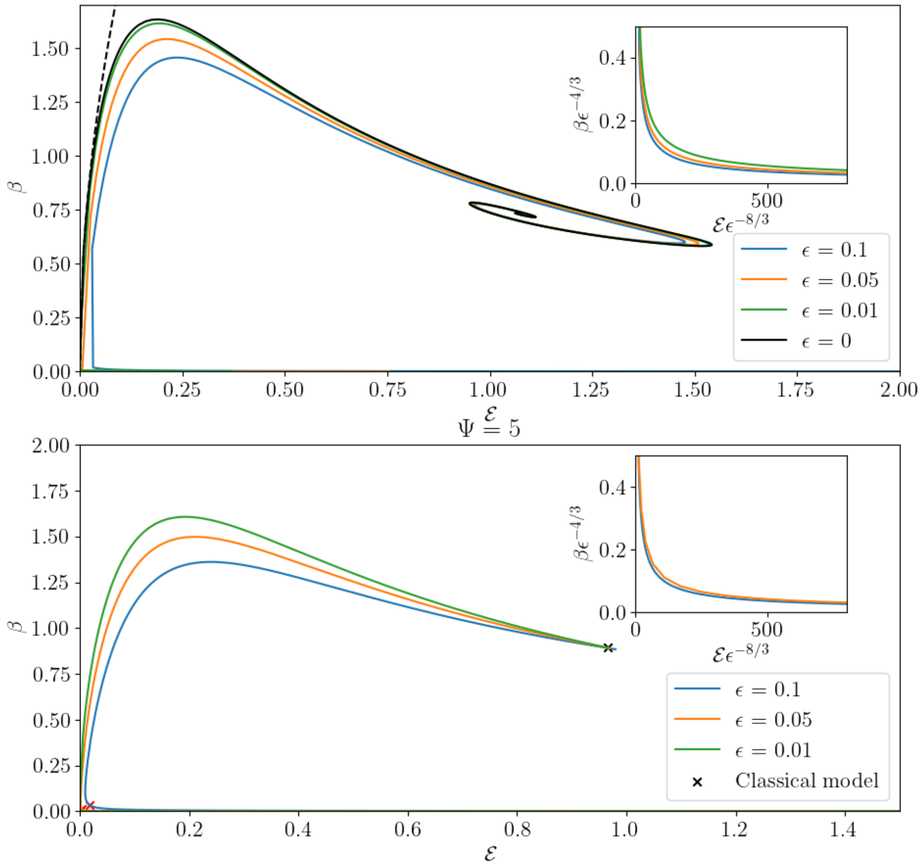

Figure 2.18: Caloric curves, i.e. the inverse temperature, β, as a function of the total energy, $\mathcal{E}$ (for definitions, see Sect. 2.8.2) computed for several equilibria. **Top:** Models with fixed values of $\{\mu,\epsilon\}$, parameterised by a_0. For large values of a_0, the models share the same "cold spiral" behaviour; to progress around the spiral in an anti-clockwise direction from the centre corresponds to decreasing values of central dimensionless escape energy, from $\Psi = 30$ to some $\Psi_{\rm min}$. This minimum value of Ψ, when ϵ is fixed, then determines the value of μ for the equilibria. The black dashed line corresponds to the polytropic approximation $\beta(\mathcal{E}) = 5.77\mathcal{E}^{1/2}$, which is expected for King (1966) models with small values of Ψ (see Chavanis et al., 2015a, equation (86)). **Bottom:** Models with fixed values of $\{\Psi, \epsilon\}$, parametrised by μ, starting as $\mu = 0$ (black cross) at the upper right and increasing as the curve is traversed anti-clockwise. The red cross denotes the equilibrium with $\mu = \mu_c$, which corresponds to a first-order microcanonical phase transition. The insets offer a magnified view of this locus, scaled with Regime 3 asymptotics.

complex caloric curve. For large values of a_0, the equilibria display the "cold spiral" described above, with only a minor displacement of the relevant turning points. This is consistent with our previous remarks concerning the behaviour of the entropy for large values of a_0 (see Sect. 2.8.1). For small values of a_0, the behaviour of the models is drastically different with respect to the classic case: at high temperatures, a new branch appears in the caloric curve. This branch corresponds to the solutions in the proximity and beyond the sharp transition that occurs at the critical value $\mu = \mu_c(\Psi, \epsilon)$.

The caloric curve for equilibria with non-vanishing values of μ is multi-valued in $\mathcal{E}$, hence phase transitions can occur. Specifically, we identify the locus at which the two branches meet as a first-order microcanonical phase transition (i.e., where the values of the entropy of the two phases become equal, e.g., see Gross et al. 1996). This two-branch caloric curve resembles the one identified by Chavanis et al. 2015b (see especially Sect. IV, A and B) for the case of Fermionic King models in the limit of high, yet finite, values of the degeneracy parameter, where two phases of "gaseous" and "condensed" nature can co-exist. In their setting, they qualitatively note that to make the transition from the gaseous phase to the condensed phase, the system must spontaneously form a "small nucleus" and, vice versa, from the condensed phase to the gaseous phase, the system must spontaneously form a "massive atmosphere". This is akin to the sharp transition in truncation radius and mass of the host stellar system, which we initially noted in Fig. 2.2 and subsequently characterised in full with the three nested asymptotic regimes.

The insets in Fig. 2.18 show that thanks to the Regime 3 asymptotics in region 2, we can further characterise the behaviour of the caloric curve close to the phase transition. Under the appropriate rescaling conditions (see Sect. 2.6.2) and using equations (2.19), (2.57), (2.68), and (2.69), we find that $\beta = O(\epsilon^{4/3})$ and $\mathcal{E} = O(\epsilon^{8/3})$; this observation enables us to identify the ϵ-independent behaviour of the caloric curve at the phase transition.

2.9 Application of previous formalism to other non-King models

The formalism for the inclusion of a central black hole, as developed in Sect. 2.4-2.6, is not relevant exclusively to King (1966) models. Several families of truncated isothermal spheres (see, e.g. Davoust 1977, Gomez-Leyton & Velazquez 2014, Gieles & Zocchi 2015), and, more generally, spherical isotropic distribution functions (e.g., the kinetic counterparts to low-n polytropes, including the Plummer 1911 model; see App. B in Bertin & Varri 2008 details), are suitable for an immediate application of this approach. Here we summarise some intuitive conclusions pertinent to two notable cases. We consider the isotropic limit of the Prendergast & Tomer (1970b) (i.e. Woolley 1954) and Wilson (1975) distribution

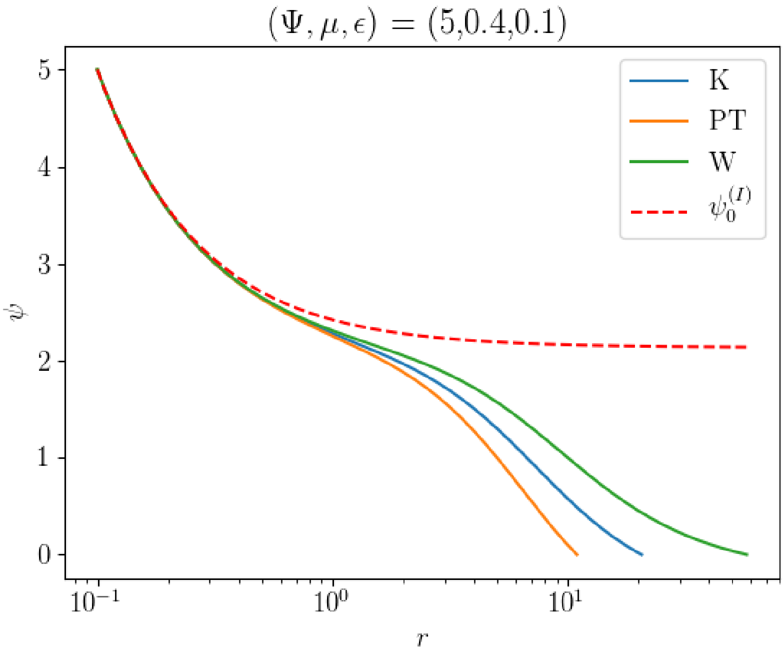

Figure 2.19: Numerical solutions to equation (2.16) using different phase space truncation prescriptions. The red dashed line shows the zeroth-order approximation to the central behaviour via equation (2.24) which is not dependent upon the truncation prescription. These parameters have been chosen to be away from the transition region in all three cases, effectively placing each of these models in the equivalent of Regime 1 described in Sect. 2.4.

functions, which are defined as

$$f_{PT}(E) = Ae^{-aE} \tag{2.73}$$

$$f_{WT}(E) = Ae^{-aE_0}\left[e^{-a(E-E_0)} - 1 + a(E-E_0)\right] \tag{2.74}$$

for $E \leq E_0$ and $f_{PT}(E) = f_{WT}(E) = 0$ otherwise; when integrated over the velocity space, these families provide densities with the same functional form as equation (2.3)

$$\rho_{PT}(\psi) = \frac{3}{2}\hat{A}e^{\psi}\gamma\left(\frac{3}{2}, \psi\right), \tag{2.75}$$

$$\rho_{W}(\psi) = \frac{2}{5}\hat{A}e^{\psi}\gamma\left(\frac{7}{2}, \psi\right), \tag{2.76}$$

which are then used directly in equation (2.16). The primary difference here is in the index of the lower incomplete gamma function: a higher value of this index delivers a smoother phase space truncation (e.g., see Hunter 1977; Davoust 1977, or App. A in Varri & Bertin 2012, of which we have adopted the same notation). The phase space truncation prescription, therefore, primarily affects the behaviour of the solution in the outer regions of the domain. In Fig. 2.19, we present the numerical solution of equation (2.16) for three models with different truncation prescriptions, but the same values of central dimensionless escape energy Ψ, minimal radius ϵ, and black hole mass μ (corresponding, in all cases, to an equilibrium within Regime 1). All truncation prescriptions produce a similar behaviour of the dimensionless escape energy near the centre of the system, where the black hole contribution is dominant; such a behaviour is captured by the asymptotic solution for Region I of Regime 1 (see Sect. 2.4).

The general results from our asymptotic analysis still hold for the construction of these additional equilibria. First, as illustrated in Fig. 2.19, in the outer regions of the domain, the solution behaves as a model without a central black hole, but with a lower central dimensionless escape energy given by the parameter a_0. Second, the fundamental structure of the parameter space is equivalent: a critical black hole mass $\mu_c = \mu_c(\Psi, \epsilon)$, at which the sharp transition in the properties of the models occurs, and a maximum value $\mu_{\max} = \mu_{\max}(\Psi, \epsilon)$, which results from the requirement of positivity of a_0, still exist. The expression of μ_c, which is derived using the Regime 3 asymptotics (see Sect. 2.6), is particularly sensitive to the value of the index of the lower incomplete gamma function, which, in turn, has a large influence upon the particular scaling in ϵ identified in various regimes considered in the main text. In essence, the steepness of the density profiles of the model of interest (as determined by the smoothness of the underlying distribution function), sets the number of nested asymptotic regimes required in the application of the formalism presented in this thesis.

2.10 Summary and discussion

In this chapter, we present a family of spherically symmetric, isotropic stellar equilibria with a central massive object. The models are defined by a truncated isothermal distribution function in phase space, suitably modified to allow for the presence of a central point mass. We propose a treatment of the boundary conditions of the relevant Poisson equation for the mean-field potential, which is then solved self-consistently and described using matched asymptotic expansions over three nested regimes of the dimensionless parameter space.

Our approach reveals the existence of a sharp transition in the structure of the solutions, corresponding to a transition between equilibria which are dominated by the mass of the host stellar system or by the mass of the central black hole. A thermodynamic characterisation of the models is offered through the corresponding caloric curve, which presents two distinct phases. Black hole-dominated equilibria populate a novel branch in the phase diagram, which connects, via a first-order microcanonical phase transition, to the classic “cold spiral” behaviour of the sequence of truncated isothermal spheres.

The formalism described in the main text can also be readily applied to other families of truncated isothermal spheres, and further classes of more complex non-spherical, anisotropic and rotating equilibria, with appropriate truncated isothermal behaviour in the central region of their domain. This investigation offers a route to explore the possible overlap between kinematic complexity and black holes in dense stellar environments, as motivated by recent observational evidence provided by nuclear and globular star clusters. Ultimately, this approach can address a number of limitations of current modelling techniques, and it paves the way towards a more informative assessment of the presence of intermediate-mass black holes in dense stellar systems.

More generally, these LoKi models provide a tool to approach the study of quasi-Keplerian systems, in which the mass of the central black hole and its host system are comparable, without resorting to approximate "tracer density" arguments. This, therefore, represents a fruitful playground for the study of the behaviour of the stars in the proximity of a central black hole, within a realistic self-consistent potential, with possible implications for few-body black hole dynamics. To facilitate the application to observational data and N-body simulations, we also provide a numerical implementation (LoKi - Loaded King Models, see App. B) which enables a rapid computation of the intrinsic and projected properties of the models and generates discrete samples in configuration and velocity space.

Chapter 3

Rotating Loaded King models

3.1 Introduction

In this chapter, we extend the class of LoKi models introduced in Chapt. 2 to the case of a rigidly rotating cluster with a central black hole. As in Varri & Bertin (2012), the addition of rotation is accomplished via assuming a distribution function of the form $f(H)$, where $H = E - \omega J_z$ is the Jacobi integral (e.g., see Landau & Lifshitz 1976). The presence of the black hole is then accounted for via a change of variables which may be shown to be equivalent to the modification of boundary conditions for the Poisson equation employed in Chapt. 2 for this purpose. In Sect. 3.3-3.4 we detail the numerical solution of these models. Initially, we use an iterative procedure based on that used by Prendergast & Tomer (1970a), which possesses the possibility of extension to the case of differential rotation (as in Varri & Bertin 2012 for example). The rigid body motion assumed here then allows us to consider a solution via matched asymptotic expansions. In Sect. 3.5 we investigate the admissible parameter space for these models with a focus on the maximum angular momentum content that a configuration can support. In Sect. 3.6 we present the intrinsic properties of these models. In Sect. 3.7 we perform a similar thermodynamic characterisation to that performed in Chapt. 2, for these rotating models. We then present our conclusions in Sect. 3.8.

3.2 Model construction

We consider a rotating, isotropic stellar system with a central black hole. This black hole is treated as a point particle with mass M_{BH} located at the system centre of mass. As in Chapt. 2 and Huntley & Saslaw (1975), we also make the modelling assumption that interior to some minimum radius, r_{min}, all the mass may be considered to be concentrated at the origin, i.e. that the stellar density, $\rho = 0$ for $r < r_{\mathrm{min}}$. We further assume that the system rigidly rotates about the $z-$axis with angular frequency ω. This assumption relaxes the condition of spherical symmetry considered in Chapt. 2, as this configuration is axisymmetric about the rotation axis. Consequently, we shall work in the co-rotating frame of reference and use a spherical coordinate system with (r, θ, ϕ) representing the radial, polar, and azimuthal variables respectively.

In this frame of reference, the energy of a single star is given by the Jacobi integral (see Landau & Lifshitz, 1976)

$$H = \frac{1}{2}v^2 + \Phi_{\mathrm{cen}}(r,\theta) + \Phi_C(r,\theta) + \Phi_{\mathrm{BH}}(r), \tag{3.1}$$

where Φ_C is the cluster potential to be determined self-consistently,

$$\Phi_{\mathrm{cen}}(r,\theta) = -\frac{1}{2}\omega^2 r^2 \sin^2\theta \tag{3.2}$$

is the centrifugal potential, and

$$\Phi_{\mathrm{BH}}(r) = -\frac{GM_{\mathrm{BH}}}{r} \tag{3.3}$$

is the contribution to the potential due to the black hole.

To encode the influence of the rigid rotation upon the system we then assume a distribution function that takes the same functional form as the King (1966) model, but which uses the Jacobi integral in place of the usual single star energy

$$f(H) = \begin{cases} Ae^{-aH_0}\left[e^{-a(H-H_0)} - 1\right], & H \le H_0, \\ 0, & H > H_0. \end{cases} \tag{3.4}$$

Here a and A provide physical scales on the energy and overall phase space normalisation. The constant H_0 then parameterises the truncation of the system imposed by external tidal effects. We now introduce the dimensionless escape energy defined via

$$\psi(r,\theta) = a\left[H_0 - \Phi_C(r,\theta) - \Phi_{\mathrm{cen}}(r,\theta) - \Phi_{\mathrm{BH}}(r)\right]. \tag{3.5}$$

This quantity is defined such that the outer boundary of the system is described by the surface $\psi\left(r_t(\theta),\theta\right) = 0$ for $\theta \in [0,\pi]$. This highlights the axisymmetric nature of the problem, as a single radius $r = r_t$ is no longer sufficient to describe the boundary of the system as in Chapt. 2.

The stellar density corresponding to the distribution function (3.4) is calculated as the zeroth moment of this distribution function in velocity space

$$\rho(\psi) = \begin{cases} \hat{A}e^{\psi}\gamma\left(\frac{5}{2},\psi\right) = \hat{A}\hat{\rho}(\psi), & \psi > 0 \\ 0, & \psi \le 0, \end{cases} \tag{3.6}$$

where $\hat{A} = 8\sqrt{2}\pi A\, e^{-aH_0}/(3a^{3/2})$, and γ is the lower incomplete gamma function (Olver et al., 2022).

A self-consistent equilibrium then requires that the stellar potential and density be determined via the Poisson equation

$$\nabla^2\Phi_C(r,\theta) = 4\pi G\rho(r,\theta). \tag{3.7}$$

We express equation (3.7) in fully dimensionless units by substituting in the dimensionless escape energy (3.5), and introducing the dimensionless radial variable $\hat{r} = r/r_K$ where

$$r_K = \left(\frac{9}{4\pi G\rho_0 a}\right)^{\frac{1}{2}} \tag{3.8}$$

is the classical King scale radius. Here ρ_0 is the density evaluated on the inner surface $r = r_{\mathrm{min}}$. In these variables, we may rewrite the Poisson equation (3.7) as

$$\nabla^2\psi = -9\frac{\rho}{\rho_0} + 18\chi, \tag{3.9}$$

where

$$\chi = \frac{\omega^2}{4\pi G\rho_0} \tag{3.10}$$

is a parameter measuring the strength of the rotation (Varri & Bertin, 2012). By construction, this parameter is small as it represents the ratio between the angular frequency of the rigid rotation for the whole cluster and a scale on the orbital frequencies in the centre of the system. This observation is important for the success of the asymptotic solution to equation (3.9) described in Sect. 3.4. The inner spherical surface is then defined by $\hat{r} = \varepsilon$.

We must now set boundary conditions for equation (3.9). We may naively think that setting boundary conditions on the inner surface, in an analogous manner to Chapt. 2, is the way to proceed. However, this choice neglects important information that is vital to the solution of the Poisson equation in this case.

Instead, we shall appeal to our assumption that the stellar density is zero interior to $\hat{r} = \varepsilon$. In this region, we have only the potential due to the central black hole. We may then subtract the part of solution to equation (3.9) that diverges as $\hat{r} \to 0$ and work with the variable

$$u(\hat{r},\theta) = \psi(\hat{r},\theta) - \frac{9\mu}{4\pi\hat{r}} - \frac{9}{2}\chi\hat{r}^2\sin^2\theta, \tag{3.11}$$

where $\mu = M_{\mathrm{BH}}/(\rho_0 r_K^3)$ is the non-dimensional black hole mass. Subtracting the centrifugal term here just simplifies the resulting Poisson equation and is not required to set boundary conditions and obtain a solution. In particular, just for Sect. 3.4 we will drop this term from the definition of u, as this is the choice of variable in which the resulting equations are most simply expressed there. As a result, the variable u now does not diverge at the origin. This regularity then allows us to set boundary conditions at the origin. We also have a condition governing the expected behaviour of the solution at larger radii. Namely, the cluster potential, Φ_C, should tend to zero at large radii. This is a consequence of the finite extent of the system imposed by the truncation in phase space.

The full boundary value problem governing the dimensionless escape energy is then given by

$$\nabla^2 u(\hat{r},\theta) = -\frac{9}{\hat{\rho}(\Psi)}\hat{\rho}\left(u(\hat{r},\theta) + \frac{9\mu}{4\pi\hat{r}} + \frac{9}{2}\chi\hat{r}^2\sin^2\theta\right), \tag{3.12a}$$

$$u(0,\theta) = \Psi - \frac{9\mu}{4\pi\varepsilon} = a_0, \tag{3.12b}$$

$$\partial_{\hat{r}} u(0,\theta) = 0, \tag{3.12c}$$

$$u(\hat{r},\theta) + a\Phi_{\text{cen}}(\hat{r},\theta) \to aH_0, \text{ as } \hat{r} \to \infty. \tag{3.12d}$$

Where we introduce the notation a_0 to be consistent with that employed in Chapt. 2 for the combination of parameters stated as the first boundary condition (3.12b). We must also recall the assumption that $\hat{\rho} = 0$ for $\hat{r} < \varepsilon$, so the $\hat{r}^{-1}$ term in equation (3.12a) does not diverge. For $\hat{r} \geq \varepsilon$ the density is given by equation (3.6).

The specific boundary conditions chosen are such that the solution to equation (3.12a) reduces to that of the models considered in Chapt. 2 when $\chi = 0$. Consequently, when we further set $\mu = \epsilon = 0$ we also recover the King (1966) models. This choice also imposes a maximum value on the mass of the black hole, μ, so that $a_0 = \Psi - 9\mu/(4\pi\epsilon) > 0$ to ensure that the dimensionless escape energy is well posed, see Sect. 2.4 for further discussion of this combination of parameters.

In summary, our model is defined by two physical scales (A, and a), and four dimensionless parameters: the dimensionless radius, ε, below which the potential is considered to be dominated by the black hole, the dimensionless escape energy Ψ at this radius, the dimensionless black hole mass, μ, and the rotation strength parameter, χ. For simplicity of notation, we will drop hats from non-dimensional variables in the remaining sections of this chapter, unless otherwise stated.

We now present two methods of solution for the boundary value problem (3.12). First, in Sect. 3.3 we describe an iteration scheme to obtain a numerical solution. Alternatively, in Sect. 3.4 we detail the use of matched asymptotic expansions, the results of which are compared with the iterative solution to verify accuracy. The asymptotic solution is significantly more efficient to calculate and will allow us to further explore the properties of these models analytically.

3.3 Spectral iteration solution

To obtain a numerical solution to equation (3.12) we define a spectral iteration scheme equivalent to the approach used by Prendergast & Tomer (1970a) and Varri & Bertin (2012) to investigate models of rotating elliptical galaxies, and globular clusters (with no central black hole).

We define an iteration scheme $u^{(n)}$ where the seed solution $u^{(0)}$ is given by

$$\nabla^2 u^{(0)}(r) = -\frac{9}{\rho(\Psi)}\rho\left(u^{(0)}(r) + \frac{9\mu}{4\pi r}\right), \tag{3.13a}$$

$$u^{(0)}(0) = \Psi - \frac{9\mu}{4\pi\varepsilon}, \tag{3.13b}$$

$$\partial_r u^{(0)}(0) = 0. \tag{3.13c}$$

The seed solution corresponds to the non-rotating, and thus spherically symmetric, LoKi models introduced and explored in detail within Chapt. 2.

Subsequent solutions $u^{(n)}$ are obtained by solving the Poisson equation, sourced by the $(n-1)$-th solution $u^{(n-1)}$,

$$\nabla^2 u^{(n)} = -9\frac{\rho\left(u^{(n-1)} + \frac{9\mu}{4\pi r} + \frac{9}{2}\chi r^2 \sin^2\theta\right)}{\rho(\Psi)}, \tag{3.14a}$$

$$u^{(n)}(0,\theta) = \Psi - \frac{9\mu}{4\pi\varepsilon}, \tag{3.14b}$$

$$\partial_r u^{(n)}(0,\theta) = 0, \tag{3.14c}$$

$$u^{(n)} + a\Phi_{\mathrm{cen}}(r,\theta) \to aH_0, \text{ as } r \to \infty. \tag{3.14d}$$

We may then expand the density and escape energy in Legendre series

$$u^{(n)}(r,\theta) = \sum_{l=0}^{\infty} u_l^{(n)}(r)\mathrm{P}_l(\cos\theta), \tag{3.15}$$

$$\rho^{(n)}(r,\theta) = \sum_{l=0}^{\infty} \rho_l^{(n)}(r)\mathrm{P}_l(\cos\theta), \tag{3.16}$$

where P_l is the lth Legendre polynomial (Olver et al., 2022, 18.3). Substituting these expansions into equation (3.14a) provides a set of l linear initial value problems, in the radial variable only, provided by

$$\left(\frac{\mathrm{d}^2}{\mathrm{d}r^2} + \frac{2}{r}\frac{\mathrm{d}}{\mathrm{d}r} - \frac{l(l+1)}{r^2}\right) u_l^{(n)}(r) = -9\frac{\rho_l^{(n-1)}(r)}{\rho(\Psi)} \tag{3.17}$$

and boundary conditions

$$u_0^{(n)}(0) = \Psi - \frac{9\mu}{4\pi\varepsilon}, \quad u_l^{(n)}(0) = 0 \text{ for } l > 0, \tag{3.18}$$

$$u_0^{(n)\prime}(0) = 0, \quad u_l^{(n)\prime}(0) = 0 \text{ for } l > 0, \tag{3.19}$$

$$u_0^{(n)} \to aH_0, \quad u_l^{(n)} \to 0 \text{ as } r \to 0 \text{ for } l > 0. \tag{3.20}$$

Each of these problems is linear and amenable to the method of variation of arbitrary constants (see App. C). This allows us to express the solution, in integral form, at each iteration by

$$u_0^{(n)}(r) = \Psi - \frac{9\mu}{4\pi\varepsilon} - \frac{9}{\rho(\Psi)}\left[\int_\varepsilon^r s\rho_0^{(n-1)}(s)\mathrm{d}s - \frac{1}{r}\int_\varepsilon^r s^2\rho_0^{(n-1)}(s)\mathrm{d}s\right], \tag{3.21}$$

and

$$u_l^{(n)}(r) = \frac{9}{(2l+1)\rho(\Psi)}\left[r^l\int_r^\infty s^{1-l}\rho_l^{(n-1)}(s)\mathrm{d}s + \frac{1}{r^{l+1}}\int_\varepsilon^r s^{l+2}\rho_0^{(n-1)}(s)\mathrm{d}s\right]. \tag{3.22}$$

The integrals contained within equations (3.21) and (3.22) are then evaluated numerically. The iteration process is continued until the sequence of solutions $u^{(n)}$ converges numerically. The details of the specific implementation used in this paper are presented in App. C.

3.4 Asymptotic solution

The solution of initial value problems such as (3.12a)-(3.12d) via asymptotic methods has a distinguished history in theoretical astrophysics. Initially, work was done constructing polytropic models of rotating stars using asymptotic methods: the Chandrasekhar-Milne expansion (see Milne 1923, Chandrasekhar 1933, and Tassoul 1978). First, we introduce the solution on the interior of system, $u^{(\mathrm{int})}$, where the stellar density is non-vanishing, and the solution on the exterior of the system, $u^{(\mathrm{ext})}$, where the stellar density is zero and equation (3.12a) reduces to the Laplace equation. These functions are expressed as an expansion in the rotation strength parameter, χ,

$$u^{(\mathrm{int})}(r,\theta) = \sum_{k=0}^{\infty}\frac{1}{k!}u_k^{(\mathrm{int})}(r,\theta)\chi^k, \tag{3.23}$$

$$u^{(\mathrm{ext})}(r,\theta) = \sum_{k=0}^{\infty}\frac{1}{k!}u_k^{(\mathrm{ext})}(r,\theta)\chi^k. \tag{3.24}$$

In the Chandrasekhar-Milne expansion, the potential and its derivative are enforced to be continuous over a given surface. However, Monaghan & Roxburgh (1965) pointed out that the resulting boundary value problem (3.12a)-(3.12d) is formally singular, as the series expansions stated above become disordered. As we approach the boundary between the interior and exterior regions, the leading and first-order terms in the expansion of the potential become of comparable size, and the expansion is no longer valid. It was not until the contribution of Smith (1975) that a satisfactory method of solution was found for the rigidly rotating polytrope involving the use of matched asymptotic expansions. Success has then been found in applying those techniques in non-polytropic cases (Varri

& Bertin 2012), as well as for alternative quadratic perturbations such as the influence of an external tidal field (Bertin & Varri 2008). We thus apply the same technique of matched asymptotic expansions to our problem.

3.4.1 Interior solution

Substituting equation (3.23) into equation (3.12) provides a series of initial value problems at each order of k.

At leading-order we obtain

$$\nabla^2 u_0^{(\mathrm{int})}(r) = -9\frac{9}{\rho(\Psi)}\rho\left(u_0^{(\mathrm{int})}(r) + \frac{9\mu}{4\pi r}\right), \tag{3.25a}$$

$$u_0^{(\mathrm{int})}(0) = \Psi - \frac{9\mu}{4\pi\varepsilon}, \tag{3.25b}$$

$$u_0^{(\mathrm{int})\prime}(0) = 0, \tag{3.25c}$$

which, again, delivers the LoKi models considered in Chapt. 2. We recall that the boundary of the LoKi model occurs at a radius $r = r_t$ defined by

$$\psi_0^{(\mathrm{int})}(r_t) = u_0^{(\mathrm{int})}(r_t) + \frac{9\mu}{4\pi r_t} = 0.$$

We limit ourselves to considering only the first-order corrections in χ to the LoKi model, given by

$$[\nabla^2 + R_1(r,\Psi)]u_1^{(\mathrm{int})}(r,\theta) = 18, \tag{3.26a}$$

$$u_1^{(\mathrm{int})}(0) = 0, \tag{3.26b}$$

$$\nabla u_1^{(\mathrm{int})}(0) = 0, \tag{3.26c}$$

where

$$R_1(r,\Psi) = \frac{9}{\rho(\Psi)}\left.\frac{\mathrm{d}\rho}{\mathrm{d}\psi}\right|_{\psi_0^{(\mathrm{int})}} \tag{3.27}$$

is a term arising due to the expansion of the density term in equation (3.12a) for small χ. Now, in a similar manner to the iteration scheme, we may reduce the partial differential equation in equation (3.26a) to a series of initial value problems in the radial variable only, by expanding $u_1^{(\mathrm{int})}$ in a Legendre series

$$u_1^{(\mathrm{int})}(r,\theta) = \sum_{l=0}^{\infty} u_{1,l}(r)\mathrm{P}_l(\cos\theta). \tag{3.28}$$

If we substitute equation (3.28) into equation (3.26a) and introduce the operator

$$\mathcal{D}_l = \frac{\mathrm{d}^2}{\mathrm{d}r^2} + \frac{2}{r}\frac{\mathrm{d}}{\mathrm{d}r} - \frac{l(l+1)}{r^2} + R_1(r,\Psi), \tag{3.29}$$

then the problem obtained at $l = 0$ is given by

$$\mathcal{D}_0 u_{1,0}(r) = 18, \tag{3.30a}$$
$$u_{1,0}(0) = 0, \tag{3.30b}$$
$$u'_{1,0}(0) = 0. \tag{3.30c}$$

The two homogeneous solutions associated with the operator $\mathcal{D}_l$ take the form r^l and $1/r^{l+1}$ as $r \to 0$. In the $l = 0$ case, the contribution from the second homogeneous solution is zero, as we require regularity at the origin, eliminating the singular solution. The boundary condition (3.30b) further eliminates the constant solution. We are thus left with the particular solution corresponding to equation (3.30), to be obtained numerically.

For $l > 0$ we obtain

$$\mathcal{D}_l u_{1,l}(r) = 0, \tag{3.31a}$$
$$u_{1,l}(0) = 0, \tag{3.31b}$$
$$u'_{1,l}(0) = 0. \tag{3.31c}$$

In this case, the solution to equation (3.31) is given by $u_{1,l}(r) = A_l \gamma_l(r)$ where A_l are free constants, and γ_l are the homogeneous solutions to equation (3.31a), which behave as r^l as $r \to 0$.

Note that the regularity at the origin of the escape energy has allowed us to discard the divergent terms in the homogeneous solutions to equations (3.30) and (3.31). This would not have been possible if we naively set our initial boundary conditions on the surface $r = \epsilon$, as in Chapt. 2. If we did so then further free constants associated with divergent components of the homogeneous solutions at the origin remain, and cannot be determined in the asymptotic matching procedure.

The full interior solution is, therefore, given by

$$\begin{aligned}\psi^{(\text{int})}(r,\theta) &= \psi_0^{(\text{int})}(r) + \chi\left[u_{1,0}(r) + \sum_{l=1}^{\infty} A_l \gamma_l(r) P_l(\cos(\theta))\right], \\ &= u_0^{(\text{int})}(r) + \frac{9\mu}{4\pi r} + \chi\left[u_{1,0}(r) + \sum_{l=1}^{\infty} A_l \gamma_l(r) P_l(\cos(\theta)\right] + O(\chi^2),\end{aligned} \tag{3.32}$$

where the currently undetermined constants A_l must be specified via the matching procedure with the exterior solution. The matching process will require, formally, corrections up to third-order in χ to be taken into account. However, these corrections do not appear explicitly in the final definitions of the free constants needed in the first-order solution we are interested in. Hence, these corrections are not treated in detail here.

3.4.2 Exterior solution

Outside the surface where the density vanishes, which is currently unknown, the equation governing the exterior escape energy, $\psi^{(\mathrm{ext})}$, reduces to

$$\nabla^2\psi^{(\mathrm{ext})} = 18, \tag{3.33}$$

along with the condition

$$\psi^{(\mathrm{ext})}(r,\theta) - \frac{9}{2}\chi r^2 \sin^2\theta \to aH_0, \text{ as } r \to \infty, \tag{3.34}$$

arising from equation (3.12d). The solution to equations (3.33)-(3.34) then takes the form

$$\psi^{(\mathrm{ext})}(r,\theta) = \alpha - \frac{\lambda}{r} - \sum_{l=1}^{\infty} \frac{\beta_l}{r^{l+1}} \mathrm{P}_l(\cos\theta) + \frac{9}{2}\chi r^2 \sin^2(\theta), \tag{3.35}$$

where the first three terms correspond to the homogeneous solution of equation (3.33) satisfying boundary conditions (3.34), which eliminates the divergent solution. The last term then corresponds to the particular solution. The constants α, λ, β_l are all free constants that must be determined via matching with the interior solution. Therefore, we must be able to expand equation (3.35) as a series in χ. To accomplish this, we expand

$$\alpha = \alpha_0 + \alpha_1\chi + \alpha_2\chi^2 + O(\chi^3), \tag{3.36}$$

and we proceed similarly for λ. The expansion for each β_l must begin at first-order in χ, as for $\chi = 0$ we must recover the spherical solution given only by $\alpha - \lambda/r$. Hence, we expand each β_l as

$$\beta_l = a_l\chi + \frac{1}{2}b_l\chi^2 + O(\chi^3). \tag{3.37}$$

We only consider the expansion up to second-order as this will be sufficient to match the interior solution to the first-order. We may also expand the particular solution as a Legendre series

$$\begin{aligned}\frac{9}{2}r^2\sin^2(\theta) &= 3r^2\mathrm{P}_0(\cos\theta) - 3r^2\mathrm{P}_2(\cos\theta),\\ &= C_0(r)\mathrm{P}_0(\cos\theta) + C_2(r)\mathrm{P}_2(\cos\theta).\end{aligned} \tag{3.38}$$

Substituting these expansions into equation (3.35) provides the exterior solution to first-order in χ as

$$\psi^{(\mathrm{ext})}(r,\theta) = \alpha_0 - \frac{\lambda_0}{r} + \chi \Bigg[\alpha_1 - \frac{\lambda_1}{r} + C_0(r) - \sum_{l=1}^{\infty} \left(\frac{a_l}{r^{l+1}} - C_l(r)\right) \mathrm{P}_l(\cos\theta)\Bigg] + O(\chi^2). \tag{3.39}$$

As discussed in the previous section concerning the interior solution, formally we would also require the exterior solution up to third order to perform the matching procedure. Since the final expressions for obtaining the first-order matched solution do not depend on the higher-order corrections, we do not treat them in any further detail.

3.4.3 Boundary layer

The interior and exterior solutions present several free constants that must be determined via an asymptotic matching procedure. We recall that the validity of the expansion (3.32) breaks down in the vicinity of the point where the leading-order term $\psi_0^{(\mathrm{int})}$ vanishes. This condition takes place at the radius $r = r_t$. We address this formal singularity by introducing a boundary layer defined by rescaling the radial variable and the solution as

$$\eta = \frac{r_t - r}{\chi}, \tag{3.40}$$

$$\tau(r,\theta) = \frac{\psi^{(\mathrm{lay})}(r,\theta)}{\chi}, \tag{3.41}$$

where $\psi^{(\mathrm{lay})}$ represents the dimensionless escape energy within the boundary layer. Substituting equations (3.40) and (3.41) into equation (3.12a) provides that

$$\frac{\partial^2 \tau}{\partial \eta^2} - \frac{2\chi}{r_t - \chi\eta}\frac{\partial \tau}{\partial \eta} + \frac{\chi^2}{(r_t - \chi\eta)^2}\Lambda^2 \tau = -9\chi\frac{\rho(\chi\tau)}{\rho(\Psi)} + 18\chi^2, \tag{3.42}$$

where Λ^2 is the angular part of the Laplacian.

We expand τ as a series in χ,

$$\tau(r,\theta) = \sum_{k=0}^{\infty} \tau_k(r,\theta)\chi^k. \tag{3.43}$$

It is worth noting that, for a small argument, in equation (3.42) we have $\rho(z) \approx (2/5)z^{5/2}$ (Olver et al. 2022). Consequently, the density will only contribute at order 7/2 in χ or higher. Substituting equation (3.43) into equation (3.42) provides a sequence of initial value problems at each order in χ. We only consider terms up to first-order as this is sufficient to match the free constants in equation (3.32) up to first-order.

At leading-order, we have

$$\frac{\partial^2 \tau}{\partial \eta^2} = 0, \tag{3.44}$$

from which we easily obtain

$$\tau_0(r,\theta) = F_0(\theta)\eta + G_0(\theta) \tag{3.45}$$

where F_0, G_0 are free angular functions. At first-order, we have that

$$\frac{\partial^2 \tau_1}{\partial \eta^2} - \frac{2}{r_t}\frac{\partial \tau_0}{\partial \eta} = 0. \tag{3.46}$$

Using equation (3.45) in equation (3.46) then provides that

$$\tau_1(r,\theta) = \frac{F_0(\theta)}{r_t}\eta^2 + F_1(\theta)\eta + G_1(\theta), \tag{3.47}$$

where again F_1, G_1 are free angular functions.

The second-order solution within the boundary layer, τ_2, may be calculated similarly and it is formally required for the matching procedure. However, since there is no explicit dependence on second-order terms in the free constants needed in the first-order solution, we will omit any further discussion of the τ_2 contributions.

3.4.4 Asymptotic matching to first-order

Now that we have formulated the relevant expansions in each region, we are in a position to specify the remaining free constants via a matching procedure based on Van Dyke's matching principle (Van Dyke 1975). Specifically, to achieve a global solution, we match the interior solution to the solution on the boundary layer, and then the boundary layer solution to the exterior solution. For the full details of this process see App. D. The results of this procedure that are relevant to the first-order solution are shown below.

$$\psi_0^{(\mathrm{int})}(r_t) = 0 \qquad = \psi_0^{(\mathrm{ext})}(r_t), \tag{3.48a}$$

$$-\psi_0^{(\mathrm{int})\prime}(r_t) = F_0(\theta) \ = \psi_0^{(\mathrm{ext})\prime}(r_t), \tag{3.48b}$$

$$\psi_1^{(\mathrm{int})}(r_t,\theta) = G_0(\theta) = \psi_1^{(\mathrm{ext})}(r_t,\theta), \tag{3.48c}$$

$$-\partial_r\psi_1^{(\mathrm{int})}(r_t,\theta) = F_1(\theta) \ = -\partial_r\psi_1^{(\mathrm{ext})}(r_t,\theta). \tag{3.48d}$$

These relations may then be used along with equations (3.32) and (3.39) to deduce the remaining free constants which are given as

$$\lambda_0 = r_t^2 \psi_0^{(\text{int})\prime}(r_t), \tag{3.49a}$$

$$\alpha_0 = r_t \psi_0^{(\text{int})\prime}(r_t), \tag{3.49b}$$

$$\lambda_1 = u_{1,0}'(r_t) r_t^2 - C_0'(r_t) r_t^2, \tag{3.49c}$$

$$\alpha_1 = u_{1,0}(r_t) + \frac{\lambda_1}{r_t} - C_0(r_t), \tag{3.49d}$$

$$A_2 = \frac{5C_2(r_t)}{r_t \gamma_2'(r_t) + 3\gamma_2(r_t)}, \tag{3.49e}$$

$$a_2 = -r_t^3 [A_2 \gamma_2(r_t) - C_2(r_t)], \tag{3.49f}$$

with $A_l = a_l = 0$ for $l \neq 2$. This set of conditions specifies all free constants necessary to obtain the full interior and exterior solutions up to first-order in χ. The interior solution may be written as

$$\psi^{(\text{int})}(r) = \psi_0^{(\text{int})}(r) + \chi \left[u_{1,0}(r) + A_2 \gamma_2(r) \mathrm{P}_2(\cos\theta) \right] + O(\chi^2), \tag{3.50}$$

and the exterior solution is given by equation (3.39). In essence, the entire solution process requires solving three initial value problems for $\psi_0^{(\text{int})}$, $u_{1,0}$, and γ_2, which is significantly more efficient than the iterative method described in Sect. 3.3.

In Fig. 3.1 we illustrate the dimensionless escape energy evaluated along the polar axis ($\theta = 0$), where the influence of the rotation is absent (as the perturbation is a quadratic function only of the x and y variables), and along the equatorial plane ($\theta = \pi/2$), where the influence of rotation is most significant. The figure displays the solution obtained by using both the iteration scheme and asymptotic methods for the same set of parameters. We note the good agreement between the profiles calculated using distinct methods. For efficiency, the results we present in the rest of this chapter will be calculated using the asymptotic method.

3.5 The parameter space

The models described thus far are governed by four dimensionless parameters. For a full discussion of the role of the central concentration, Ψ, the black hole mass, μ, and the minimum radius, ϵ, we refer to Chapt. 2, as this subset of parameters already appears in the LoKi models introduced previously. Here, we note that the existence of a maximum possible black hole mass, μ_{max} for a given choice of $\{\Psi, \epsilon\}$, also applies to the rotating models considered in this chapter. This feature arises from the condition $\Psi - 9\mu/(4\pi\epsilon) > 0$, i.e. the total depth of the potential well can not be shallower than the depth due solely to the central black hole. We recall that, for a given choice of $\{\Psi, \epsilon\}$, there also exists a critical value of the black hole mass, μ_c, at which the extent of the system is greatest (see

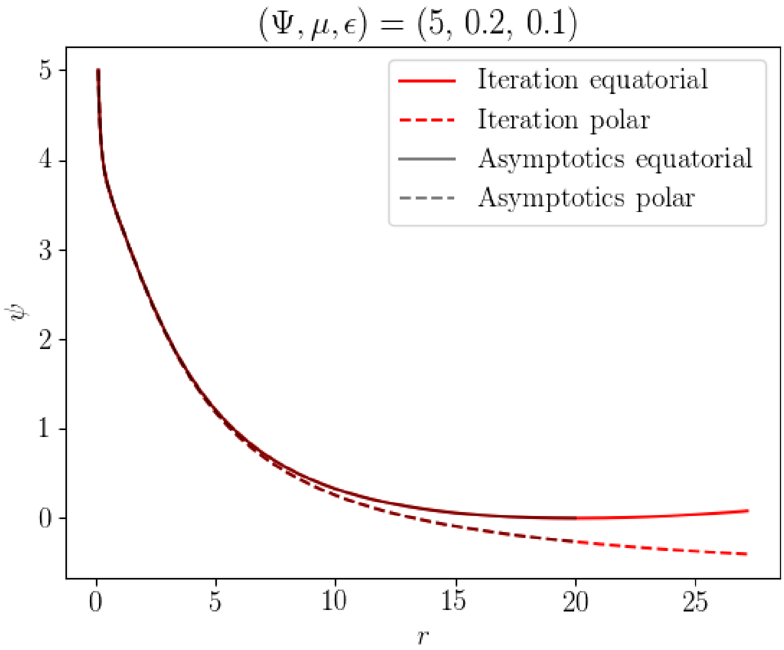

Figure 3.1: Comparison of the numerical solutions to equation (3.12) for a selected critical (in terms of the rotation strength parameter χ) model, obtained via the spectral iterative scheme (red) and via matched asymptotic expansions (black). The solid line represents the solution in the equatorial plane ($\theta = \pi/2$), while the dashed line shows the solution in the polar direction ($\theta = 0$).

Fig. 2.2). A model with a black hole mass close to this critical value displays a very compact and dense central region, surrounded by a highly extended and diffuse outer region.

The behaviour of the non-rotating configurations considered here is further enriched by the presence of the non-vanishing global angular momentum, which is encapsulated by the rotation strength parameter χ. We illustrate in Fig. 3.2 the effect of increasing values of χ when the solution is evaluated on the equatorial plane ($\theta = \pi/2$). We can see that the system becomes more extended along this plane and the gradient at the edge of the solution becomes shallower. If we increase the rotation strength past a maximum rotation value, then the minimum in the escape energy will occur at $\psi > 0$. Therefore, the equipotential surface $\psi = 0$ which defines the boundary of the equilibrium is no longer closed, and the model becomes unphysical. Therefore, there exists also a maximum value of the rotation strength parameter, χ_c. A system rotating with this strength can thus be considered a critical model. On the boundary of such a critical equilibrium configuration, all points on the equatorial plane are saddle points. The distance of these points from the origin can be interpreted as the break-up radius of the rotating system, r_B.

In order to obtain values for χ_c and r_B, we must solve the following system of equations numerically

$$\psi(r = r_B, \theta = \pi/2|\chi_c) = 0, \tag{3.51a}$$

$$\partial_r\psi(r = r_B, \theta = \pi/2|\chi_c) = 0. \tag{3.51b}$$

The first condition corresponds to the requirement that r_B must be located on the equatorial plane of the boundary of a critically rotating equilibrium. The second condition enforces that the point $(r_B, \theta = \pi/2)$ is a critical point (in this case a saddle).

The interaction between χ_c and the other parameters is non-trivial. We illustrate in Fig. 3.3 and 3.4 the variation of the critical values of the rotation strength parameter χ_c, as a result of varying the black hole mass (with fixed Ψ and ϵ), and as a result of varying a_0 (with fixed μ, and ϵ). From Fig. 3.3 we see that there is a dramatic fall in the value of χ_c for large black hole masses. In particular, this drop occurs in the vicinity of the critical value of μ identified in Chapt. 2. This feature is driven primarily by the behaviour of the underlying LoKi model in this region of the parameter space. To prove this statement, we consider a reduced form of the exterior solution

$$\psi(r, \pi/2) = \psi_0^{(\mathrm{ext})}(r) - \frac{9}{2}\chi r^2, \tag{3.52}$$

where we take into account only the unperturbed exterior solution and the quadratic perturbation due to rotation, i.e. we neglect the first-order corrections to the dimensionless escape energy of the clusters. After substituting equation (3.52), the conditions (3.51) become algebraic equations that can be solved analytically, yielding a zeroth order approximation for χ_c as

$$\chi_c^{(0)} = -\frac{8\alpha_0^3}{243\lambda_0^2}, \tag{3.53}$$

where we recall that α_0 and λ_0 are the constants given by equations (3.49b) and (3.49a). We also note that in Sect. 2.6 we derived that the scalings for the magnitude of both r_t and $\psi_0^{(\text{int})}$ are $O(\epsilon^{-3})$ and $O(\epsilon^4)$, respectively. This then allows us to obtain the magnitudes of α_0 and λ_0 in the vicinity of the minimum χ_c, as seen in Fig. 3.3. The result of this assessment is that, in this region of the parameter space, the value of χ_c is of $O(\epsilon^{10})$, thus predicting the observed decrease in χ_c at black hole masses near that of the critical black hole mass identified in the LoKi models. It should be noted that this conclusion relies on the validity of the asymptotic results of Chapt. 2. If ϵ is not sufficiently small, then these asymptotic results no longer provide an appropriate description of the solution and this scaling no longer applies. This is illustrated in Fig. 3.3 where, for $\Psi = 3$, the value $\epsilon = 0.1$ is not sufficiently small. This causes the $\chi_c - \mu$ curve to be displaced compared to the predictions of this asymptotic theory. Although the exact scaling of χ_c no longer applies in this instance, the physical reasoning behind the still observed drop is still applicable. The physical reason for this decrease becomes apparent when considering the morphology of the LoKi models in this regime. These equilibria consist of a concentrated central region and an extremely extended, but diffuse, outer region. As the rotational perturbation is quadratic in radius, the outer portions can only sustain a very tenuous rigid body rotation, before the self-gravity of the system becomes subdominant to the centrifugal effects, leading to an open equipotential surface as the boundary of the configuration. This result is further supported by in Fig. 3.5 where the regions of low χ_c correspond to the regions of large break-off radius r_B over all three examined values of Ψ.

The results from this simple analysis are unchanged when considering the full self-consistent first-order solution given by equation (3.39). By substituting this expansion into equation (3.51) and using the Regime 3 asymptotic results from Chapt. 2 we may employ a dominant balance argument to recover that $\chi_c = O(\epsilon^{10})$ in this regime. Consequently, we conclude that the behaviour of χ_c as a function of the other parameters is primarily driven by the underlying LoKi model.

3.6 Intrinsic properties

To illustrate some basic properties of the models, in Fig. 3.6 we show the density contours in the meridional plane for a selection of critically rotating first-order models. By construction, these isodensity surfaces correspond to equipotential surfaces and isobaric surfaces, as all velocity moments of the distribution function are stratified on the dimensionless escape energy ψ (see equations (3.6) and (3.4)). First, as an extension to our conclusion from Sect. 3.5, we note that the behaviour of the rotating model is dominated by that of the LoKi model defined

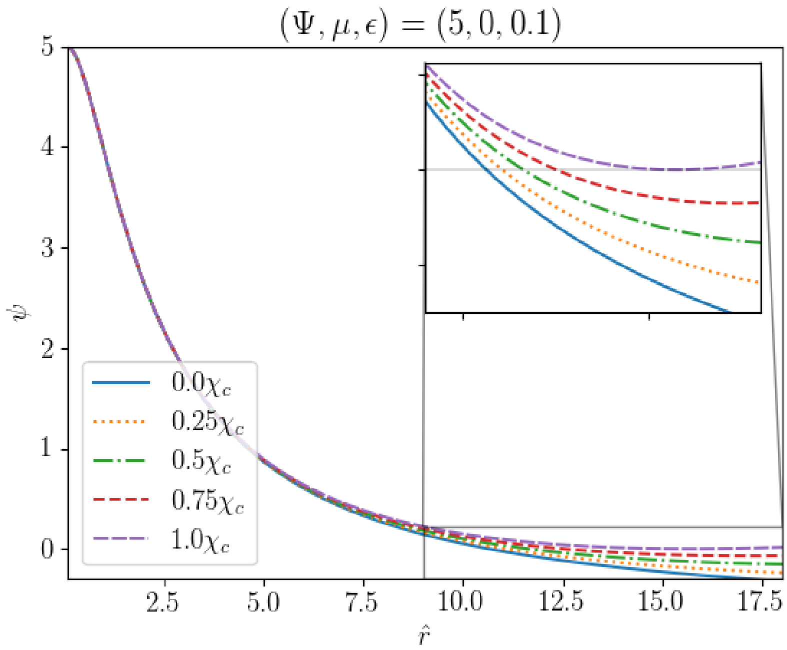

Figure 3.2: Dimensionless escape energy as a function of the dimensionless radius on the equatorial plane ($\theta = \pi/2$). A range of values for the rotation strength parameter are considered, from the non-rotating limit (solid blue) to the critical model (purple long dashes), while keeping the other three parameters fixed.

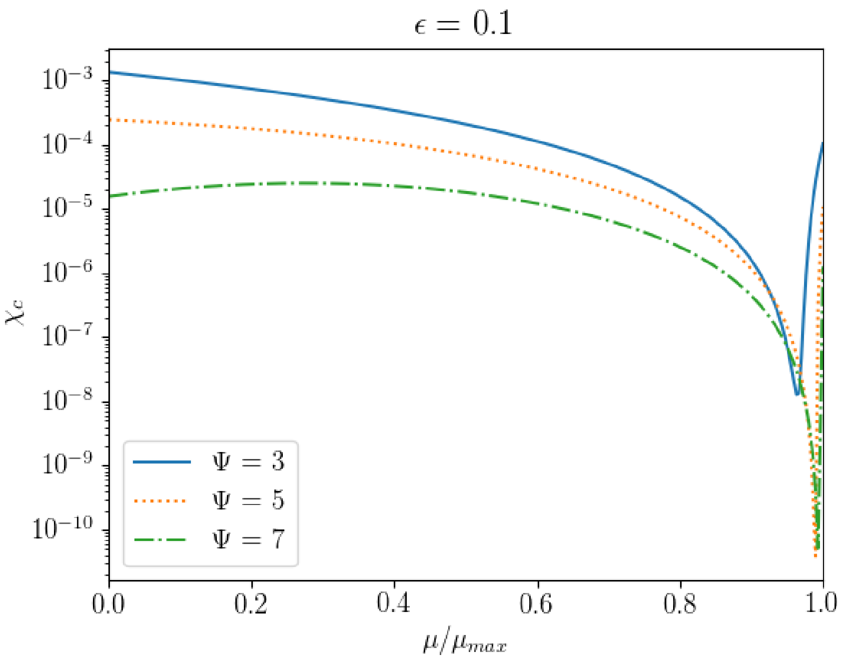

Figure 3.3: Critical rotation strength, χ_c, as a function of black hole mass, μ, for three selected central concentrations, Ψ. Obtained by numerically solving the system of equations (3.51), with the dimensionless escape energy ψ being provided by the first-order solution (3.50).

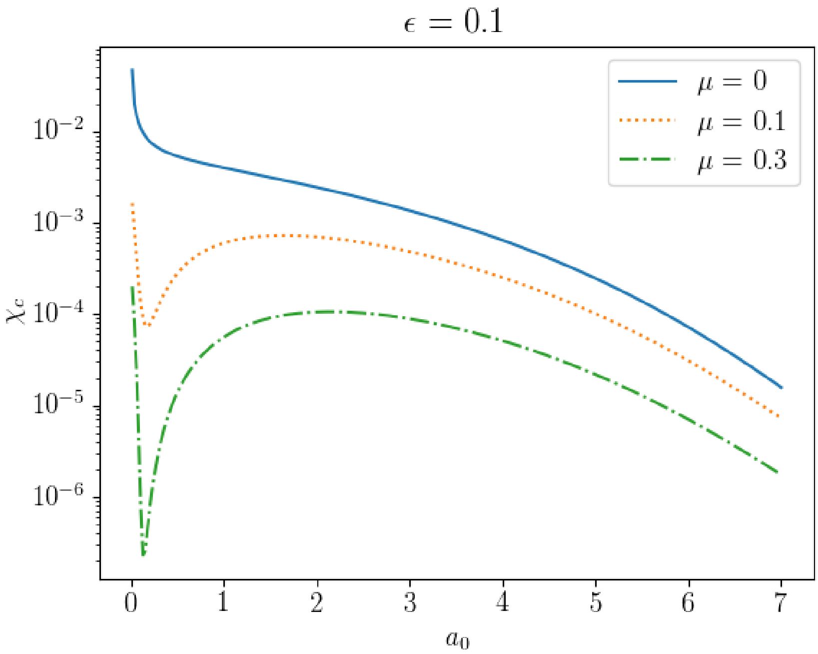

Figure 3.4: Critical rotation strength, χ_c, as a function of the particular combination of parameters $a_0 = \Psi - 9\mu/(4\pi\epsilon)$, for three selected black hole masses, μ. Again obtained by numerically solving equation (3.51) with ψ given by equation (3.50).

by equation (3.13). We can see that increasing Ψ provides a more centrally concentrated model. A moderately sized black hole (see the middle column) yields significant central density gradients. Models with black hole masses close to μ_c provide an extremely dense inner region, with a diffuse and extended outer envelope.

These models exhibit symmetry about the z-axis, as well as about the equatorial plane. Recall that the LoKi models are spherically symmetric. Once the rotational perturbation is added, we can see from Fig. 3.6 that a moderate flattening is visible, especially in the outer regions of the system. This flattening is best seen by inspecting the eccentricity, defined by

$$e = \sqrt{1 - \frac{b^2}{a^2}}, \tag{3.54}$$

where a and b are the semi-major/minor axes of the isodensity surfaces shown in Fig. 3.6. In Fig. 3.8 we show the eccentricity profiles for the three models illustrated in the bottom row of Fig. 3.6. As calculated in Varri & Bertin (2012), the non-black hole case ($\mu = 0$) exhibits a non-zero, though small, value of the eccentricity in the central region. The addition of the black hole further suppresses the deviation from spherical symmetry in the central region, an effect that increases with the black hole mass (a similar effect to that observed by Goodman & Binney (1984)). We can also see that the mass of the central black hole has no effect on the eccentricity in the outer regions of the system. The

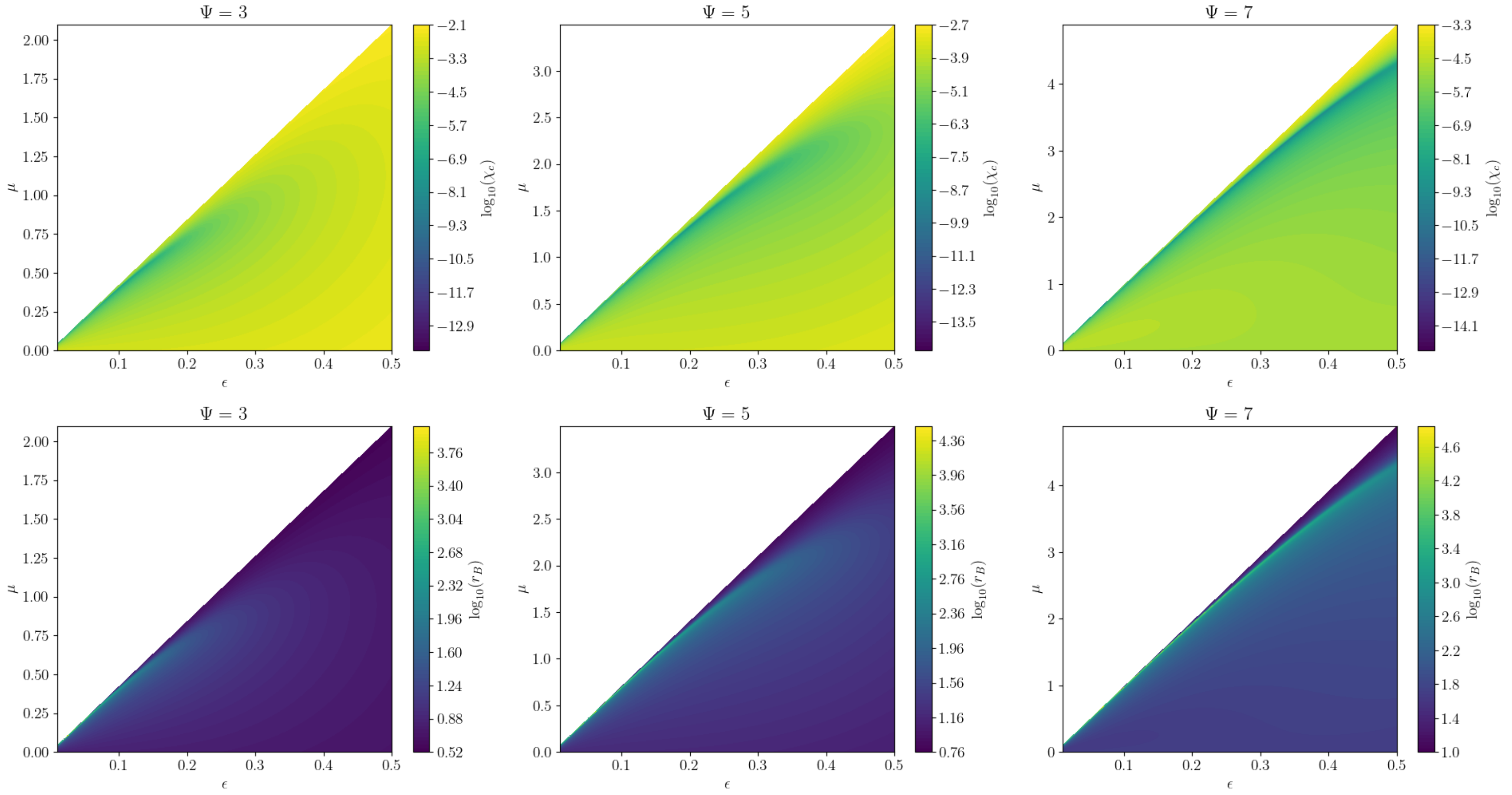

Figure 3.5: Contour plots of the critical rotation strength (top), and break-off radius (bottom) obtained via numerically solving the system of equations (3.51).

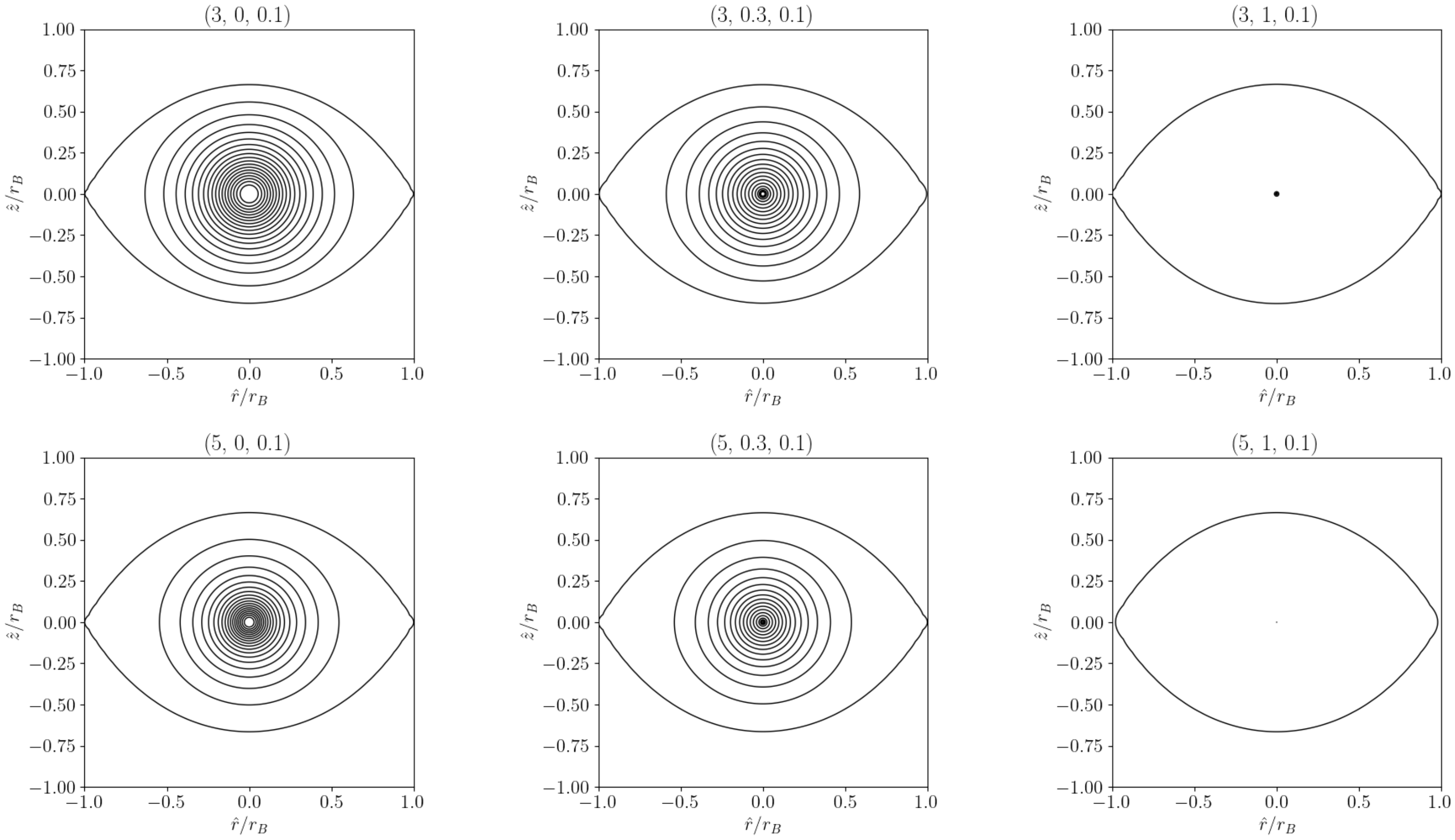

Figure 3.6: Density contours in the meridional plane for selected critically rotating models with varying values of $\{\Psi, \mu/\mu_c, \epsilon\}$. We present a set of models with low central concentration (top row), and moderate central concentration (bottom row). The black hole mass is given as a fraction of the critical black hole mass identified in Chapt. 2 and increases left to right. In each panel, 20 contours linearly spaced between zero and Ψ have been used.

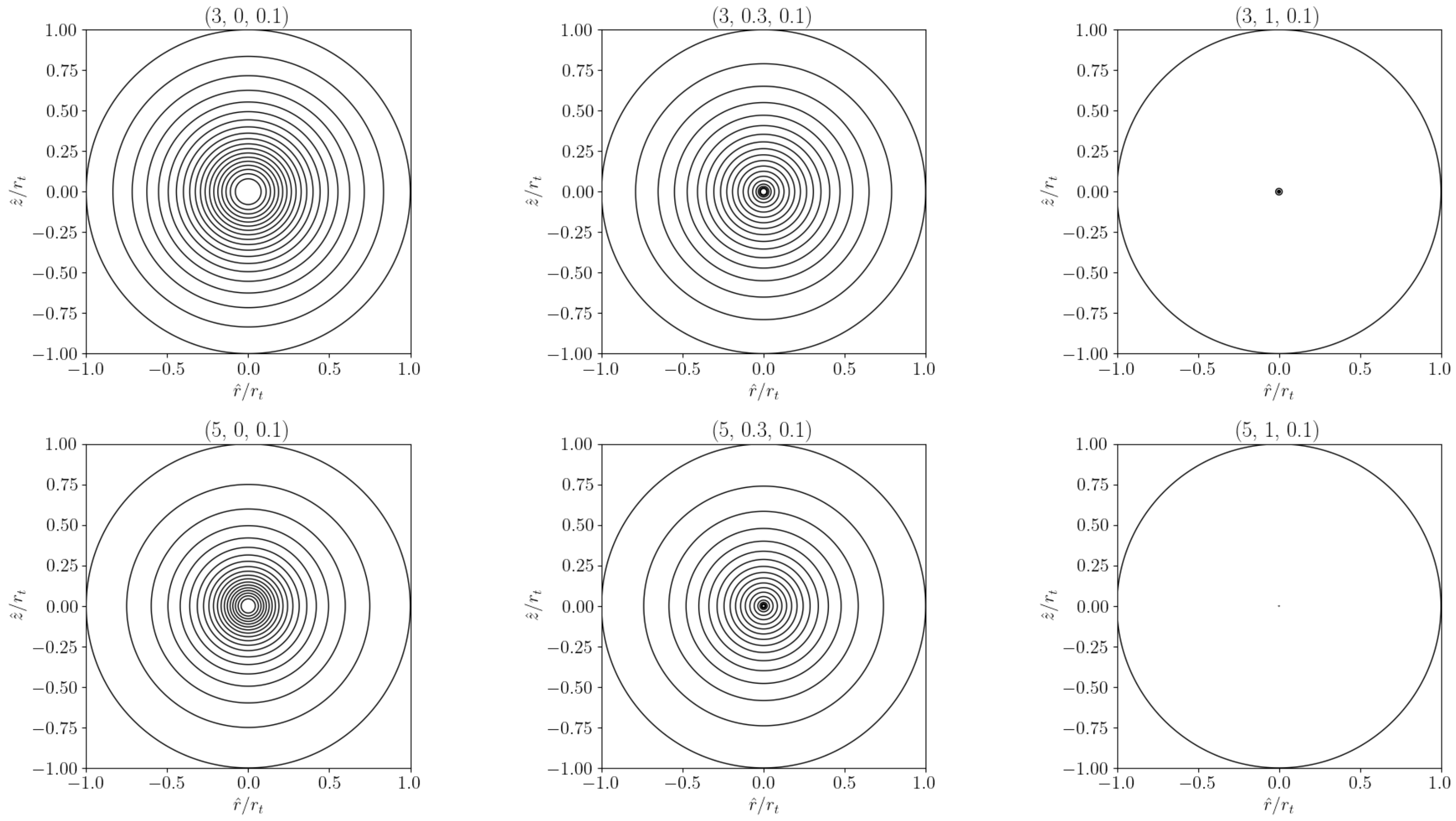

Figure 3.7: As Fig. 3.6 but for the corresponding non-rotating LoKi models generated in Chapt. 2

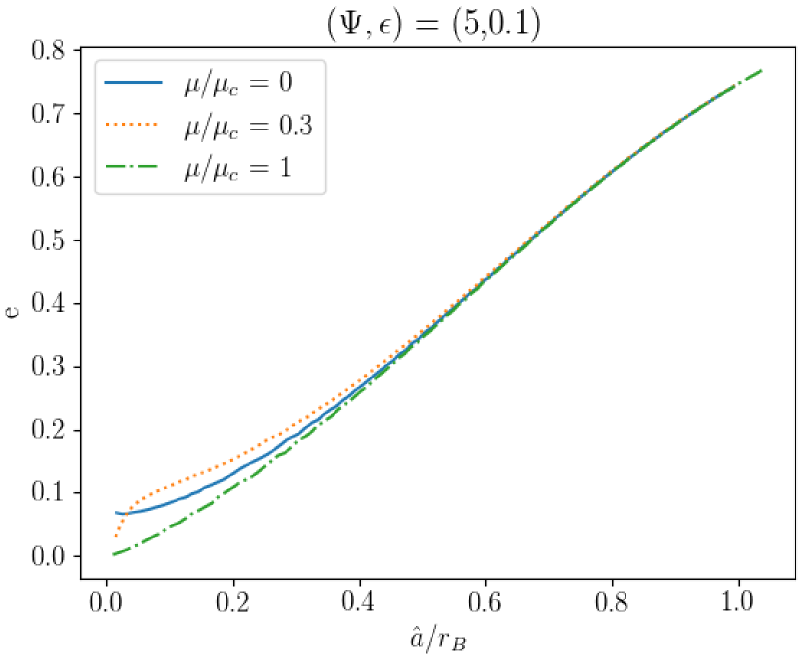

Figure 3.8: Eccentricity profiles as a function of semi-major axis, $\hat{a}$ for three models with varying black hole mass, given as a fraction of the critical black hole mass. The models are also illustrated in the bottom row of Fig. 3.6.

geometry in this region is dominated by the centrifugal potential which retains the same quadratic form regardless of black hole mass.

3.7 Thermodynamic quantities

To obtain the suitably normalised inverse temperature, β, and total energy $\mathcal{E}$ we must first calculate the mass and total potential energy of the system (see Sect. VI Chavanis et al. 2015a for a discussion on this normalisation).

By definition, the mass is given by

$$\begin{aligned} M &\equiv \int \rho(\boldsymbol{r}) d^3\boldsymbol{r} \\ &= \hat{A} r_K^3 2\pi \int_0^{\pi} \int_{\epsilon}^{R(\theta)} \hat{\rho}(\psi(r,\theta)) r^2 \mathrm{d}r \mathrm{d}\theta \equiv \hat{A} r_K^3 \hat{M}, \end{aligned} \tag{3.55}$$

where $R(\theta)$ is the radius at which $\psi(R(\theta),\theta) = 0$; we have used equations (3.6) and (3.8) to express the mass in dimensionless form. We further simplify the calculation by only taking the radial integral between $r = \epsilon$ and $r = r_t$. The low-density envelope, which is excluded by this approximation to spherical symmetry, does not contribute, at first-order in χ, to the total mass.

Now, by substituting the first-order expansion for ψ given by equation (3.50) into equation (3.55), we may obtain $\hat{M}$ also as an expansion in χ. This is achieved by using equations (3.13) and (3.30) to perform the necessary integrations. This results in a dimensionless mass given by

$$\hat{M} = -\frac{4\pi\hat{\rho}(\Psi)}{9}\left(\frac{9\mu}{4\pi} + \lambda_0 + \chi\lambda_1\right) + O(\chi^2). \tag{3.56}$$

This approximation for the mass has been checked against a numerical integration of the density over the full domain and it has been found to produce relative errors of 10^{-3} or lower over the entire parameter space of the family of models.

Then, following Chavanis et al. (2015a) (see especially Sect. III, D and E), we introduce the inverse temperature

$$\beta \equiv aG^2M_C^{4/3}(8\sqrt{2}\pi Ae^{-aH_0})^{2/3} = \frac{81\cdot 3^{2/3}}{16\pi^2\hat{\rho}(\Psi)^2}\hat{M}^{4/3}. \tag{3.57}$$

The expression here differs subtly from that seen in Chapt. 2 due to the different dimensional scaling of M adopted in equation (3.55).

Similarly, we may introduce the total potential energy defined (see Binney & Tremaine 2008) by

$$U = \frac{1}{2}\int \rho(\boldsymbol{r})\Phi_C(\boldsymbol{r})\mathrm{d}^3\boldsymbol{r}, \tag{3.58}$$

which, after making use of equations (3.2), (3.3), (3.5), (3.6), and (3.8), becomes

$$U = \frac{r_K^3\hat{A}}{a}\pi\int_0^{\pi}\int_{\epsilon}^{R(\theta)}\hat{\rho}(r,\theta)\,[aH_0 - \psi(r,\theta) \tag{3.59}$$

$$+\frac{9}{2}\chi r^2\sin^2(\theta) + \frac{9\mu}{4\pi r}\Big]\, r^2\sin(\theta)\mathrm{d}r\mathrm{d}\theta \equiv \frac{r_K^3\hat{A}}{a}\hat{U}. \tag{3.60}$$

By recalling the boundary condition (3.34), along with our expansion for the exterior solution given by equation (3.35), we may conclude that

$$aH_0 = \alpha = \alpha_0 + \chi\alpha_1 + O(\chi^2), \tag{3.61}$$

which allows us to simplify the expression slightly as

$$\hat{U} = \frac{1}{2}\alpha\hat{M} - \pi\int_0^{\pi}\int_{\epsilon}^{R(\theta)}\hat{\rho}(r,\theta)\left[\psi(r,\theta) - \frac{9}{2}\chi r^2\sin^2(\theta)\right.$$
$$\left. -\frac{9\mu}{4\pi r}\right] r^2\sin(\theta)\mathrm{d}r\mathrm{d}\theta. \tag{3.62}$$

We may then apply the virial theorem to obtain the total energy of the system $E_{\mathrm{tot}} = U/2$. Suitably normalised (see Chavanis et al. 2015a), we then obtain the final expression as

$$\mathcal{E} = -\frac{8\pi^2\hat{\rho}(\Psi)^2}{3^{14/3}}\frac{\hat{U}}{\hat{M}^{7/3}}. \tag{3.63}$$

It is interesting to ask how the introduction of slow rigid body rotation affects the structure of the caloric curves obtained in Chapt. 2. For the LoKi models, we recall that the addition of a central black hole resulted in the appearance of a second branch in the caloric curve corresponding to models with black hole masses in the vicinity of, and greater than, the identified critical black hole mass $\mu = \mu_c$. At this black hole mass, a first-order microcanonical phase transition occurs associated with the sharp transition in the extent and mass of the stellar system in that regime.

In Fig. 3.9, we can see that the effect of rotation is highly dependent upon which portion of the parameter space the specific model lies. In the case of a sub-critical model ($\chi < \chi_c$), the caloric curve from the LoKi models is perturbed only slightly. To appreciate this feature, we may Taylor expand both equations (3.57) and (3.63) in χ. Using these expansions we may explicitly calculate the first-order corrections, β_1 and $\mathcal{E}_1$, to the non-rotating values of β and $\mathcal{E}$ as

$$\beta_1 = \frac{27 \cdot 3^{2/3}}{4\pi^2 \hat{\rho}(\Psi)^2} \hat{M}_0^{1/3} \hat{M}_1 \tag{3.64}$$

$$\mathcal{E}_1 = -\frac{8\pi^2 \hat{\rho}(\Psi)^2}{3^{14/3}} \frac{3\hat{U}_1 \hat{M}_0 - 7\hat{U}_0 \hat{M}_1}{3\hat{M}_0^{10/3}}, \tag{3.65}$$

where $\hat{M}_0$, $\hat{M}_1$, $\hat{U}_0$, and $\hat{U}_1$ arise from the Taylor expansions of equations (3.56) and (3.62). It is then easily verified that this linear approximation well describes the behaviour of β and $\mathcal{E}$ over the full range of accessible values of the rotation strength parameter, hence the effect of rotation manifests itself at order χ.

However, if the model is super-critical ($\chi > \chi_c$) then no physical solution exists. Thus, along a sequence of equilibria with fixed (ϵ, χ, μ) the observed decrease in χ_c around μ_c observed in Fig. 3.3 manifests itself as a break in the caloric curve. The two-branch structure remains, but we no longer have a continuous sequence of equilibria.

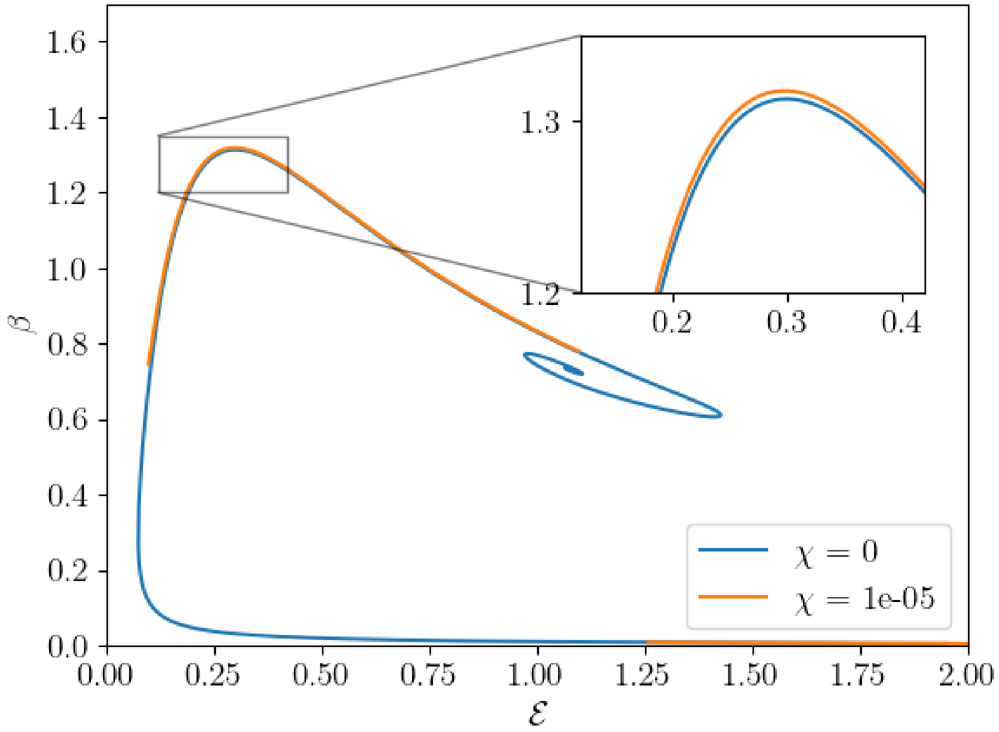

Figure 3.9: Caloric curves for models with $(\epsilon, \mu) = (0.1, 0.3)$ and a_0 varying from 25 at the centre of the spiral, to 0.01 at the terminal point on the lower branch. Both curves have been generated via the asymptotic method outlined in Sect. 3.4. We present both the LoKi models in blue and a series of models with the same value of the rotation strength parameter in orange.

3.8 Summary and discussion

In this chapter, we have presented an extension to the class of models introduced in Chapt. 2 to account for the presence of rigid body internal rotation. We have presented a description of these models via their intrinsic properties including a thermodynamic characterisation. The resulting models are axisymmetric, flattened configurations with significant central gradients depending on the mass of the central black hole. Thermodynamically, we retain the two-branch structure of the caloric curves identified in Sect. 2.8, however, we now have the possibility of a break in the caloric curve, providing a discontinuous sequence of equilibria if the rotation strength is sufficiently large.

The first solution approach provided in this chapter relies on a spectral iteration method. This approach presents the potential of further extensions to the case differential rotation (see Varri & Bertin 2012 for the construction of a family of differentially rotating equilibria without a central black hole). Such a generalisation would provide a framework for the inclusion of further kinematic complexity, offering physically realistic models of stellar systems with central black holes.

The second solution procedure using asymptotic expansions allows for the efficient calculation of the solution and enables an in-depth exploration of the admissible parameter space of the models. Using this approach, we were also able to assess the origin of the different behaviours observed in the solutions. Specifically, we note that the overall structure of the system is determined primarily by the corresponding unperturbed LoKi model, particularly in the central regions. The addition of rotation manifests itself in the breaking of the spherical symmetry and it represents the primary driver of the structure of the solution in the outskirts of the system.

Chapter 4

Bayesian inference for truncated isothermal spheres from discrete phase space data

In the previous two chapters, we have developed models describing globular clusters with massive central black holes, both with and without rigid rotation. We now turn our attention to the task of fitting the parameters of these models to data.

Traditionally this has been accomplished via the fitting of theoretical surface brightness profiles, usually of the King (1966) variety, to observed surface brightness profiles (see Trager et al. (1995), and McLaughlin & van der Marel (2005) for example). In some cases, when limited radial velocity data is also available, the surface brightness profiles can be supplemented using velocity dispersion profiles constructed from this data, as in early studies conducted by Gunn & Griffin (1979) for M3, Meylan & Mayor (1991) for NGC 6397, and Meylan et al. (1995) for ω Centauri. One of the downsides of these methods is that they are susceptible to biases due to small numbers of very luminous stars.

More recently, high-resolution photometric and astrometric Hubble Space Telescope data has provided morphologic and kinematic coverage of the crowded central regions of many Galactic globular clusters, allowing us to resolve many more individual stars in these traditionally challenging regions. This has been combined with data from ground-based campaigns to obtain resolved star positions and velocities (generally along the line of sight) over the full radial extent of several Galactic globular clusters, with reasonable completeness (see Gaia-ESO survey by Gilmore et al. 2012, and more targeted initiatives, e.g. MIKiS survey by Ferraro et al. 2018). This data has allowed the construction of projected density and velocity dispersion profiles using individual star counts in annular bins (for photometric studies, see e.g. Miocchi et al. 2013, Pallanca et al. 2021; for kinematic studies, see e.g., Lanzoni et al. 2013, Leanza et al. 2023, and references therein). Such methods help alleviate the problems related to the presence of individual luminous stars in a dataset, as each star provides the same contribution to the resulting number density profiles.

However, we now possess a large number of stars for which we have full six-dimensional data, primarily thanks to the astrometric data obtained by the Gaia satellite (Gaia Collaboration et al. 2023). Such data can be used to supplement existing number density profile-based methods (see de Boer et al. 2019, and Pallanca et al. 2023 for example), but the availability of this additional phase space information raises further possibilities. Rather than relying on constructing radial profiles of projected moments, it seems most efficient to solely use the individual star data, bypassing the need for any binning. This three-dimensional data in velocity space has already allowed the community to characterise the internal kinematics of several Galactic globular clusters. Specific recent examples concern the investigation of the presence of internal rotation (see Bianchini et al. 2018, Sollima et al. 2019, and Vasiliev & Baumgardt 2021 among others), anisotropy in the velocity space (see e.g. Jindal et al. 2019 and Bianchini et al. 2019), and the density distribution and kinematics of stars in tidal tails originated from nearby progenitor star clusters (see Kuzma et al. 2022, Sollima 2020 and references therein). Some attempts to exploit individual phase space data for model selection purposes have recently been conducted (see Eadie et al. 2022, Wen et al. 2024), but much of the methodology remains to be established.

In the rest of this chapter we formulate a Bayesian framework designed to exploit the phase space information contained within this new generation of discrete data sets, first for the fitting of King (1966) models, then considering the extension to the LoKi models detailed in Chapt. 2.

4.1 Synthetic phase space data generation

We describe the generation of synthetic data using the LoKi models introduced in Chapt. 2. Initially, we consider the classical King (1966) models obtained by setting $\epsilon = \mu = 0$ within the LoKi models. Extension to the case of a non-zero μ is possible by calculating the dimensionless escape energy, ψ, as the solution to equation (2.16) rather than the classical King (1966) solution, otherwise the overall procedure is the same.

To generate discrete data we must obtain individual samples of the velocity and positions of the stars. Specifically, we aim to generate the set $X = \{(x, y, z, v_x, v_y, v_z)_i\}_{i=1}^{N}$. Here we define (x, y) as our coordinates in the plane of the sky, and z as the coordinate along the line of sight with the origin located at the centre of the cluster.

To obtain the position and velocity of an individual star we follow the general method outlined in Chapt. 8 of Aarseth (2003). This is not a unique prescription for sampling from a distribution function, see Sellwood (2024) who presents a method based on first sampling from the distribution function in terms of integrals of motion before assigning positions and velocities. Recall the dimensionless density profile associated with the King model

$$\hat{\rho}(\psi) = e^{\psi}\gamma\left(\frac{5}{2}, \psi\right). \tag{4.1}$$

This expression, when suitably normalised, provides us with a probability distribution on the dimensionless radial position, $\hat{r}$, for a given star. Since equation (4.1) is a dimensionless density, the required normalisation is provided via division by the total dimensionless mass, $\hat{M}_C$, of the cluster given by equation (2.19). The resulting probability density on the dimensionless radial position is provided by

$$p(\hat{r}) = \frac{\hat{\rho}(\psi(\hat{r}))}{\hat{M}_C}. \tag{4.2}$$

We may then integrate equation (4.2) over configuration space to obtain the cumulative distribution function

$$P(\hat{r}) = 4\pi \int_0^{\hat{r}} \hat{r}^2 p(\hat{r}) \mathrm{d}\hat{r}, \tag{4.3}$$

this function is analogous to the mass enclosed within a radius $\hat{r}$, normalised so that $P(\hat{r}_t) = 1$. To obtain a sample of the radius we first sample a uniformly distributed random number $X_1 \sim U[0,1]$, the radius sample is then obtained as

$$\hat{r} = P^{-1}(X_1), \tag{4.4}$$

where P^{-1} is the inverse of equation (4.3). We can then obtain $(\hat{x}, \hat{y}, \hat{z})$ from this radial sample by sampling $X_2, X_3 \sim U[0,1]$ and using equation (8.8) from Aarseth (2003), repeated here as

$$\hat{z} = (1 - 2X_2)\hat{r}, \tag{4.5}$$

$$\hat{x} = (\hat{r}^2 - \hat{z}^2)^{\frac{1}{2}} \cos(2\pi X_3), \tag{4.6}$$

$$\hat{y} = (\hat{r}^2 - \hat{z}^2)^{\frac{1}{2}} \sin(2\pi X_3). \tag{4.7}$$

Now that the star's position is fixed, the distribution function (2.1) may be used to provide a probability density for the modulus of the velocity vector, $\hat{v}$. We thus have that

$$p_{\hat{r}}(v) \propto e^{\psi(\hat{r}) - \hat{v}^2/2} - 1, \quad \hat{v} \in \left[0, \sqrt{2\psi(\hat{r})}\right]. \tag{4.8}$$

The appropriately normalised cumulative distribution function associated with this probability density is obtained by integrating over the velocity space to provide

$$P_{\hat{r}}(\hat{v}) = \frac{4\pi \int_0^{\hat{v}} s^2 p_{\hat{r}}(s) \mathrm{d}s}{4\pi \int_0^{\sqrt{2\psi(\hat{r})}} s^2 p_{\hat{r}}(s) \mathrm{d}s} = \frac{\gamma(3/2, \hat{v}^2/2) - \hat{v}^{3/2}}{\gamma(3/2, \psi(\hat{r})) - (2\psi(\hat{r}))^{3/4}}. \tag{4.9}$$

We then proceed in the same manner as the radial variable to obtain $(\hat{v}_x, \hat{v}_y, \hat{v}_z)$.

To generate this set of dimensionless positions and velocities, we only required one parameter, the central dimensionless escape energy, Ψ. However, astronomical data is expressed in physical units so we must provide two further parameters. In this chapter, we select the King radius, r_K, defined by equation (3.8), and the total mass of the cluster M. It is important to note that this is not a unique choice. These may be any two parameters that allow us to fully specify the physical scales present in equation (2.1). For example, we could have selected r_K and the central density of the cluster, ρ_0. We also tested using r_K and $\hat{A}$, defined as in equation (2.3) and found that the choice of $\{r_K, M\}$ performed better than the other two choices in the inference process.

The set of parameters required to generate a data set, with positions and velocities expressed in physical units, is then $\{\Psi, M, r_K\}$. Once these parameters are fixed we may then obtain the components of the discrete data, expressed in physical units, by taking

$$x = r_K \hat{x}, \tag{4.10}$$

$$v_x = a^{-\frac{1}{2}} \hat{v}_x, \tag{4.11}$$

and similarly for the other components, where the remaining dimensional scale a is calculated as

$$a = \frac{9 r_K \hat{M}_C(\Psi)}{4\pi G M}. \tag{4.12}$$

This process can then be repeated N times to provide our set of synthetic discrete data. In App. E we present checks on the density profile, velocity dispersion profile, and virial ratios of data set generated using the method outlined in this section.

4.2 Bayesian parameter inference

We now possess a set, X, of single-star data for N stars. To fit a model to this data we must determine which set of parameters $\theta = \{\Psi, M, r_K\}$ generated our data.

First, we recall that the choice of normalisation for the distribution function is not unique. Thus far we have primarily considered this function to represent a physical density in phase space. If we retain this meaning on the physical scale A, then a probability density for the position and velocity of a single star may be written as

$$l_{6d}(x, y, z, v_x, v_y, v_z) = \begin{cases} \frac{A}{M} e^{-aE_0} \left[e^{-a(E-E_0)} - 1 \right], & E \leq E_0, \\ 0, & E > E_0, \end{cases} \tag{4.13}$$

where the subscript indicates that we have full six-dimensional phase space data available. The case where we are restricted in the available phase space information is considered in Sect. 4.5.

Each star in our synthetic data set, $X = \{r_i, v_i\}_{i=1}^{N}$, is independently sampled from the distribution function. Thus, the likelihood of a specific set of data given parameters θ, is given by the product of the individual star likelihoods,

$$l(X|\theta) = \prod_{i=1}^{N} l_{6d}(\boldsymbol{r}_i, \boldsymbol{v}_i). \tag{4.14}$$

We now introduce the key object of interest in a Bayesian formulation, the posterior probability density. For more details, we refer the reader to MacKay (2003) and Robert (2007).

We are interested in $P(\theta|X)$, the likelihood of a set of parameters given the data. This is the posterior probability density. To obtain an expression for the posterior we use Bayes' theorem to write

$$P(\theta|X) = \frac{l(X|\theta)p(\theta)}{p(X)}. \tag{4.15}$$

We already have an expression for the likelihood, $l(X|\theta)$, given by equation (4.14). The term $p(\theta)$ in equation (4.15) is the prior distribution and encompasses our assumed knowledge of the parameters before any inference. To begin constructing our prior distribution we assume that the true parameter values lie within some finite region of the parameter space, Θ.

We shall first assume that we have physically motivated upper and lower bounds for each of our three parameters so that

$$\begin{aligned} \Theta = \{ \{M, r_K, \Psi\} : \Psi_{\min} \le \Psi \le \Psi_{\max},\ r_{K\min} \le r_K \le r_{K\max}, \\ M_{\min} \le M \le M_{\max} \} . \end{aligned} \tag{4.16}$$

Once the physical constraints on the parameter values are set, we can further reduce the volume of the parameter space in which the true parameters lie. Recall that the distribution function for the King (1966) model (2.1) is truncated at an energy E_0. Thus, if a dataset contains a single star $(\boldsymbol{r}_i, \boldsymbol{v}_i)$ such that $E > E_0$, then the likelihood for the whole dataset will be zero. This fact can be used to reduce the admissible portion of the parameter space for a given dataset.

Let $\{\Psi^*, M^*, r_K^*\}$ represent the true parameter values. This set of parameters defines a curve in phase space, illustrated by the black line in Fig. 4.4, such that samples from the true distribution function must fall within the region enclosed by this curve and the coordinate axes. Let $\mathcal{S}(\Psi^*, M^*, r_K^*)$ represent this region. For a set of candidate parameters $\{\Psi, M, r_K\}$ there is a similarly defined region $\mathcal{S}(\Psi, M, r_K)$. The set of admissible parameter values, given that the true parameters are known, is then provided by

$$\Omega^* = \{ \{\Psi, M, r_K\} : \mathcal{S}(\Psi^*, M^*, r_K^*) \subseteq \mathcal{S}(\Psi, M, r_K) \} . \tag{4.17}$$

The criterion for the above set can be thought of as the requirement that any potential sample from the true distribution should have a non-zero likelihood under a candidate set of parameters, otherwise, we may immediately rule them out.

One useful implication of the above definition of the admissible region is that the true set of parameters, $\theta^* = \{\Psi^*, M^*, r_K^*\}$, will always lie upon the boundary of the admissible region.

The simplest illustration of this fact is to consider the point $(r_t^*, 0)$ where $r_t^* = r_K^* \hat{r}_t^*$ is the truncation radius of the true model. If we allow variation only in r_K, i.e. $\delta\theta = \{0, 0, \delta r_k\}$, then the truncation radius of a new model calculated using parameters $\theta = \theta^* + \delta\theta$ is then given by

$$r_t = r_t^* + \delta r_K \hat{r}_t^*. \tag{4.18}$$

Here we recall that dimensionless quantities are denoted by hats. Thus, $\hat{r}_t^*$, is the dimensionless truncation radius and is dependent only upon Ψ^*.

Suppose $\delta r_K < 0$, and consider the point $(r_t^* + \delta r_K \hat{r}_t^*/2, 0)$. Under the true parameters θ^* a star at this location in phase space has a non-zero likelihood. Under the new parameters $\theta^* + \delta\theta$ the likelihood function vanishes at this location due to the truncation in phase space. This applies also to any $\delta r_K < 0$ and so $\theta^* \in \partial\Omega^*$. Similar arguments follow by considering variation only in Ψ for this point, and variation only in M, if we consider the point $(0, \sqrt{2\Psi}/a)$ instead.

The definition (4.17) relies on having full knowledge of the true parameters to determine $\mathcal{S}(\Psi^*, M^*, r_K^*)$, however, we possess only a finite number of stars, X, sampled from the true distribution function. As such there will be regions of $\mathcal{S}(\Psi^*, M^*, r_K^*)$ that remain unsampled. The logic that any sample from the true distribution function should have a non-zero likelihood under any admissible set of parameters may still be used. The admissible parameter space, given a finite set of stars, is then given by

$$\Omega = \{\{\Psi, M, r_K\} : x \in \mathcal{S}(\Psi, M, r_K)\ \forall x \in X\}. \tag{4.19}$$

This then provides an estimate of Ω^*, and as $N \to \infty$ we will recover Ω^*.

We are now able to define the prior distribution that we will use in our inference process. Next, we choose a uniform distribution on Ω as the prior distribution. Specifically, we take

$$p(\theta) = \begin{cases} \frac{1}{V}, & \theta \in \Omega, \\ 0, & \text{Otherwise,} \end{cases} \tag{4.20}$$

where

$$V = \int_\Omega \mathrm{d}^3\Omega. \tag{4.21}$$

We stress that this is not a unique choice and more complex definitions of the prior are possible (e.g., see Chapt. 3 in Robert 2007).

The factor $p(X)$ in equation (4.15) is the evidence, and is defined by

$$p(X) = \int_\Omega l(X|\theta) p(\theta) \mathrm{d}^3\theta. \tag{4.22}$$

In many instances, this integral can be computationally intractable. In the case of the King (1966) models, this integral is three-dimensional and defined on a finite domain, Ω, therefore we may explicitly calculate this integral by using a standard Simpson's rule integration. The only potential computational issue arising here is the magnitude of the likelihood (4.14), especially for large numbers of stars where the log-likelihood is too small for the likelihood to be expressed as a floating point number. This issue can be avoided by noting that

$$\begin{aligned} \ln p(X) &= \ln\left(\frac{1}{V}e^{\ln l^*}\int_\Omega e^{\ln l(X|\theta)-\ln l^*}\mathrm{d}^3\theta\right), \\ &= \ln l^* - \ln V + \ln\int_\Omega e^{\ln l(X|\theta)-\ln l^*}\mathrm{d}^3\theta \end{aligned} \tag{4.23}$$

where we have explicitly used equation (4.20), and defined

$$\ln l^* = \max_{\theta\in\Omega} \ln l(X|\theta).$$

In this way, we only perform calculations using differences in log-likelihoods, which have larger magnitudes than individual log-likelihoods. This provides a region around the maximum of the likelihood function in which the integrand in equation (4.23) can be numerically evaluated as non-zero. Points in the domain where the difference in log-likelihoods is still so large that the integrand evaluates to zero remain, however, these provide a negligible contribution towards the integral.

The appropriately normalised posterior can therefore be evaluated by combining equations (4.15), (4.20), and (4.23) to provide

$$\ln P(\theta|X) = \ln P(X|\theta) - \ln P(X) + \ln P(\theta). \tag{4.24}$$

All quantities of interest can now be calculated from the posterior density. First, we can calculate

$$\theta_{\mathrm{MAP}} = \arg\max_{\theta\in\Omega} P(\theta|X). \tag{4.25}$$

This is the maximum a posteriori (MAP) estimate of the true parameters. With the choice of a uniform prior distribution used here, this estimate coincides with the usual maximum likelihood estimate, in a Frequentist's interpretation of the statistics. This may be observed from Bayes' theorem (4.15): under a uniform prior we have that $P(\theta|X) \propto l(X|\theta)$, thus the maximum of the posterior and the likelihood will coincide under the choice of a uniform prior. This statement does not hold for alternative choices of prior distribution.

Two further quantities of interest are the mean and covariance matrix of the posterior distribution, which are defined as

$$\bar{\theta} = \int_\Omega \theta P(\theta|X)\mathrm{d}^3\theta, \tag{4.26}$$

and

$$\delta_{ij}^2 = \int_\Omega (\theta_i - \bar{\theta}_i)(\theta_j - \bar{\theta}_j)P(\theta|X)\mathrm{d}^3\theta. \tag{4.27}$$

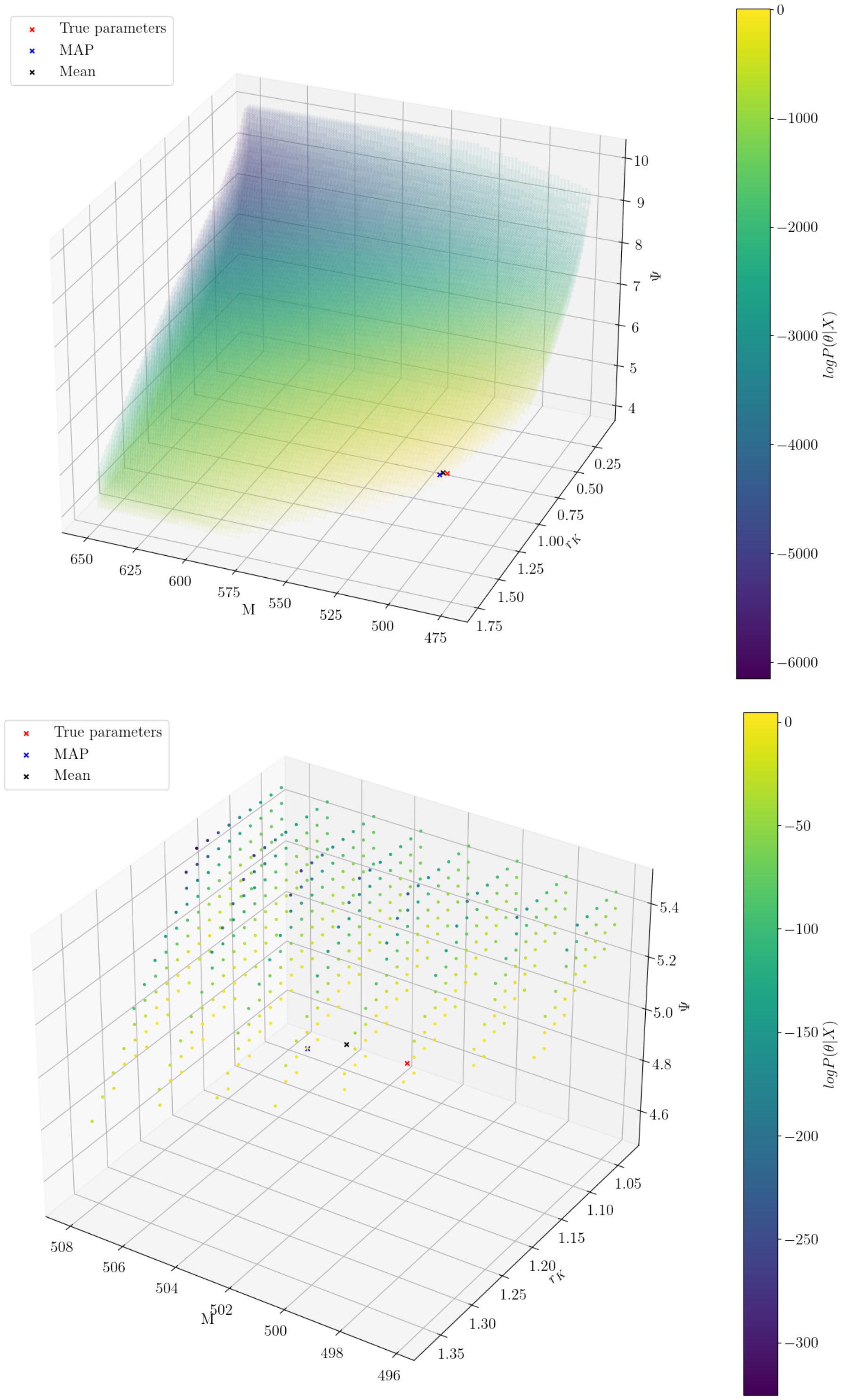

Figure 4.1: Logarithm of the posterior density (4.15). The discrete data set used here was sampled using the parameters $\{\Psi, M, r_K\} = \{5, 500, 1.2\}$. This data set is shown in Fig. 4.3. The posterior has been calculated on a grid of parameter values where the limits of each parameter value were set to ensure that we calculate the posterior over the full range for which there is a high posterior density. We explicitly indicate the MAP estimate obtained via equation (4.25), the mean obtained via equation (4.26), and the true parameters used to generate the samples (blue, red, and black crosses). The bottom panel shows a magnified view centred on the posterior mean located at $\bar{\theta} = \{4.99488, 502.171, 1.20182\}$.

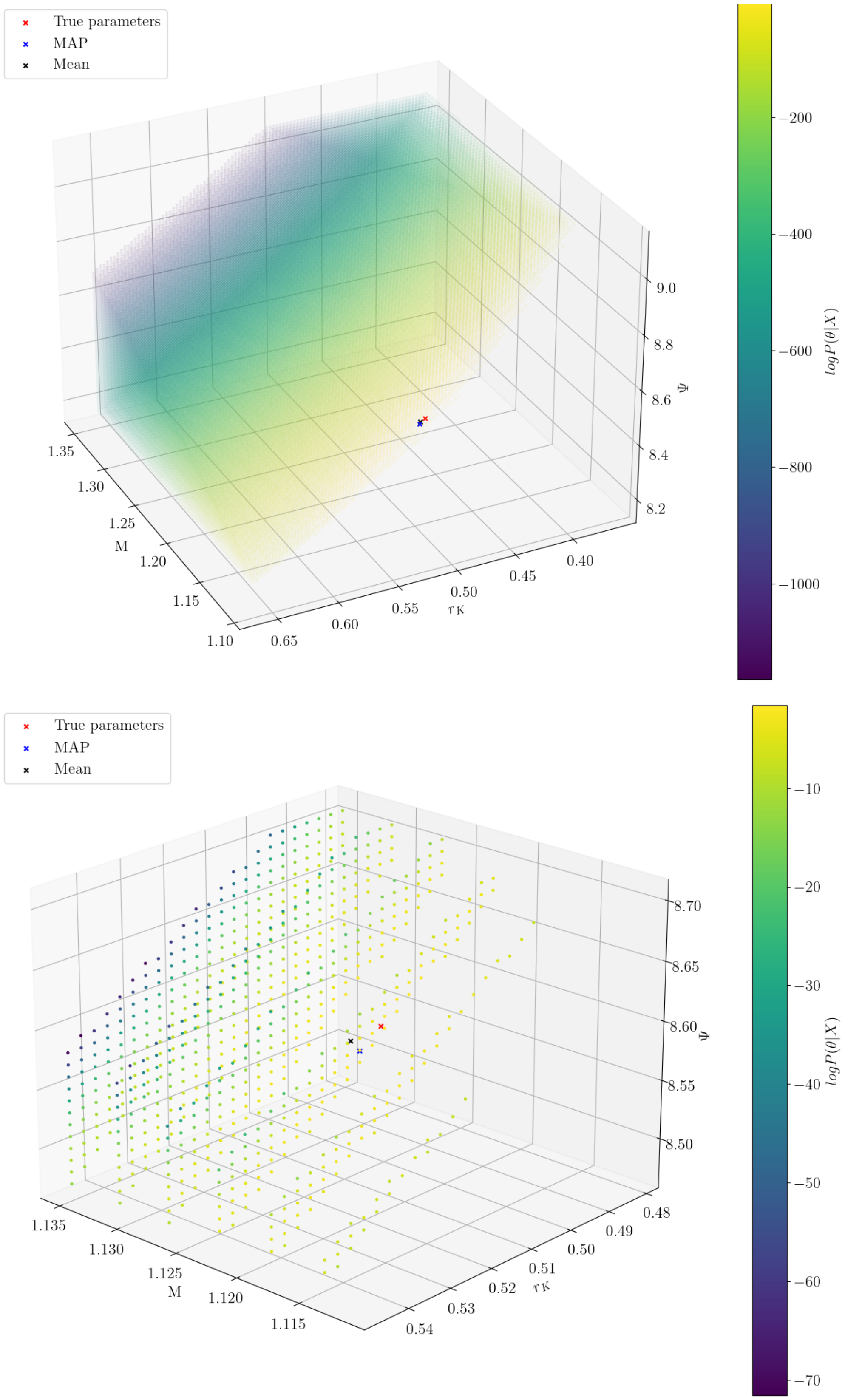

Figure 4.2: As Fig. 4.1, but concerning the inference problem emulating the globular cluster NGC 104 (47 Tucanae). The posterior mean, and the resulting percentage error in this case may be found in Tabs. 4.1-4.3.

4.2.1 Test case: King (1966) model with $\Psi = 5$

We can now test this methodology by applying it to a synthetic data set generated as per Sect. 4.1. We generate samples from the King (1966) distribution with true parameters $\{\Psi, M, r_K\} = \{5, 500, 1.2\}$. These values have been chosen to provide a simple test case for validating the inference process detailed in Sect. 4.2.

In Fig. 4.1 we show the posterior distribution calculated for a single synthetic data set generated with the above-stated parameters. The posterior has been calculated directly using a simple three-dimensional Simpson's rule routine for the integrals in equations (4.23), (4.26), and (4.27). In general, this is an inefficient way to calculate these quantities but, in this case, the relatively low dimension of the parameter space, combined with the narrow physical bounds on the parameters allows this to be practical. If the dimension is much higher (as is the case when inferring the parameters of the LoKi models, see Sect. 4.4), or the bounds on the parameters are too wide to make a reasonable discretisation of the parameter space impractical, then alternative numerical methods to calculate the posterior distribution must be used. One such method will be addressed in Sect. 4.3.

We note that the resulting distribution is unimodal and monotonically decreasing away from the MAP estimate (see the blue cross in Fig. 4.1). The recovered posterior mean is located at $\bar{\theta} = \{4.99488, 502.171, 1.20182\}$, representing a percentage error compared to the true values of $\{0.00102, 0.00434, 0.00152\}$. It is also worth noting that there is a small displacement between the mean and the MAP estimate. This results from the finite size of the admissible region Ω, due to the the truncation in phase space, combined with the observation that the true parameters lie near the boundary of the admissible region. This means that the bulk of the probability density, although still concentrated near the true parameters, is asymmetric about the MAP estimate.

Visually, the procedure detailed above appears to reproduce the true parameters used to generate the samples. We can also compare this by observing the resulting boundary in the $r - v$ plane from the mean parameters compared to the true parameters (black and red lines respectively in Fig. 4.3) where we observe good agreement between these two curves over the majority of the radial extent of the cluster, with the main deviations arising in the sparsely sampled outer region of the cluster.

4.2.2 Emulation of selected Galactic globular clusters

As the inference process appears to perform well on the test case described above, we present an application to a suite of discrete data sets obtained using ten different sets of parameter values. These have been selected from McLaughlin & van der Marel (2005) and have been chosen to cover a range of structural and kinematical properties of Galactic globular clusters, from highly concentrated (e.g., NGC 104), to diffuse (e.g., Pal 5), as well as core-collapsed cases (e.g., NGC 1904, according to the Harris 1996 catalogue, 2010 edition).

As a representative case, we present the equivalent of Figs. 4.1 and 4.3, as resulting from the inference problem corresponding to NGC 104 (47 Tucanae) in Figs. 4.2 and 4.4. We note that, in the case of such physically-motivated values of the parameters, the qualitative behaviour of the posterior density is broadly similar to the one observed in the reference test case. The results of this emulation exercise are presented in full in Tables 4.1-4.3. The small percentage errors and the standard deviations in the fits of all three parameters indicate that this inference procedure is robust over a wide range of physically realistic parameter values.

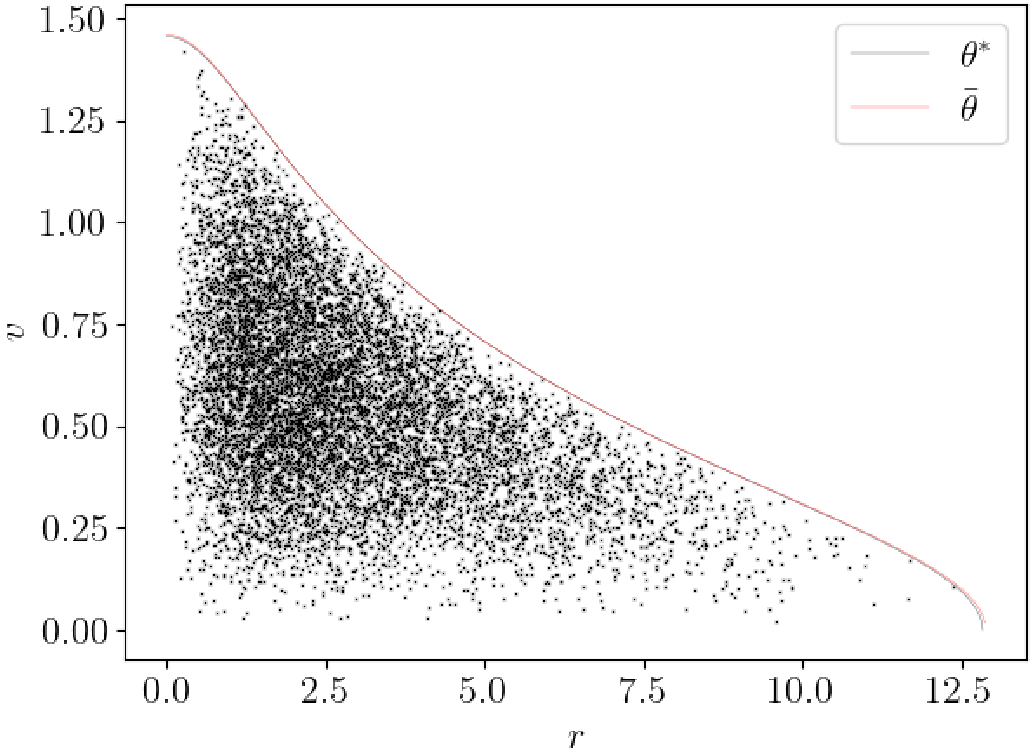

Figure 4.3: An illustration of the boundary in the v-r plane imposed by the truncation in phase space. The black solid line denotes the boundary determined by the true parameters, $\theta^* = \{5, 500, 1.2\}$. The black points are the discrete samples generated from the procedure detailed in Sect. 4.1. The red solid line traces the boundary determined by the mean parameter values, $\bar{\theta}$, of the posterior distribution (4.15) calculated using the discrete data set. Over the majority of the radial extent of the cluster the red and black lines overlap.

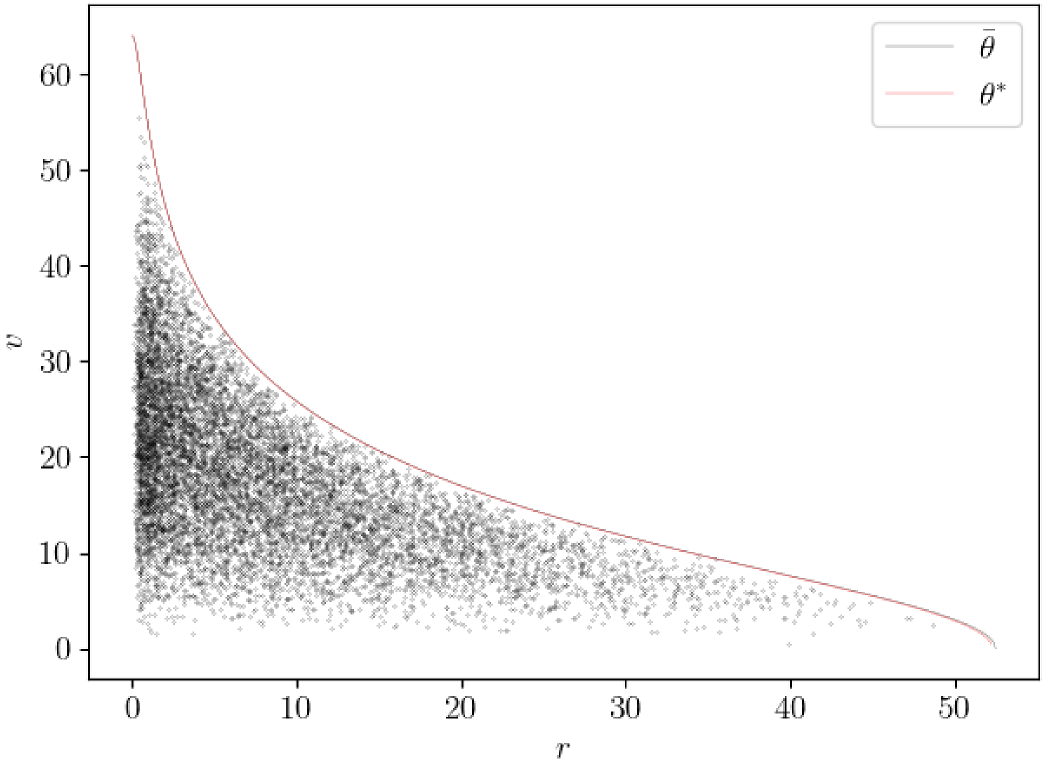

Figure 4.4: As Fig. 4.3, but concerning the inference problem emulating the globular cluster NGC 104 (47 Tucanae). Over the majority of the radial extent of the cluster the red and black lines overlap.

Cluster	$\log_{10} \bar{M}$	$\log_{10} M^*$	M % error	σ_M	$\sigma_M / \bar{M}$
NGC 104	6.052	6.05	0.3967	3809	0.003381
Pal 5	4.168	4.17	0.4652	46.69	0.003171
NGC 6229	5.361	5.36	0.1465	917.3	0.003998
Pal 3	4.647	4.65	0.6322	190.3	0.004287
NGC 7492	4.44	4.44	0.01977	121.6	0.004415
NGC 6809	4.991	4.99	0.2211	400.8	0.004093
NGC 6553	5.502	5.5	0.5288	1505	0.004734
NGC 6402	5.8	5.8	0.05037	2821	0.004469
NGC 5139	6.37	6.37	0.02851	6132	0.002615
NGC 2419	5.947	5.95	0.5911	4276	0.004826
NGC 1904	5.197	5.2	0.5913	591.7	0.003755

Table 4.1: Results of the parameter inference experiments for King (1966) models, emulating a range of different Galactic globular clusters. Each inference process has been performed by using $N = 10000$ synthetic phase space data, obtained as described in Sect. 4.1. The true values of the parameters of the globular clusters (indicated here with stars) have been taken from McLaughlin & van der Marel (2005). We present the mean value of the numerically calculated posterior density (indicated with a bar), as well as the error in that estimate, the standard deviation of the posterior distribution, and its size relative the to mean. The error is calculated as the difference between the true value and the posterior mean.

Cluster	$\bar{r}_K$	r_K^*	r_K % error	σ_{r_K}	$\sigma_{r_K}/\bar{r_K}$
NGC 104	0.5207	0.51	2.106	0.01518	0.02916
Pal 5	23.86	24.17	1.27	0.03105	0.001301
NGC 6229	1.126	1.14	1.212	0.02145	0.01904
Pal 3	10.39	10.68	2.758	0.1611	0.01552
NGC 7492	8.571	8.41	1.919	0.1294	0.01509
NGC 6809	3.324	3.25	2.281	0.04826	0.01452
NGC 6553	1.036	1.02	1.549	0.01546	0.01493
NGC 6402	2.477	2.44	1.519	0.03499	0.01413
NGC 5139	3.632	3.63	0.04906	0.05751	0.01584
NGC 2419	8.257	8.41	1.825	0.1393	0.01687
NGC 1904	0.6391	0.65	1.67	0.01378	0.02156

Table 4.2: As Table 4.1, but for the King radius, r_K.

Cluster	$\bar{\Psi}$	Ψ^*	Ψ % error	σ_Ψ	$\sigma_\Psi/\bar{\Psi}$
NGC 104	8.574	8.6	0.3021	0.04407	0.00514
Pal 5	2.146	2.1	2.167	0.003711	0.00173
NGC 6229	6.934	6.9	0.4878	0.03221	0.004646
Pal 3	5.376	5.3	1.432	0.03689	0.006862
NGC 7492	3.246	3.3	1.623	0.0479	0.01475
NGC 6809	4.431	4.5	1.527	0.04128	0.009315
NGC 6553	5.575	5.6	0.4454	0.03507	0.00629
NGC 6402	4.775	4.8	0.5231	0.03739	0.007831
NGC 5139	6.22	6.2	0.3271	0.03265	0.005249
NGC 2419	6.538	6.5	0.5833	0.02902	0.004439
NGC 1904	7.53	7.5	0.3956	0.03309	0.004394

Table 4.3: As Table 4.1, but for the dimensionless central escape energy, Ψ.

4.3 Markov chain Monte Carlo methods

We detail an alternate method for the calculation of quantities such as the posterior mean, (4.26), and covariance, (4.27), in a situation where a direct numerical integration of the requisite integrals is not practical. One such method that allows us to obtain estimates of these quantities of interest is the Metropolis-Hastings algorithm.

This is a Markov Chain Monte Carlo method that allows us to obtain samples from a non-normalised probability distribution, such as that in equation (4.15), when the evidence is computationally intractable. The method generates a Markov chain $\{\theta^{(n)}\}_{n=1}^{N}$, by proposing a new set of parameters based on the current position of the chain. The proposal is then accepted or rejected with a probability determined by a ratio of likelihoods. This ratio eliminates the need for the normalisation of the density of interest to be known. The stationary distribution of this chain can then be shown to approach the distribution of interest. Below we present a summary of the algorithm and we refer to Robert (2007) and MacKay (2003) for further details. The algorithm proceeds as follows:

1. Initialise the Markov chain at some $\theta^{(0)}$ such that $P(\theta^{(0)}) > 0$.
2. Propose a new step θ' according to the density $Q(\theta'|\theta^{(n)})$.
3. Calculate the quantity

$$\begin{aligned}\alpha &= \frac{l(\theta'|X)Q(\theta^{n+1}|\theta^{n})}{l(\theta^{n}|X)Q(\theta^{n}|\theta')} \\ &= \frac{P(\theta')l(X|\theta^{n+1})Q(\theta'|\theta^{n})}{P(\theta^{n})l(X|\theta^{n})Q(\theta^{n}|\theta')} \qquad (4.28)\end{aligned}$$

   where we have used Bayes' theorem for the first equality.

4. If $\alpha > 1$ then accept the proposal. Else, accept the proposal with probability α.
5. If the proposal is accepted then set $\theta^{(n+1)} = \theta'$, otherwise set $\theta^{(n+1)} = \theta^{(n)}$.
6. Repeat steps 2-5 until the desired chain length, $\mathcal{N}$, is reached.

Some remarks about the use of this algorithm are in order.

First, we must define the proposal density, $Q(\theta'|\theta^{(n)})$, which specifies how the next step in the chain is determined. In our case, we choose a Gaussian proposal density centred on the current position in the chain, $\theta^{(n)}$, with a fixed predefined covariance matrix $\beta\boldsymbol{C}$ where $\beta > 0$, and $\boldsymbol{C}$ is a diagonal matrix, i.e.

$$\theta'|\theta^{(n)} \sim \mathcal{N}(\theta^{(n)}, \beta\boldsymbol{C}). \qquad (4.29)$$

Some practical considerations about the implementation of the proposal density (i.e., the selection of the elements of $\boldsymbol{C}$, and tuning of β, to obtain a reasonable acceptance rate) are discussed in App. F.

It is also important to note that this choice of proposal density is symmetric so that $Q(\theta'|\theta^{(n)}) = Q(\theta^{(n)}|\theta')$. This property simplifies the calculation of the acceptance probability (4.28) so that we only have to consider the ratio of likelihoods

$$\alpha = \frac{P(\theta')l(X|\theta')}{P(\theta^{n})l(X|\theta^{n})}. \qquad (4.30)$$

The distribution of the samples in the chain $\{\theta^{(n)}\}$ approaches that of equation (4.15) only in the limit of long chain length. A number of the initial samples must be discarded as the chain has not reached its stationary distribution - this is typically called a burn-in period. The length of this burn-in period is not generally calculated a priori and is determined by examining the behaviour of the resulting chain. For example, there are methods based on the chain's autocorrelation as it approaches its stationary distribution (Goodman & Weare 2010). In our case we adopt the criterion from Gelman & Rubin (1992). We repeat the required steps for calculation of the criterion here and refer the reader to Gelman & Rubin (1992) for further discussion.

We simulate m distinct chains, each of length $2n$. The chains begin at starting points distributed about the true set of parameters. The first n elements of the chain are discarded as the burn-in period.

For each of the parameters of interest, θ_i, we then calculate the following quantities

$$\frac{B}{n} = \sum_{i=1}^{m} \frac{\left(\bar{\theta}_i - \bar{\theta}\right)^2}{m-1}, \tag{4.31}$$

$$W = \sum_{i=1}^{m} \frac{\sigma^2_{\theta_i}}{m}. \tag{4.32}$$

Here $\bar{\theta}_i$, and $\sigma^2_{\theta_i}$ are the mean and variance of θ_i respectively. These are calculated using the n samples in the i^{th} chain. $\bar{\theta}$ is then the mean value of θ_i calculated using the mn samples in all of the chains, this provides an estimate of the mean of the target distribution. Here equation (4.31) represents the variance between the individual sequence means, and equation (4.32) the mean of the within-sequence variances.

We then calculate an estimate of the variance of the target distribution as

$$\hat{\sigma}^2 = \frac{n-1}{n} W + \frac{B}{n}. \tag{4.33}$$

We then calculate the quantities

$$\hat{V} = \hat{\sigma}^2 + \frac{B}{mn}, \tag{4.34}$$

$$\begin{aligned} \mathrm{var}(\hat{V}) = {} & \left(\frac{n-1}{n}\right)^2 \frac{1}{m} \mathrm{var}(\sigma^2_{\theta_i}) + \left(\frac{m+1}{mn}\right)^2 \frac{2}{m-1} B^2, \\ & + 2\frac{(m+1)(n-1)}{mn^2} \cdot \frac{n}{m} [\mathrm{cov}(\sigma^2_{\theta_i}, \bar{\theta}^2_i) - 2\bar{\theta}\mathrm{cov}(\sigma^2_{\theta_i}, \bar{\theta}_i)]. \end{aligned} \tag{4.35}$$

Here the covariances and variances are calculated using the n samples within the i^{th} chain. The distribution for θ_i is then summarised via Student's t distribution with centre $\bar{\theta}$, scale given by $\sqrt{\hat{V}}$, and degrees of freedom

$$df = \frac{2\hat{V}^2}{\mathrm{var}(\hat{V})}. \tag{4.36}$$

The extent to which the scale of this distribution may be decreased by continuing to run the chains as $n \to \infty$ is then provided by

$$\sqrt{\hat{R}} = \sqrt{\frac{\hat{V}}{W}\frac{df}{df-2}}. \tag{4.37}$$

Thus, a value close to 1 is ideal as little improvement in the spread of the target distribution may be expected. Conversely, a large value of $\sqrt{R}$ then indicates that a longer chain would provide an improved inference on that parameter.

Assuming that we have a chain that has reached convergence then the samples which are not discarded can then be used to estimate the quantities we are interested in via Monte Carlo estimates of equations (4.26) and (4.27) given by

$$\bar{\theta} \approx \frac{1}{L}\sum_{n=0}^{L} \theta^{(n)} \tag{4.38}$$

and

$$\delta_{ij}^2 \approx \frac{1}{L}\sum_{n=0}^{L} (\theta_i^{(n)} - \bar{\theta}_i)(\theta_j^{(n)} - \bar{\theta}_j). \tag{4.39}$$

4.3.1 Test case: King (1966) model with $\Psi = 5$

We now apply the method detailed in Sect. 4.3 to the discrete phase space data generated as in 4.1. We consider as test case a King (1966) model with parameters $\{\Psi, M, r_K\} = \{5, 500, 1.2\}$. We generate a data set containing $N = 10^4$ stars using these parameters and run the Metropolis-Hastings algorithm to obtain a set of $\mathcal{N} = 10^5$ samples.

Convergence was confirmed by repeating this experiment $m = 10$ times from different initial positions in the admissible parameter space and examining the criterion calculated as in equation (4.37). The values obtained in this case were $\hat{R} = (1.00009, 1.00008, 1.00007)$, with each component relating to one of the three parameters $\{M, r_K, \Psi\}$ respectively. Values close to 1 indicate that there is little to be gained in obtaining a longer chain length, and thus we have reached convergence.

An illustration of the two- and one-dimensional projections of the posterior distribution is shown in Fig. 4.5. We note that we can still recover the true parameters to a good degree of accuracy with the best-fit parameters provided by $\{M, r_K, \Psi\} = \{504, 1.24, 4.92\}$, representing percentage errors of $\{0.0097, 0.037, 0.016\}$.

4.4 Application of MCMC to Loaded King models

We can extend the methodology described in the previous section to the LoKi models. In this case, we retain the same form of the likelihood function provided by equation (4.14), where the dimensionless escape energy is now provided by the solution to equation (2.16), rather than the classical King (1966) solution.

It is important to note that we are introducing a new pair of parameters in this process: the dimensionless inner radius, ϵ, and the dimensionless mass of the

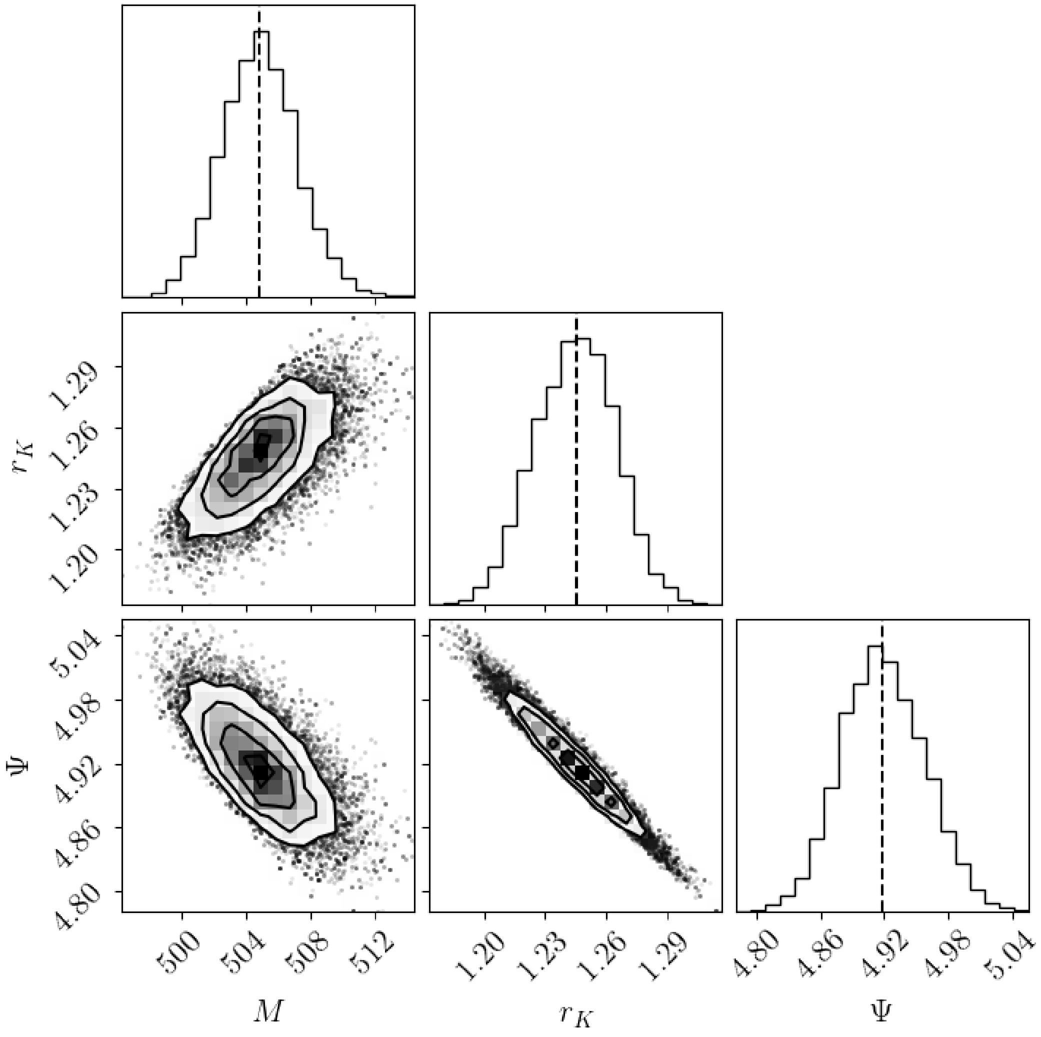

Figure 4.5: Illustration of the one and two-dimensional projections of the posterior distributions (4.15) generated via the Metropolis-Hastings algorithm detailed in Sect. 4.3. The model used to generate the discrete data set is a King model with parameters $\{\Psi, r_K, M\} = \{5, 1.2, 500\}$. We use a data set containing $N = 10^4$ stars and generate a chain containing $\mathcal{N} = 10^5$ samples.

black hole, μ. We may still set physically motivated bounds on the parameters as follows

$$\begin{aligned}\Theta = \{&\{M, r_K, \Psi, \epsilon, \mu\} : \Psi_{\min} \leq \Psi \leq \Psi_{\max},\ r_{K\min} \leq r_K \leq r_{K\max},\ ,\\ &M_{\min} \leq M \leq M_{\max},\ \varepsilon_{\min} \leq \varepsilon \leq \varepsilon_{\max},\ \mu_{\min} \leq \mu \leq \mu_{\max}\}\,. \end{aligned} \tag{4.40}$$

To identify the admissible regions Ω^* and Ω we generalise the definitions introduced in equations (4.17) and (4.19) for the King (1966) models

$$\Omega^* = \{\{\Psi, M, r_K, \varepsilon, \mu\} : \mathcal{S}(\Psi^*, M^*, r_K^*, \varepsilon^*, \mu) \subseteq \mathcal{S}(\Psi, M, r_K, \varepsilon, \mu)\} \tag{4.41}$$

and

$$\Omega = \{\{\Psi, M, r_K, \varepsilon, \mu\} : x \in \mathcal{S}(\Psi, M, r_K, \varepsilon, \mu)\ \forall x \in X\}\,. \tag{4.42}$$

Thus, a uniform prior can again be imposed on the admissible parameter space. However, we encounter an issue when attempting to evaluate the posterior distribution using Bayes' theorem (4.15). The evidence, which, in this case, is given by

$$p(X) = \int_{\Omega} l(X|\theta)p(\theta)\mathrm{d}^5\theta, \tag{4.43}$$

is now a high-dimensional integral that is challenging to evaluate efficiently when a small grid size is required. Thus, we can only obtain the posterior up to a constant of proportionality. This issue may be addressed using the Metropolis-Hastings algorithm detailed in Sect. 4.3.

We test the application of this method to LoKi models by selecting a moderate mass black hole, so that the resulting model lies within Regime 1 (see Sect. 2.4). The parameters we consider are an extension of our previously considered test model, i.e. $\{\Psi, r_K, M, \mu, \epsilon\} = \{5, 1.2, 500, 0.3, 0.1\}$. A synthetic data set containing $N = 2 \times 10^4$ stars is then generated. The Metropolis-Hastings algorithm is then run using this data set as detailed in Sect. 4.3, for a chain length of $\mathcal{N} = 10^5$ samples. The results from this process are summarised in Fig. 4.6.

The resulting posterior distribution is multi-modal and highly scattered, the chain does not appear to have converged to its stationary distribution. This is confirmed via the calculation of the convergence criterion in equation (4.37). We recover values of $\hat{R} \gg 1$ for each parameter, thus indicating that the chains have not converged. We have then tried changing approaches, in an attempt to reach convergence.

First, we fixed one of the newly introduced parameters, ϵ, at its true value. This action reduces the dimension of the parameter space that must be explored. We also recall that for LoKi models with parameters within Regime 1 (see Sect. 2.4), the structure of the system outside of the immediate vicinity of the black hole is largely driven by the combination of parameters $a_0 = \Psi - 9\mu/(4\pi\epsilon)$. Thus, for any given central concentration, there is an inherent degeneracy between the values of μ and ϵ. Therefore, by fixing ϵ, we hoped to reduce the impact of this degeneracy upon the inference process.

The inference process is then performed upon the data set generated previously from the LoKi model with parameters $\{\Psi, r_K, M, \mu, \epsilon\} = \{5, 1.2, 500, 0.3, 0.1\}$. The results are shown in Fig. 4.7. We observed more structure in the resulting distributions, noting the diagonal bands in the $r_K - \mu$, $r_K - \Psi$, and $\mu - \Psi$ plots. However, a high degree of scatter remains, this is especially visible in the projections of the posterior distribution involving the mass M. The chains have not converged to their stationary distribution.

Second, we have considered an alternative set of parameters, by exploiting the freedom attributed to the two physical scales of the models. Specifically, we have conducted the inference process on a LoKi model with parameters $\{\Psi, r_K, \rho_0, \epsilon, \mu\}$

Finally, we also considered providing the mass of the black hole in physical

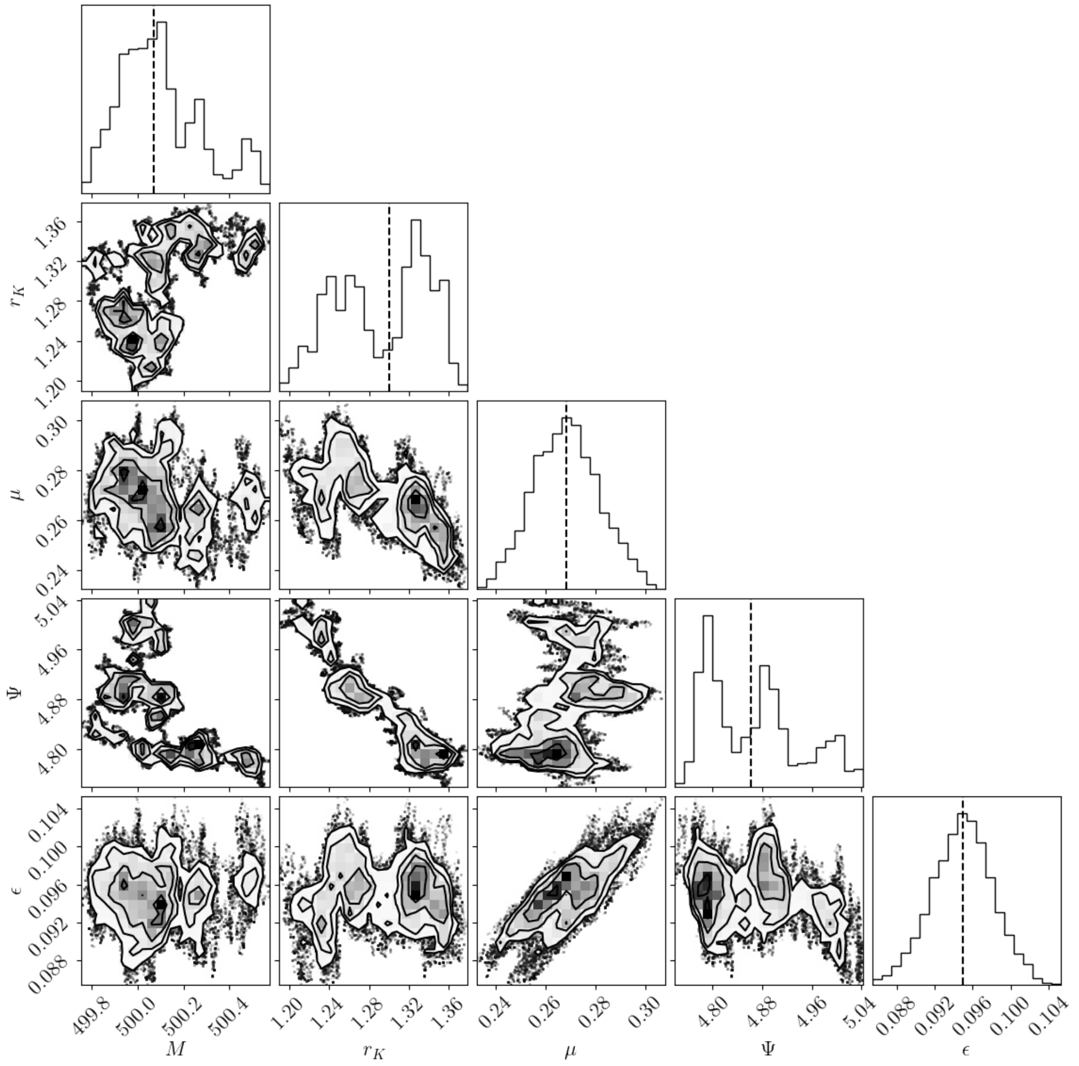

Figure 4.6: Illustration of the one and two-dimensional projections of the posterior distribution (4.15) generated via the Metropolis-Hastings algorithm detailed in Sect. 4.3. The model used to generate the discrete data set used here is a King model with parameters $\{\Psi, r_K, M, \mu, \epsilon\} = \{5, 1.2, 500, 0.3, 0.1\}$. We use a data set containing $N = 2 \times 10^4$ stars and generate a chain containing $\mathcal{N} = 10^5$ samples.

units, M_{BH}, rather than the dimensionless black hole mass, μ. However, upon running the inference process on the data set generated from a LoKi model with parameters $\{\Psi, r_K, M, \mu, \epsilon\} = \{5, 1.2, 500, 0.3, 0.1\}$ using these alternative parameterisations we observed no improvement in convergence compared to our initial set of chosen parameters.

None of the Metropolis-Hastings simulations that we have performed on synthetic data generated from LoKi models with non-vanishing μ and ϵ have reached convergence. We believe that this failure is due to a combination of a higher dimensional parameter space, alongside a sub-optimal choice of proposal density in the Metropolis-Hastings algorithm. This is likely due to stronger

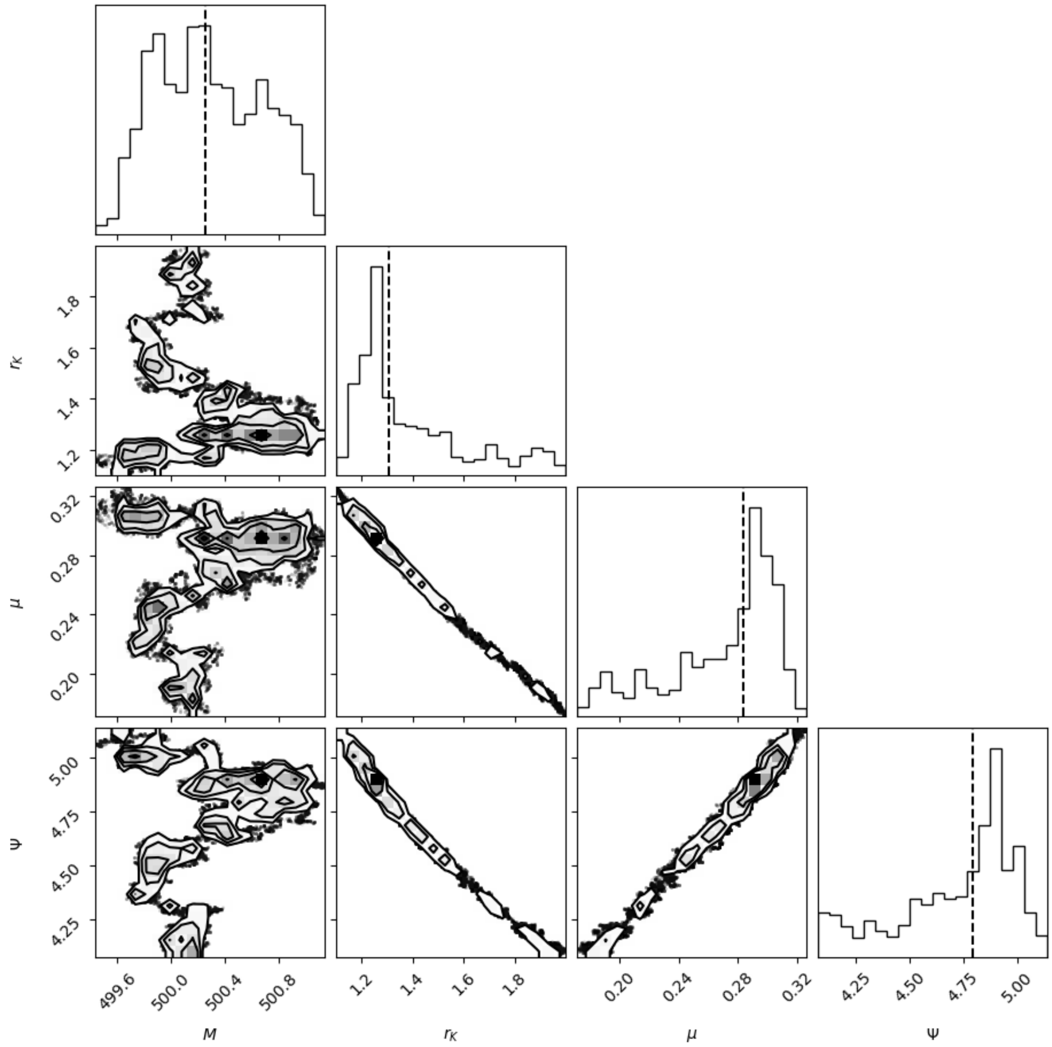

Figure 4.7: As Fig. 4.6, however, the parameter ϵ is kept fixed at the true value.

covariances between the model parameters in the LoKi models, particularly between the parameters μ and ϵ. Due to these covariances, the assumed diagonal proposal density cannot efficiently explore the parameter space. In Sect. 5.2 we present a possible approach to deal with this issue.

4.5 Extension to incomplete phase space data

Thus far we have assumed that full six-dimensional phase space data is available for each star in our data set. In real astronomical data there are often stars that are missing information on one or more components of phase space data (see, e.g. Gaia Collaboration et al. 2023). In this chapter, we restrict our attention to the five-dimensional case where a subset of the stars has no line-of-sight distance, z, and the three-dimensional case where a subset of the stars further lacks proper motion data in the plane of the sky, (v_x, v_y). Alternative scenarios with different missing components may use similar techniques to make use of the specific set of available phase space data components.

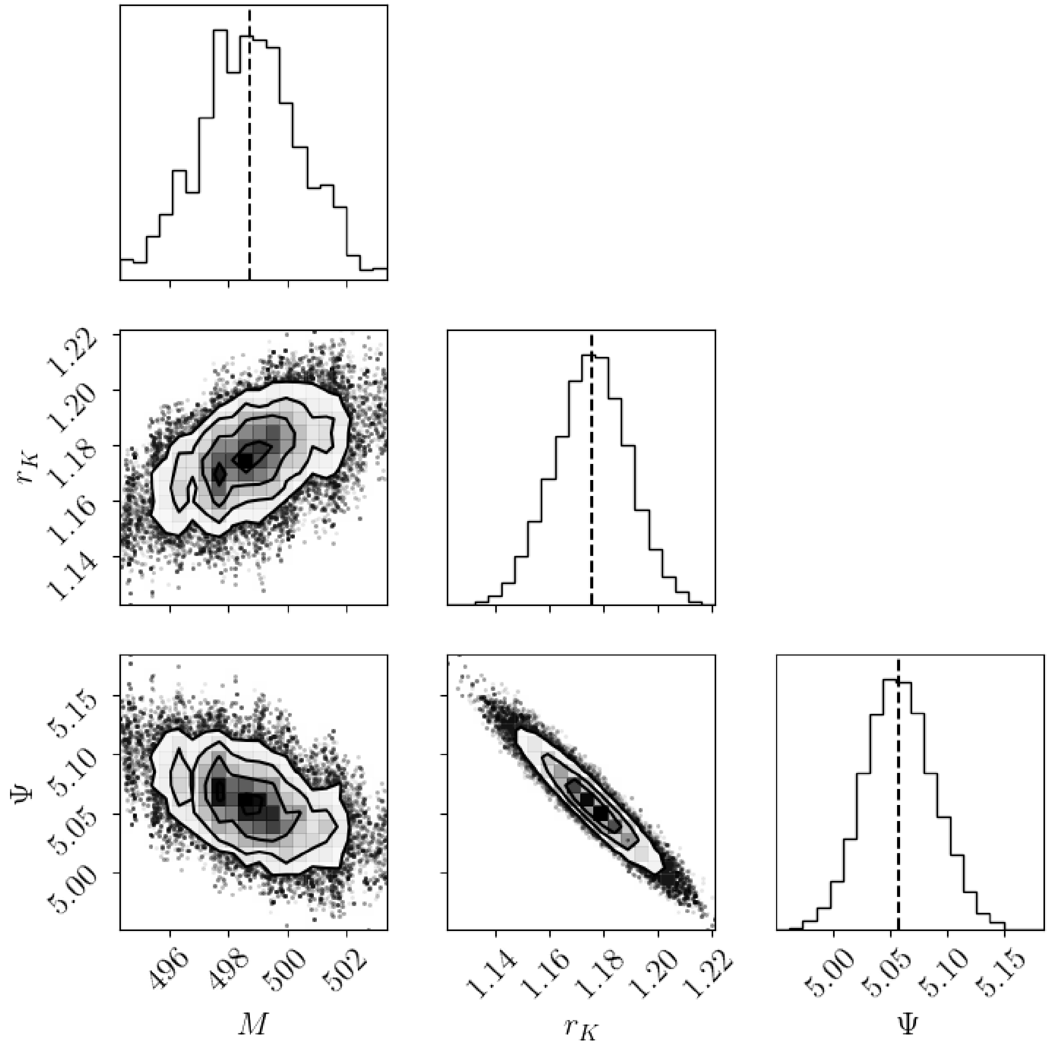

Figure 4.8: As Fig. 4.5, using a data set containing equal numbers of stars with three-, five-, and six-dimensional data as described in Sect. 4.5.

The extension to incomplete data is achieved by defining likelihood functions applicable to each missing data scenario. Starting with the full six-dimensional likelihood function (4.13), we marginalise over the missing data. Thus, the 5-d likelihood function is given by

$$l_{5d}(x, y, v_x, v_y, v_z) = 2 \int_0^{z_t} l_{6d}(x, y, z, v_x, v_y, v_z) \mathrm{d}z, \tag{4.44}$$

where $z_t = \sqrt{r_t^2 - x^2 - y^2}$ is the largest possible line-of-sight distance, given the truncation radius of the LoKi model, and the known (x, y) coordinates. The integral (4.44) must be performed numerically.

For the three-dimensional case, we obtain

$$l_{3d}(x, y, v_z) = 2\int_0^{z_t}\int_{-\infty}^{\infty}\int_{-\infty}^{\infty} l_{6\mathrm{d}}(x, y, z, v_x, v_y, v_z)\mathrm{d}v_x\mathrm{d}v_y\mathrm{d}z, \tag{4.45}$$

$$\equiv 2\int_0^{z_t} I\mathrm{d}z \tag{4.46}$$

To evaluate the inner two integrals, we define $v_\perp = \sqrt{v_x^2 + v_y^2}$. Now, due to the truncation in phase space, we have an upper limit on $v_\perp$ given by $\sqrt{\psi - v_z^2}$. The inner two integrals then become

$$I = 2\pi A e^{-aE_0}\int_0^{\sqrt{\psi - v_z^2}} v_\perp \left(e^{\psi - \frac{v_z^2}{2}} e^{-\frac{v_\perp^2}{2}} - 1\right)\mathrm{d}v_\perp, \tag{4.47}$$

$$= e^{\psi - \frac{v_z^2}{2}}\gamma\left(2, \psi - \frac{v_z^2}{2}\right), \tag{4.48}$$

where γ is the incomplete gamma function (Olver et al., 2022). Thus, the three-dimensional likelihood function is most compactly written as

$$l_{3d}(x, y, v_z) = \frac{4\pi A e^{-aE_0}}{M}\int_0^{z_t} e^{\psi - \frac{v_z^2}{2}}\gamma\left(2, \psi - \frac{v_z^2}{2}\right)\mathrm{d}z, \tag{4.49}$$

where again the remaining integral in z must be performed numerically.

The procedure for parameter inference using a data set X, which contains a mixture of incomplete data, consists in splitting the data set into three subsets, S_{3d}, S_{5d}, and S_{6d}. Each set contains only the stars with three-, five-, and six-dimensional data. The total log-likelihood of a given data set is then provided by

$$\ln l(X) = \sum_{s\in S_{3d}} \ln l_{3d}(s) + \sum_{s\in S_{5d}} \ln l_{5d}(s) + \sum_{s\in S_{6d}} \ln l_{6d}(s). \tag{4.50}$$

The parameter inference can then proceed in the same manner as Sect. 4.2. We apply this methodology to a test data set generated using the parameters $\{\Psi, r_K, M\} = \{5, 1.2, 500\}$. A discrete data set of stars containing full six-dimensional phase space data was generated using the procedure outlined in Sect. 4.1. To allow for the types of incomplete phase space information considered in this section we split this data set into three subsets, each containing a third of the total number of stars. For one of these subsets, we removed the line of sight distance from each star. For another subset, we removed both the line of sight distance and proper motion for each star. In the final subset, we retained all components of the phase space data. The resulting data set now contains an equal mix of three-, five-, and six-dimensional phase space data. We then used the inference process detailed in Sect. 4.3 with this mixed data set. The results are presented in Fig. 4.8. We note that the result is still satisfactory in this case.

4.6 Summary and discussion

In this chapter, we have discussed how we may exploit the large quantities of six-dimensional astrometric data, now available due to the Gaia satellite (Gaia Collaboration et al., 2016), for the task of fitting model parameters to data in a Bayesian framework. These methods allow us to avoid the task of binning the data, and work directly with the single-star data itself.

First, we have illustrated the potential of Bayesian inference in this context by fitting the parameters of King (1966) models to synthetic data via a direct calculation of the posterior distribution. We showed that, in this idealised situation, we can readily recover the input parameters from which the input data set is generated over a wide range of physically reasonable parameters representing a number of Galactic globular clusters.

We then presented a summary of the Metropolis-Hastings algorithm (see MacKay 2003 and Robert 2007). This is a Markov chain Monte Carlo method which allows us to approximate the posterior distribution on the model parameters in a high-dimensional parameter space, where a direct calculation of the posterior distribution is computationally intractable. Such is the case when we attempt to apply Bayesian inference methods to the LoKi models described in Chapt. 2. However, likely due to an inefficient choice of proposal density within the Metropolis-Hastings algorithm, none of the simulations that we have performed reached convergence when applied to these LoKi models. Metropolis-Hastings based methods for this model fitting remain promising, and future modifications to the utilised proposal density should then allow comparison to both more realistic synthetic data, as well as real astronomical data.

We concluded this chapter by detailing how the Bayesian methods discussed here may be extended to account for cases where full six-dimensional data is not available for a subset of the stars in the data set. Here we showed that it is still possible to accurately fit parameters to King (1966) models using synthetic input data containing subsets with only three-, or five-dimensional data.

Chapter 5

Conclusions and future work

5.1 Summary and conclusions

This thesis developed a set of tools necessary for the self-consistent dynamical modelling, and subsequent parameter inference, of stellar systems containing a central black hole.

In Chapt. 2, we presented a new family of spherically symmetric, isotropic stellar equilibria defined by a truncated isothermal distribution function in phase space. The effect of a central black hole was then accounted for via a modification of the boundary conditions for the resulting nonlinear Poisson equation. This equation was then solved numerically and the intrinsic properties of these models were described. Of particular note are the steep central gradients in density and velocity dispersion expected from a cluster harbouring a central black hole. For black hole masses that are close to the maximum black hole mass that a model can support, we noted the presence of a sharp transition in the structure of the equilibria between a branch of solutions where the black hole mass is subdominant to the cluster mass and a branch where the black hole mass is the dominant component of the system. This transitional behaviour was investigated using matched asymptotic expansions. As a result of these expansions, we identify three nested regimes of the parameter space that are required for a full description of this transitional behaviour. The interpretation of this transition as a first-order microcanonical phase transition is then supported via a thermodynamic characterisation of the models where we note the appearance of a new branch in the corresponding caloric curve when compared to the classical "cold spiral". A manuscript presenting this work is in preparation for submission to the journal Monthly Notices of the Royal Astronomical Society.

In Chapt. 3 we extended the LoKi models developed in Chapt. 2 to include the effect of rigid body internal rotation. These models are defined by a distribution function taking the same functional form as the LoKi models but with the relevant Jacobi integral as the argument, thus breaking the spherical symmetry. We detailed two methods of solution, one based upon a spectral iteration method, and one based upon matched asymptotic expansions. The resulting axisymmetric configurations were then characterised and their properties were compared to the equivalent rigidly rotating models which do not contain a central black hole. The eccentricity profiles of the Rotating LoKi models are largely similar to the models without a central black hole outside the central region ($\gtrapprox$ 40% of the cluster's extent). However, within the central region, we show that the addition of a central mass results in an increasingly spherical solution in this region. We also showed that the maximum rotation that can be sustained by the configurations is suppressed in the Rotating LoKi models, particularly in the case where the mass of the black hole is the dominant component of the mass of the system where the suppression is especially significant. This has a direct impact on the thermodynamical properties of these models where this non-uniform suppression of the allowable rotation strength, as a function of black hole mass, leads to a break in the caloric curve where a physical solution is no longer possible. A manuscript presenting this work is in preparation for submission to the journal Monthly Notices of the Royal Astronomical Society.

In Chapt. 4 we defined a Bayesian approach to the inference of model parameters for King (1966) models that exploits the increasingly available discrete single-star data containing all six dimensions of phase space information. This approach was applied to synthetic phase space data generated from King (1966) models, as well as the LoKi models constructed in Chapt. 2. We used physical parameters that emulate several Galactic globular clusters and showed that the inference process was successful at recovering the parameters used to generate the synthetic data. Initially, this method relies on a direct numerical calculation of the posterior probability density. Such a direct calculation is not always possible. For example, due to an increase in the dimension of the parameter space arising from the inclusion of further complexity (such as the addition of a central black hole). To address this issue we presented the use of the Metropolis-Hastings algorithm, a Markov chain Monte Carlo method that allows us to sample from the posterior probability density in cases where a direct calculation is impractical. This allowed us to approximate important quantities such as the posterior mean, and variance. We validated the use of this algorithm via application to the previously considered King (1966) models before attempting to extend it to the LoKi models. Unfortunately, application in this higher dimensional setting has proven ineffective thus far. We believe this to be a result of an inefficient choice of proposal density within the Metropolis-Haatings algorithm. We detail a possible method to address this issue in Sect. 5.2.

5.2 Future work

For each of the previous chapters, there are several outstanding issues or potential extensions that would form the basis of future work in this area. We outline some of them here.

5.2.1 Alternative classes of spherically symmetric distribution function

In this thesis, we have limited our attention to distribution functions defining truncated isothermal spheres. However, the method introduced in Chapt. 2 for the inclusion of a central black hole is not restricted solely to this class of distribution functions. In particular, a first step would be to consider a non-truncated model, such as a Plummer sphere (Plummer, 1911). It is not immediately obvious what the implications for a non-truncated model would be. Particularly, whether the transitional behaviour between a system in which the black hole mass is sub-dominant, to one where it dominates, would persist in this case.

There are also other physical properties, even in the spherically symmetric case, that may coexist with a central black hole. Immediately of interest would be the inclusion of radial anisotropy, a property observed in several Galactic globular clusters (see, e.g. Zocchi et al. 2017; Jindal et al. 2019), and for which a known degeneracy with a central mass exists (see, e.g. Ciotti 2021; Binney & Tremaine 2008), when considering central density and velocity dispersion gradients.

5.2.2 Differential rotation

In Chapt. 3, we consider only rigid body rotation, while current observational efforts have shown that globular clusters often exhibit differential rotation (see, e.g. Bianchini et al. 2018, and Vasiliev & Baumgardt 2021). Thus, there is a need to consider the presence of a central black hole and differential rotation together. This could be accomplished by defining a new distribution function accounting for differential rotation such as that employed in Varri & Bertin (2012) to describe a differentially rotating cluster with no central black hole. The methodology introduced in Chapt. 3 for the inclusion of a central black hole may then be used in this case, with particular attention to the spectral iterative method detailed in Sect. 3.3.

5.2.3 Alternative synthetic phase space data

In Sect. 4.1, the synthetic phase space data was generated directly from the distribution function for which we infer the parameters. This is a good first validation step, but we would like to investigate how the inference procedure detailed in Chapt. 4 performs when the synthetic data is generated via an alternative process.

We would first propose to generate the synthetic data as snapshots in time of an N-body simulation that has been allowed to evolve from its initial conditions and infer the parameters of the best-fit King (1966) model. It is not immediately obvious that the best-fit King (1966) model, obtained via the inference process detailed in Chapt. 4, should accurately represent these snapshots. Much previous work has been done fitting dynamical models of various types to snapshots of N-body simulations, highlighting the issues that may arise using single mass truncated isothermal spheres to fit this kind of data.

For example, in Sollima et al. (2015) they compare the fitting of single and multimass Michie-King models (Gunn & Griffin 1979) to synthetic N-body data. They show that fitting single-mass models can result in significant biases in total mass estimates, with over or underestimates being present depending on the state of evolution of the cluster. The multimass models generally perform well and were able to describe the density and velocity dispersion of the modelled cluster, provided that sufficient time has passed for the assumption of energy equipartition in the central region (see equation (5.3)) to be valid.

In Hénault-Brunet et al. (2019) they compare the fitting of 8 different classes of dynamical models (see Tab. 6 in Hénault-Brunet et al. 2019 for a summary) to synthetic data generated via an N-body simulation of M4 (Heggie 2014). Focusing on the single and multimass LIMEPY models (Gieles & Zocchi 2015) they recover similar results to those noted previously, i.e. that single mass models can be subject to biases in total mass and half mass radius. They also highlight the presence of potential escapers in N-body simulations. These cause an increase in the velocity dispersion profile in the outer regions of the cluster. Thus, using kinematic data covering the full radial extent of the cluster when using truncated isothermal sphere distribution functions which do not include this effect can lead to poor fits.

Both previously discussed papers perform their fits to $N-$body data using binned profiles. In Zocchi et al. (2016) a similar comparison is performed fitting single mass LIMEPY models to N-body data similarly using the discrete single-star data as in Chapt. 4. They note that the anisotropic models under consideration adequately reproduce the density, velocity anisotropy, and velocity dispersion profiles. The anisotropic models also perform considerably better than the isotropic King (1966) models that are also considered there. This highlights the importance of the extension to consider further kinematic complexity in the LoKi models.

Also, by construction, all of the synthetic data obtained via Sect. 4.1 is such that the set of parameters that generated the data belongs to the admissible parameter set Ω, defined in equation (4.19). Using N-body snapshots as the synthetic data it is then possible that the set of parameters best reproducing properties such as the total mass, density, or velocity dispersion would mean that a subset of the stars would have zero likelihood under those parameters. Such a situation could arise due to a close encounter producing a high-velocity star for example. This set of parameters is then inaccessible under the current inference setup, due to a single star in the sample. A possible solution to this problem, allowing a small subset of the stars that cannot be described under the best-fit parameters is proposed in Zocchi et al. (2016).

5.2.4 Multiple mass components

In this thesis, we have considered only single-mass systems where each star has the same mass, m. As noted in Sect. 5.2.3, this extension to account for multiple mass components may be done following classical methods (see, e.g., Michie 1963, Da Costa & Freeman 1976 and Gunn & Griffin 1979) by defining a global distribution function as a superposition of the distribution functions for each mass component. Let us consider the LoKi models of Chapt. 2 and suppose that we have components with individual masses $\{m_1, \ldots, m_k\}$, then the global distribution function, under the assumptions of spherical symmetry and isotropy in velocity space, would be defined as

$$f(r,v) = \sum_{i=1}^{k} C_i f_i(r,v), \tag{5.1}$$

where each f_k is a modification of the single component King (1966) distribution function (2.1) given by

$$f_i(r,v) = \begin{cases} e^{-a_k(E-E_0)} - 1, & E \leq E_0 \\ 0, & E > E_0. \end{cases} \tag{5.2}$$

The physical scales C_i relate to the overall phase space normalisation. The remaining physical scales, $a_i = 1/\sigma_i^2$, are velocity scales and are usually determined by assuming that the system is isothermal in the central region. Setting m_1 and σ_1^2 as reference physical scales, the remaining σ_i^2 then follow via considering energy equipartition as

$$m_i\sigma_i^2 = m_1\sigma_1^2. \tag{5.3}$$

However, Miocchi (2006) notes that this isothermal approximation can provide steeper velocity dispersion profiles and suppressed mass segregation when compared to adopting an energy equipartition criterion of the form

$$m_i\langle v_i^2\rangle = m_1\langle v_1^2\rangle. \tag{5.4}$$

Here $\langle v_i^2\rangle$ are the mean values of v_i^2 evaluated at the centre of the system using the non-isothermal distribution function (5.2).

An accurate representation of mass segregation is desirable when addressing the question of whether a central density or velocity gradient is due to an intermediate-mass black hole, or a system of stellar remnants that have migrated towards the centre of the system due to mass segregation (see, e.g. Zocchi et al. 2019, Baumgardt et al. 2019). Due to this consideration, we would seek to implement the energy equipartition criterion following equation (5.4).

5.2.5 Non-diagonal proposal covariances

In Chapt. 4, the primary outstanding item is finalising the extension of the Markov chain Monte Carlo methods described in Sect. 4.3 to the LoKi models constructed in Chapt. 2. The primary modification we would implement concerns the proposal density for the Metropolis-Hastings algorithm. We currently employ a diagonal covariance matrix for the Gaussian proposal density that we can tune relatively simply to obtain a reasonable acceptance rate (see App. F). Using a non-diagonal covariance matrix would allow us to account for the covariances that exist in the LoKi models, such as between μ and ϵ. This should allow a more efficient exploration of the parameter space. We would no longer be able to tune this covariance using the method used thus far. Instead, we would aim to implement an automatic tuning method. One such method: automated, finite adaptive-tuning (see Haario et al. 2001 and Roberts & Rosenthal 2009). This approach has been successfully applied to similar distribution function-based models (see Eadie et al. 2022) and presents the possibility of automatically tuning the relevant non-diagonal proposal density.

5.2.6 Influence of observational errors on Bayesian parameter inference

A further extension to the Markov chain Monte Carlo methods implemented in Chapt. 4 would be to include the effect of observational errors upon the inference process. This can be accomplished by modifying the likelihood function (4.13).

Initially, we would consider Gaussian errors on the components of the phase space data for each star, so that

$$\begin{aligned} r_i &\sim \mathcal{N}(r_i^*, \sigma_{r_i}^2), \\ v_i &\sim \mathcal{N}(v_i^*, \sigma_{v_i}^2), \end{aligned} \tag{5.5}$$

where (r_i, v_i) and $(\sigma_{r_i}^2, \sigma_{v_i}^2)$ denote the observed phase space coordinates and observational uncertainties. (r_i^*, v_i^*) then denotes the star's true radial position and velocity, which are unknown. Under the Gaussian assumption (5.5) we can define $P(r_i|r_i^*)$, i.e. the probability that we observe a radial position, r_i, given that the star is located at r_i^*. We can similarly define $P(v_i|v_i^*)$, the probability that a star is observed with a speed v_i, given that the true speed is v_i^*.

Now, we consider the true position and velocity of the star to be a random variable distributed according to a specified distribution function, and then the observed position and velocity as a random variable distributed according to equation (5.5). Then we can formulate the likelihood of observing the star at (r_i, v_i), under a given set of parameters, θ, as

$$l(r_i, v_i|\theta) = \iint P(r_i, v_i, r, v|\theta) \mathrm{d}^3\boldsymbol{r} \mathrm{d}^3\boldsymbol{v}, \tag{5.6}$$

where we have taken the joint distribution of the four random variables under consideration and marginalised over the unknown true position and velocity. This then simplifies to

$$l(r_i, v_i|\theta) = \iint P(r_i|r) P(v_i|v) P(r, v|\theta) \mathrm{d}^3\boldsymbol{r} \mathrm{d}^3\boldsymbol{v}. \tag{5.7}$$

This integral is defined over the whole volume of phase space accessible under the parameters θ. This integral must be calculated for each star in a given data set. This action significantly increases the computational requirements, as the Poisson equation (2.16) must be solved to obtain the $P(r, v|\theta)$ term in the integrand, an efficient method to approximate this integral is therefore needed to make use of this formulation.

5.2.7 Inference from observations in radially restricted domains

Finally, recall that in Sect. 4.5 we treat certain cases of incomplete data, limiting our consideration to the setting where certain components of phase space data are missing. Another possible scenario is that some phase space data may be missing altogether. In particular, we want to focus on the case where we only possess data in some limited radial range, $r \in [r_1, r_2]$. Such a setup allows us to answer questions about which observational strategy supplementing additional data may help us better constrain the model parameters inferred in Chapt. 4.

It is not immediately obvious how to approach such a scenario. A naive approach using the likelihood function (4.13) with a synthetic data set generated as in Sect. 4.1, but limited to a certain radial range produces highly biased results, failing to recover the true input parameters that generated the data.

We would propose to implement the methods outlined in Chapt. 8 of Gelman et al. (2013), and summarised here. This involves an explicit treatment for the data that potentially could be observed, but due to the data collection process is left unobserved. In our setting, this corresponds to stars that are generated outside of the region $r \in [r_1, r_2]$.

We begin with a dataset $X = \{\boldsymbol{x}_1, \ldots, \boldsymbol{x}_N\}$, where $\boldsymbol{x}_i = (r_i, v_i)$ represents the radial position and speed of an individual star, sampled according to Sect. 4.1 over the full radial extent of the cluster. We may then define a vector $I = \{I_1, \ldots, I_N\}$ such that $I_i = 0$, if the i^{th} star is unobserved, and $I_i = 1$ otherwise. This vector is the inclusion vector and allows us to model the collection of the data. We may thus split the full dataset into an observed component X_{obs}, which is known, and an unobserved component X_{mis} which is treated as unknown.

We may then define a complete-data likelihood as

$$l(X, I|\theta, \phi) = l(X|\theta) l(I|X, \phi), \tag{5.8}$$

where $l(X|\theta)$ is the now familiar likelihood of the full dataset under a set of parameters θ, and $l(I|X, \phi)$ is the term modelling the data collection process, dependent on a set of parameters ϕ (e.g. the radial bounds of the region we want to consider). However, we only have access to X_{obs}, so the appropriate likelihood of the observed data is given by marginalising over the unobserved data

$$l(X_{\text{obs}}, I|\theta, \phi) = \int l(X, I|\theta, \phi) \mathrm{d}X_{\text{mis}}. \tag{5.9}$$

The posterior distribution of the parameters is thus given by Bayes' theorem as

$$\begin{aligned} P(\theta, \phi|X_{\text{obs}}, I) &\propto P(\theta, \phi) \int l(X, I|\theta, \phi) \mathrm{d}X_{\text{mis}}, \\ &= P(\theta, \phi) \int l(X|\theta) l(I|X, \phi) \mathrm{d}X_{\text{mis}}, \end{aligned} \tag{5.10}$$

where in the second line we have substituted in equation (5.8), and $P(\theta, \phi)$ is the prior distribution on the parameters. Marginalising over ϕ then provides the posterior distribution on θ, the object of interest, as

$$P(\theta|X_{\text{obs}}, I) = P(\theta) \int \int P(\phi|\theta) l(X|\theta) l(I|X, \phi) \mathrm{d}X_{\text{mis}} \mathrm{d}\phi. \tag{5.11}$$

This posterior (5.11) treats the parameters determining the inclusion vector I in a very general way. When these parameters have a known value $\phi = \phi_0$, as is the case in our setup of observations within a fixed radial range, then equation (5.11) simplifies to provide

$$P(\theta|X_{\mathrm{obs}}, I) = P(\theta) \int l(X|\theta) l(I|X, \phi_0) \mathrm{d}X_{\mathrm{mis}}. \tag{5.12}$$

The main task is then the evaluation of the integral in equation (5.12), which would form the basis of this future work.

Appendix A

Asymptotic matching between regions I and II of Regime 2 for Loaded King models

We provide the details of the derivation (omitted in Sect. 2.5.2) of the values of the constants of integration that appear in the Region II solution, within Regime 2. Recall that $r_2 = \epsilon^2 r_1$. To perform the asymptotic match between regions I and II we use an intermediate region where both the large radius behaviour of region I and the small radius behaviour of region II are valid. This is satisfied by an intermediate variable $\eta = \epsilon r_1$, provided that $\eta = O(1)$.

By using this variable, we then match the large r_1 behaviour of the region I solution, provided by equation (2.36), and the small r_2 behaviour of the region II solution, which is provided by

$$\psi^{(\mathrm{II})} = \epsilon^2 \phi(r_2) = \epsilon^2(\phi_0(r_2) + \epsilon\phi_1(r_2)), \tag{A.1}$$

where

$$\phi_0(r_2) = c_0 + \frac{d_0}{r_2},$$
$$\phi_1(r_2) = e_0 + \frac{f_0}{r_2} + 4\kappa d_0^{5/2} r_2^{-1/2},$$

and c_0, d_0, e_0, f_0 are the constants of integration to be determined.

Now, the expansion of the region I solution in terms of the intermediate variable η gives

$$\psi^{(\mathrm{I})}(\eta) = \epsilon\frac{\Psi}{\eta} + \epsilon^2 a_2 + \epsilon^{5/2} 4\kappa \Psi^{5/2} \eta^{-1/2}, \tag{A.2}$$

while the expansion of equation (A.1) in the small r_2 limit gives

$$\psi^{(\mathrm{II})}(\eta) = \epsilon\frac{d_0}{\eta} + \epsilon^2\left(c_0 + \frac{f_0}{\eta}\right) + \epsilon^{5/2} 4\kappa d_0^{5/2} \eta^{-1/2} + \epsilon^3 e_0. \tag{A.3}$$

In this intermediate region, we must have that both equations (A.2) and (A.3) are valid. From this condition, we then read off that

$$c_0 = a_2, \quad d_0 = \Psi, \quad e_0 = 0, \quad \text{and } f_0 = 0, \tag{A.4}$$

i.e. the constants of integration required when considering the Region II solution are fully specified.

Appendix B

Numerical solver (`LoKi`)

B.1 General implementation of the Poisson solver

We provide a Python code which solves equation (2.16) and outputs a selection of intrinsic, projected, and global properties of the models discussed in Chapt. 2. The code also provides the relevant asymptotic solutions to the problem in Regimes 1-3, in the case of a King (1966) distribution function. As discussed in Sect. 2.9, the required scaling conditions for the Prendergast & Tomer (1970b) and Wilson (1975) models are expected to differ from those presented in the main body, but the numerical solver of equation (2.16) can be easily adapted. The "Loaded King" (LoKi) code is publicly available at https://github.com/Sbonsor/LoKi.

The output of the code is provided in the dimensionless units described in Sect. 2.2. However, for convenience, a function is included to scale the output to Hénon units (Heggie & Mathieu, 1986).

The Poisson equation is solved via the "rk45" routine provided in the SciPy (Virtanen et al., 2020a) sub-package integrate. This routine is an explicit Runge-Kutta scheme of order 4(5) using the Dormand-Prince pair of formulas (Dormand & Prince, 1980). As a baseline, the integration provides the values of ψ, and $\mathrm{d}\psi/\mathrm{d}r$ as a function of dimensionless radius. Optionally, the user can also return the mass, and potential energy directly as a result of the integration of the Poisson equation (i.e., see equations (2.19) and (2.72)).

Finally, we provide functions to return the asymptotic approximations to the solution in each of the three regimes described in Chapt. 2, by using, also in this case, the "rk45" routine for the solution of the relevant approximate equations.

B.2 Discrete sampling of the distribution function for N-body simulations

To facilitate numerical applications, we provide a function to generate a set of discrete samples from any given equilibrium generated by the LoKi code detailed in B.1. This function takes as input an object containing the model computed by the Poisson solver, the number of samples required, and whether to scale the resulting positions, velocities and masses to Hénon units. The result is then a dictionary containing the three components of the position vector, three components of the velocity vector, and the mass of each particle.

In this thesis, we have considered only single-mass models, so the mass of each particle is set to M_C/N, where N is the number of samples.

For each particle we obtain the vector $(\hat{x}, \hat{y}, \hat{z}, \hat{v}_x, \hat{v}_y, \hat{v}_z)$ according to the procedure laid out in Sect. 4.1. These values can then be scaled to Hénon units via the provided function, which multiplies the output by the scaling constants r_K, $1/\sqrt{a}$, and $1/M_C$ for positions, velocities and masses.

Appendix C

Spectral iteration scheme for Rotating Loaded King models (`RLoKi`)

Here we provide the details of the application of the method of variation of arbitrary constants to obtain equations (3.21) and (3.22). We then consider some important points for the numerical calculation of these solutions.

C.1 Variation of an arbitrary constant

The initial value problem for $l = 0$ is given by

$$\left(\frac{\mathrm{d}^2}{\mathrm{d}r^2} + \frac{2}{r}\frac{\mathrm{d}}{\mathrm{d}r}\right) u_0^{(n)}(r) = -9\frac{\rho_0^{(n-1)}(r)}{\rho(\Psi)} \equiv b_0(r), \tag{C.1}$$

$$u_0^{(n)}(r) = \Psi - \frac{9\mu}{4\pi\varepsilon}, \tag{C.2}$$

$$u_0^{(n)\prime}(0) = 0, \tag{C.3}$$

$$u_0^{(n)}(r) \to aH_0 \text{ as } r \to \infty \tag{C.4}$$

The two homogeneous solutions corresponding to equation (C.1) are given by $y_1(r) = r^0$ and $y_2(r) = r^{-1}$. We then look for a particular solution to equation (C.1) in the form

$$u_p(r) = c_1(r)y_1(r) + c_2(r)y_2(r), \tag{C.5}$$

subject to the requirement that

$$c_1'(r)y_1(r) + c_2'(r)y_2(r) = 0. \tag{C.6}$$

Substituting equation (C.5) into equation (C.1), and using equation (C.6), then provides that

$$c_1'(r)y_1'(r) + c_2'(r)y_2'(r) = b(r). \tag{C.7}$$

The equations (C.6) and (C.7) thus form a linear system of equations for c_1' and c_2' that may be solved using Cramer's rule to yield

$$c_1'(r) = r b_0(r) = -\frac{9}{\hat{\rho}(\Psi)} r \rho_0^{(n-1)}(r), \tag{C.8}$$

$$c_2'(r) = -b_0(r) r^2 = \frac{9}{\hat{\rho}(\Psi)} r^2 \rho_0^{(n-1)}(r). \tag{C.9}$$

We may then integrate these equations from the origin to provide

$$c_1(r) = -\frac{9}{\hat{\rho}(\Psi)} \int_0^r s \rho_0^{(n-1)}(s) \mathrm{d}s, \tag{C.10}$$

$$c_2(r) = \frac{9}{\hat{\rho}(\Psi)} \int_0^r s^2 \rho_0^{(n-1)}(s) \mathrm{d}s. \tag{C.11}$$

Solutions to equation (C.1) thus take the form

$$u_0^{(n)}(r) = A_0 + \frac{B_0}{r} - \frac{9}{\hat{\rho}(\Psi)} \left[\int_0^r s \rho_0^{(n-1)}(s) \mathrm{d}s - \frac{1}{r} \int_0^r s^2 \rho_0^{(n-1)}(s) \mathrm{d}s \right], \tag{C.12}$$

where A_0, B_0 are free constants to be determined. Using the boundary condition (C.2) then provides that $B_0 = 0$ and $A_0 = \Psi - 9\mu/(4\pi\epsilon)$. The conditions (C.3) and (C.4) are then satisfied automatically by the resulting expression. As a consequence by equation (C.4) we also have that

$$\begin{aligned} aH_0 &= \lim_{n\to\infty} \left(\Psi - \frac{9\mu}{4\pi\epsilon} - \frac{9}{\hat{\rho}(\Psi)} \int_0^\infty s \rho_0^{(n-1)}(s) \mathrm{d}s \right), \\ &= \lim_{n\to\infty} \left(\Psi - \frac{9\mu}{4\pi\epsilon} - \frac{9}{\hat{\rho}(\Psi)} \int_\epsilon^{r_t} s \rho_0^{(n-1)}(s) \mathrm{d}s \right), \end{aligned} \tag{C.13}$$

where we recall that $\rho_0 = 0$ interior to $r = \epsilon$, and outside of $r = r_t$.

For $l > 0$ we have that

$$\left(\frac{\mathrm{d}^2}{\mathrm{d}r^2} + \frac{2}{r}\frac{\mathrm{d}}{\mathrm{d}r} + \frac{l(l+1)}{r^2} \right) u_l^{(n)}(r) = -9 \frac{\rho_l^{(n-1)}(r)}{\rho(\Psi)} \equiv b_l(r), \tag{C.14}$$

$$u_l^{(n)}(r) = 0, \tag{C.15}$$

$$u_l^{(n)\prime}(0) = 0, \tag{C.16}$$

$$u_l^{(n)}(r) \to 0 \text{ as } r \to \infty \tag{C.17}$$

The homogeneous solutions corresponding to equation (C.14) are of the form $y_1(r) = r^l$ and $y_2(r) = r^{1+l}$. The method of variation of arbitrary constants then similarly provides that

$$u_l^{(n)}(r) = A_l r^l + \frac{B_l}{r^{1+l}} - \frac{9}{(2l+1)\hat{\rho}(\Upsilon)} \left[r^l \int_0^r s^{1-l} \rho_l^{(n-1)}(s) \mathrm{d}s \right.$$
$$\left. - \frac{1}{r^{1+l}} \int_0^r s^{l+2} \mathrm{d}s \right]. \qquad \text{(C.18)}$$

We then have two free constants for each value of l to be determined by the boundary conditions. By the boundary condition (C.17) we know that $u_l^{(n)}$ must not diverge as $r \to \infty$. This consideration yields that

$$A_l = \frac{9}{(2l+1)\hat{\rho}(\Upsilon)} \int_0^\infty s^{1-l} \rho_l^{(n-1)}(s) \mathrm{d}s. \qquad \text{(C.19)}$$

We must then have that $B_l = 0$ to obey the boundary condition (C.15). The boundary condition (C.16) is then automatically satisfied as the only remaining terms are of the form r^l.

Substituting the free constants A_l, B_l, for $l \geq 0$ into the solutions (C.12) and (C.18) then recovers equations (3.21) and (3.22) once we note that the density $\hat{\rho}$ is defined to be zero interior to $r = \epsilon$ and so the lower limit on the above integrals may be replaced by ϵ.

C.2 Notes on numerical implementation

During each iteration, we must calculate the integrals in equations (3.21) and (3.22). To this end, a radial grid is defined in two parts. First, a grid encompassing $[\epsilon, r_t]$ is generated via the LoKi code (see Chapt. 2 for details) which is sufficiently fine in the central region to capture the expected steep central density gradients. We then append a second part to the grid containing points in $[r_t, 2r_t]$ with a grid spacing inherited from the outermost points of the LoKi-generated grid. This allows for the extension of the rotating model compared to the LoKi model as the rotating model will have a radial extent on the equatorial plane of approximately $3r_t/2$.

We must then decompose the density profile from the previous iteration into Legendre polynomials. This is accomplished using a fast Legendre transform python package (Tessore, 2022). This is a discrete Legendre transform based on the use of discrete cosine transforms as detailed in Alpert & Rokhlin (1991). We also introduce a threshold, t. Any coefficient with a magnitude lower than this value is set to zero. This prevents the numerical noise arising in the transform from being amplified at small radii due to the r^{-l-1} terms, and at large radii for the r^l terms in equation (3.22). To illustrate this we show in Fig. C.1 the result of applying the discrete Legendre transform to the purely spherical model produced via the LoKi code (see Chapt. 2). The expected theoretical result is that coefficients with $l \neq 0$ are zero. However, we can see the small amplitude numerical noise that necessitates this thresholding procedure. In practice, the level at which this threshold is set depends on the maximum order of Legendre

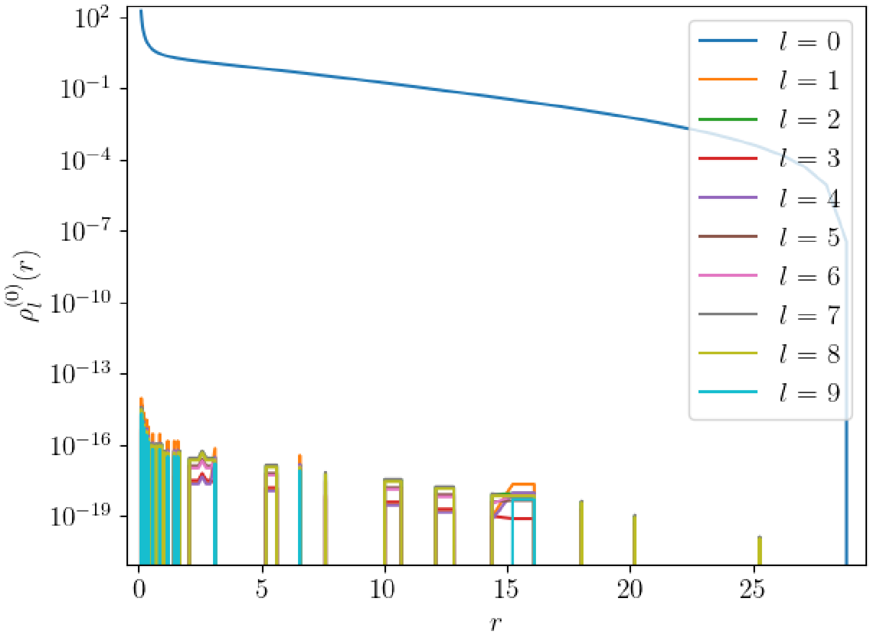

Figure C.1: Magnitudes of the Legendre coefficients, as a function of radius, for the spherical density profile of LoKi model (see Chapt. 2) with $\{\Psi, \mu, \epsilon\} = \{5, 0.5, 0.1\}$. The coefficients are calculated using the discrete Legendre transform function provided in Tessore (2022).

polynomial in use as a higher l_{max} provides greater amplification of this noise. We set $t = 10^{-10}$ after testing when this effect prevents convergence of the scheme for $l_{\text{max}} = 9$.

The integrals in equations (3.21) and (3.22) were then performed via a Simpson's rule integration as implemented in Scipy (Virtanen et al., 2020b).

The scheme was deemed to converge when the maximum relative change in ψ between iterations was below a certain tolerance, ψ_{tol}. In this case, we chose a very stringent tolerance of $\psi_{\text{tol}} = 10^{-3}$ so that our stopping condition is

$$\frac{\psi^{(n)}(r, \theta) - \psi^{(n-1)}(r, \theta)}{\psi^{(n-1)}(r, \theta)} < \psi_{\text{tol}}. \tag{C.20}$$

The "Rotating Loaded King" (RLoKi) code is publicly available at
https://github.com/Sbonsor/RLoKi

Appendix D

Asymptotic matching to first-order for Rotating Loaded King models

We begin by expanding the interior and exterior solutions in a Taylor series around the truncation radius $r = r_t$, up to third-order

$$\begin{aligned}\psi^{(\mathrm{int})}(r,\theta) = {} & \psi_0^{(\mathrm{int})}(r_t) - \psi^{(\mathrm{int})\prime}(r_t)(r_t - r) \\ & + \frac{1}{2}\psi_0^{\prime\prime(\mathrm{int})}(r_t)(r_t - r)^2 - \frac{1}{3!}\psi_0^{(\mathrm{int})\prime\prime\prime}(r_t)(r_t - r)^3 \\ & + \chi \left[\psi_1^{(\mathrm{int})}(r_t,\theta) - \frac{\partial \psi_1^{(\mathrm{int})}(r_t,\theta)}{\partial r}(r_t - r) \right. \\ & \left. + \frac{1}{2}\frac{\partial^2 \psi_1^{(\mathrm{int})}(r_t,\theta)}{\partial r^2}(r_t - r)^2 \right] + \frac{1}{2}\chi^2 \left[\psi_2^{(\mathrm{int})}(r_t,\theta) \right. \\ & \left. - \frac{\partial \psi_2^{(\mathrm{int})}(r_t,\theta)}{\partial r}(r_t - r) \right] + \frac{1}{3!}\chi^3 \psi_3^{(\mathrm{int})}(r_t,\theta). \end{aligned} \tag{D.1}$$

The same expression holds with (int) exchanged for (ext).

We now express the layer solution in non-scaled coordinates

$$\begin{aligned}\psi^{(\mathrm{lay})}(r,\theta) & = \chi\tau(r,\theta), \\ & = F_0(\theta)(r_t - r) + \frac{F_0(\theta)}{r_t}(r_t - r)^2 + \left(\frac{F_0(\theta)}{r_t^2} \right. \\ & \left. - \frac{1}{6r_t}\Lambda^2 F_0(\theta) \right)(r_t - r)^3 + \chi \left[G_0(\theta) + F_1(\theta)(r_t - r) \right. \\ & \left. + \left(\frac{F_1(\theta)}{r_t} + 9 - \frac{1}{2r_t^2}\Lambda^2 G_0(\theta) \right)(r_t - r)^2 \right] \\ & + \chi^2 \left[G_1(\theta) + \frac{1}{2}F_2(\theta)(r_t - r)^2 \right] + \chi^3 \frac{1}{2} G_2(\theta). \end{aligned} \tag{D.2}$$

The equations (D.1) and (D.2) may then be compared order by order, in both χ

and $(r_t - r)$, to obtain the relations (3.48), as well as the relations involving the higher order terms given by

$$\psi_2^{(\text{int})}(r_t,\theta) = G_1(\theta) = \psi_2^{(\text{ext})}(r_t,\theta), \tag{D.3}$$

$$-\frac{\partial\psi_2^{(\text{int})}(r_t,\theta)}{\partial r} = F_2(\theta) \;= -\frac{\partial\psi_2^{(\text{ext})}(r_t,\theta)}{\partial r}, \tag{D.4}$$

$$\psi_3^{(\text{int})}(r_t,\theta) = G_2(\theta) = \psi_3^{(\text{ext})}(r_t,\theta). \tag{D.5}$$

We must go up to this order, even though these constants do not appear in the first-order solution. The condition stated at equation (D.5) illustrates the need to consider terms up to third order in the exterior/interior solution to have a closed system of equations.

Now we can use the expressions for the interior and exterior solutions at each order of χ to determine the values of the free constants.

At $O(1)$, we have

$$\psi_0^{(\text{int})}(r) = u_0^{(\text{int})}(r) + \frac{9\mu}{4\pi r},$$

via equation (3.25a), and

$$\psi_0^{(\text{ext})}(r) = \alpha_0 - \frac{\lambda_0}{r}.$$

Then, utilising equations (3.48a) and (3.48b), we obtain that

$$\lambda_0 = r_t^2\psi_0^{(\text{int})\prime}(r_t), \tag{D.6}$$

$$\alpha_0 = r_t\psi_0^{(\text{int})\prime}(r_t). \tag{D.7}$$

At $O(\chi)$, we have

$$\psi_1^{(\text{int})}(r,\theta) = u_{1,0}(r) + \sum_{l=1}^{\infty} A_l\gamma_l(r)\mathrm{P}_l(\cos\theta),$$

where $u_{1,0}$ is calculated via equation (3.30a), and each γ_l is obtained via equation (3.31a). We also have

$$\psi_1(^{(\text{ext})}(r) = \alpha_1 - \frac{\lambda_1}{r} + C_0(r) - \sum_{l=1}^{\infty}\left[\frac{a_l}{r^{l+1}} - C_l(r)\right]\mathrm{P}_l(\cos\theta).$$

Then, we may use equations (3.48c) and (3.48d), considering each order in the Legendre series in succession.

At $l = 0$, this results in reading off

$$\lambda_1 = u_{1,0}'(r_t)r_t^2 - C_0'(r_t)r_t^2, \tag{D.8}$$

$$\alpha_1 = u_{1,0}(r_t) + \frac{\lambda_1}{r_t} - C_0(r_t). \tag{D.9}$$

For $l > 0$, we obtain, for each l, that

$$A_l \gamma_l(r_t) = -\frac{a_l}{r_t^{l+1}} + C_l(r_t), \tag{D.10}$$

$$-A_l \gamma_l'(r_t) = -\frac{(l+1)a_l}{r_t^{l+1}} - C_l'(r_t). \tag{D.11}$$

This is a linear system of equations for A_l, a_l for each l, and it may be written as

$$\boldsymbol{M}\boldsymbol{u} = \boldsymbol{v}, \tag{D.12}$$

where

$$\boldsymbol{M} = \begin{pmatrix} \gamma_l(r_t) & r_t^{-(l+1)} \\ -r_t \gamma_l'(r_t) & (l+1) r_t^{-(l+1)} \end{pmatrix}, \tag{D.13}$$

$$\boldsymbol{u} = \begin{pmatrix} A_l \\ a_l \end{pmatrix}, \tag{D.14}$$

$$\boldsymbol{v} = C_l(r_t) \begin{pmatrix} 1 \\ -2 \end{pmatrix}. \tag{D.15}$$

$$\tag{D.16}$$

Now, for $l = 2$ we have $C_2(r_t) = -3r_t^2$ and the solution to the linear system (D.12) is easily obtained as

$$A_2 = \frac{5C_2(r_t)}{r_t \gamma_2'(r_t) + 3\gamma_2(r_t)}, \tag{D.17}$$

$$a_2 = -r_t^3 [A_2 \gamma_2(r_t) - C_2(r_t)]. \tag{D.18}$$

For $l > 2$, we have $C_l(r_t) = 0$. This, along with the fact that $\det(\boldsymbol{M}) \neq 0$ (Bertin & Varri 2008), provides finally that $A_l = a_l = 0$ for $l > 2$. This conclusion specifies all free constants present in the first-order solution. However, this process may be continued for the higher order corrections in equations (D.3)-(D.5), to complete the matching procedure.

Appendix E

Validation of synthetic phase space data generation

We validate the synthetic phase space data obtained via the procedure described in Sect. 4.1 by comparison of selected intrinsic properties, as well as global properties, between a given discrete data set and the theoretically expected result.

We define a linearly spaced radial grid, r_j, that covers the radial extent of the cluster. We then consider spherical shells centred at r_j, each of a thickness equal to the radial spacing, dr. The number density associated with a given shell, ρ_j, is then given by the ratio of the number of stars located in the shell, n_j, to the volume of that shell.

$$\rho_j = \frac{n_j}{4\pi r_j^2 \mathrm{d}r} \tag{E.1}$$

This may then be normalised to the central number density provided by

$$\rho_0 = \frac{n_0}{\frac{4}{3}\pi r_0^2}, \tag{E.2}$$

where n_0 is the number of stars located within a sphere of radius r_0, centred at the origin.

We show the result of this procedure for a King (1966) model with central concentration $\Psi = 6$, compared to the theoretical result obtained via equation (2.3), in Fig. E.1.

We may also perform a similar procedure to test the pressure profile, with the radial component of the pressure tensor associated with a given spherical shell being calculated as

$$P_{r,j} = \frac{\rho_j}{n_j} \sum_i v_{r,i}^2, \tag{E.3}$$

where the summation is taken over all stars located within the j^{th} spherical shell. We, again, normalise this profile using a central value obtained by considering

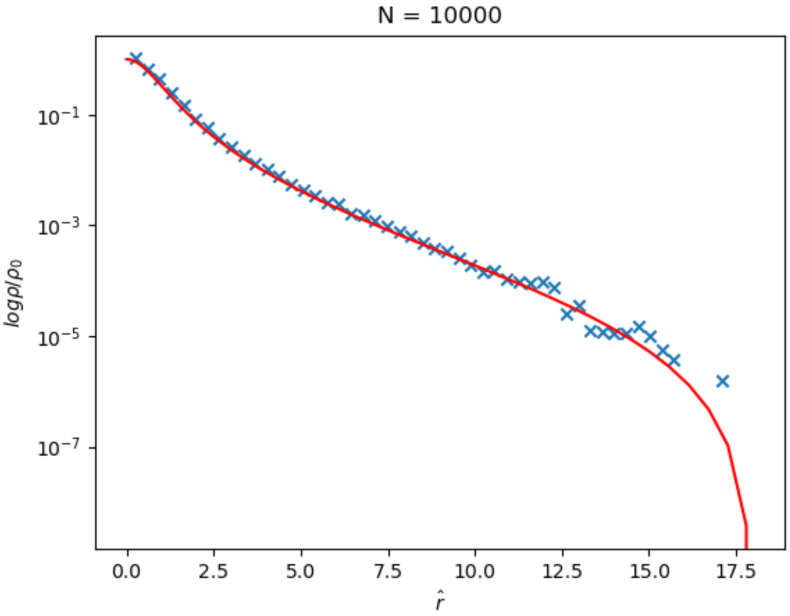

Figure E.1: Intrinsic density profile for a King (1966) model with central concentration $\Psi = 6$. Obtained by considering the number of stars located in successive radial shells in a data set with $N = 10000$ stars sampled according to Sect. 4.1 (blue crosses), and the theoretical result via the numerical solution of equation (2.16).

the same sphere of radius r_0, centred at the origin, to give

$$P_{r,0} = \frac{\rho_0}{n_0} \sum_i v_{r,i}^2. \tag{E.4}$$

We recall that the King (1966) model is isotropic, thus the other components of the pressure tensor are expected to be equal to the radial component presented here and they may be calculated in the same manner.

The comparison between this empirical pressure profile and the theoretical result from equation (2.4) is illustrated in Fig. E.2.

For both density and pressure profiles, we observe good agreement between the empirical and theoretical results, with the expected Poisson noise about the theoretical results being larger in the more sparsely sampled, low-density, outer regions of the domain of the model.

The models that we consider are equilibrium models and therefore the scalar Virial theorem (Heggie & Hut, 2003) states that

$$2T + W = 0, \tag{E.5}$$

where T is the total kinetic energy of the system, and W is the total gravitational potential energy of the system. Given our discrete data set, we can then calculate

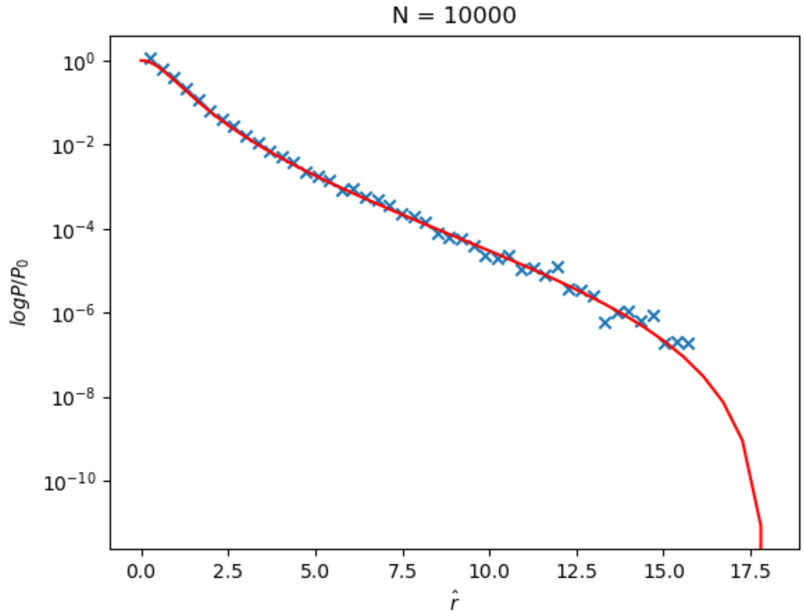

Figure E.2: Intrinsic pressure profile for a King (1966) model with central concentration $\Psi = 6$. The data are obtained by considering the number of stars located in successive radial shells in a data set with $N = 10000$ stars sampled according to Sect. 4.1 (blue crosses), and the theoretical result via the numerical solution of equation (2.16).

these quantities as

$$T = \frac{1}{2}\sum_{i=1}^{N} m(v_{xi}^2 + v_{yi}^2 + v_{zi}^2), \tag{E.6}$$

where $m = M/N$ is the mass of an individual star in the sample, and

$$W = \sum_{i=1}^{N}\sum_{j>i} -\frac{Gm^2}{|\boldsymbol{r}_i - \boldsymbol{r}_j|}. \tag{E.7}$$

We can then examine the ratio

$$Q_{\rm vir} = -\frac{W}{T}, \tag{E.8}$$

where we expect a result of $Q_{\rm vir} = 0.5$ for an equilibrium system, with fluctuations due to the Poisson noise arising from the discrete nature of the sample. To validate this aspect of the synthetic data, we generate multiple synthetic data sets for the adopted King (1966) test model with parameters $\{\Psi, r_K, M\} = \{5, 1.2, 500\}$, and varying numbers of stars between $N = 10^3$ and $N = 10^5$. We then calculate the virial ratio for each of these generated data sets. This procedure is repeated 10 times per value of N, to illustrate the scatter about $Q_{\rm vir} = 0.5$. The results of this process are illustrated in Fig. E.3.

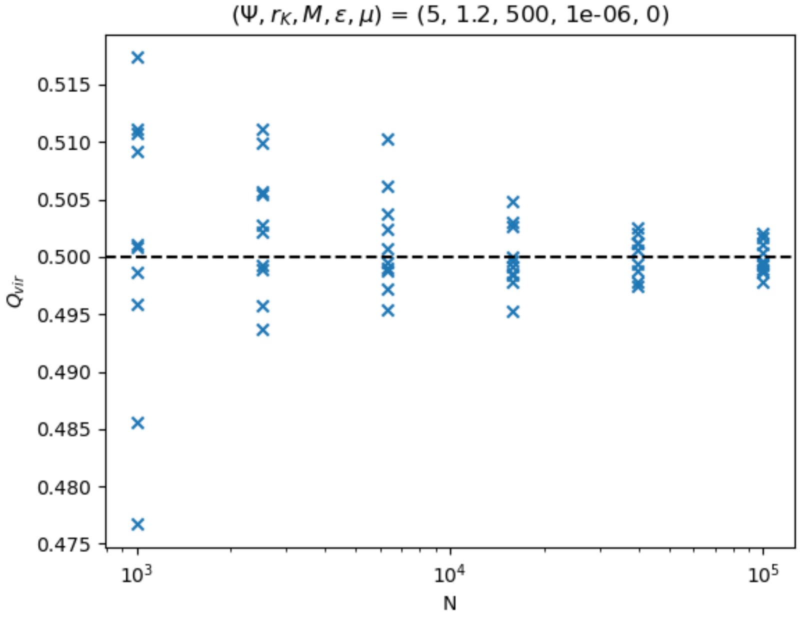

Figure E.3: Virial ratios calculated for individual synthetic data sets generated from a King (1966) model with parameters $\{\Psi, r_K, M\} = \{5, 1.2, 500\}$, varying the number of stars, N. The theoretical value of $Q_{\rm vir} = 0.5$ is indicated by the black dashed line.

Appendix F

Metropolis-Hastings algorithm proposal distribution tuning

In Sect. 4.3.1, we introduce a proposal density (4.29)

$$\theta' | \theta^{(n)} \sim \mathcal{N}(\theta^{(n)}, \beta \boldsymbol{C}).$$

The diagonal elements of $\boldsymbol{C}$ are chosen such that the relative size of a step in each of the three parameters is similar. This consideration is important, as it allows us to explore the parameter space efficiently by allowing larger steps for the parameters with large magnitudes (e.g. M), and smaller steps for those with small magnitudes (e.g. r_K).

In practice, we accomplish this by evaluating the likelihood (4.14) on a coarse discretisation of the parameter space. The values of the maximum likelihood parameters on this coarse grid are then used to set the diagonal elements of $\boldsymbol{C}$.

The constant β allows us to tune the overall rate at which proposed moves are accepted or rejected. If the acceptance rate is too low, then the sampling is inefficient as the chain will only rarely accept a proposal, wasting too many proposals on unlikely moves. Conversely, if the rate is too high, then only small moves are performed and the exploration of the parameter space is slow. The constant β is, therefore, tuned to achieve an acceptance rate similar to the optimal acceptance rate for a Gaussian proposal density, calculated in Gelman et al. (1997) as 23.4%. There are several ways to perform this tuning, as well as adaptive methods to automatically tune the proposal density (see, e.g. Haario et al. 2001).

Since we use a fixed proposal density, we define a target acceptance rate, R_0, and an initial value, $\beta = \beta_0$. We then run the Metropolis-Hastings algorithm to obtain the acceptance rate associated with that value of beta, R_β. We then update β via

$$\beta_n = \beta_{n-1} \frac{R_{\beta_n - 1}}{R_0}. \tag{F.1}$$

This ensures that the step size increases if the acceptance rate is too high, and decreases if the acceptance rate is too low. This process is then repeated until the acceptance rate is within some tolerance of the target acceptance rate, R_0. In our case we set a tolerance of 0.02.

Bibliography

Aarseth S. J., 2003, Gravitational N-Body Simulations: Tools and Algorithms. Cambridge University Press, Cambridge, UK

Abbott R., et al., 2020, Phys. Rev. Lett., 125, 101102

Alpert B. K., Rokhlin V., 1991, SIAM Journal on Scientific and Statistical Computing, 12, 158

An J. H., Evans N. W., 2006, ApJ, 642, 752

Anderson J., King I. R., 2003, AJ, 126, 772

Aros F. I., Vesperini E., 2023, MNRAS, 525, 3136

Aros F. I., Sippel A. C., Mastrobuono-Battisti A., Askar A., Bianchini P., van de Ven G., 2020, MNRAS, 499, 4646

Bahcall J. N., Wolf R. A., 1977, ApJ, 216, 883

Ball W. H., Tout C. A., Żytkow A. N., Eldridge J. J., 2011, MNRAS, 414, 2751

Baumgardt H., Makino J., 2003, MNRAS, 340, 227

Baumgardt H., et al., 2019, MNRAS, 488, 5340

Begelman M. C., Rossi E. M., Armitage P. J., 2008, MNRAS, 387, 1649

Bellini A., et al., 2015, ApJ, 810, L13

Bellini A., Bianchini P., Varri A. L., Anderson J., Piotto G., van der Marel R. P., Vesperini E., Watkins L. L., 2017, ApJ, 844, 167

Bender C., Orszag S., 1999, Advanced Mathematical Methods for Scientists and Engineers: Asymptotic Methods and Perturbation Theory. Springer, New York, NY, USA

Bertin G., Stiavelli M., 1984, A&A, 137, 26

Bertin G., Varri A. L., 2008, ApJ, 689, 1005

Bianchini P., Varri A. L., Bertin G., Zocchi A., 2013, ApJ, 772, 67

Bianchini P., van der Marel R. P., del Pino A., Watkins L. L., Bellini A., Fardal M. A., Libralato M., Sills A., 2018, MNRAS, 481, 2125

Bianchini P., Ibata R., Famaey B., 2019, ApJ, 887, L12

Binney J., Tremaine S., 2008, Galactic Dynamics: Second Edition. Princeton Series in Astrophysics, Princeton University Press

Breen P. G., Heggie D. C., 2013, MNRAS, 432, 2779

Breen P. G., Varri A. L., Heggie D. C., 2017, MNRAS, 471, 2778

Cappellari M., 2008, MNRAS, 390, 71

Cappellari M., 2020, MNRAS, 494, 4819

Chandrasekhar S., 1933, MNRAS, 93, 390

Chavanis P.-H., Lemou M., Méhats F., 2015a, Phys. Rev. D, 91, 063531

Chavanis P.-H., Lemou M., Méhats F., 2015b, Phys. Rev. D, 92, 123527

Ciotti L., 2021, Introduction to Stellar Dynamics. Cambridge University Press

Ciotti L., Morganti L., 2009, MNRAS, 393, 179

Ciotti L., Morganti L., 2010a, MNRAS, 401, 1091

Ciotti L., Morganti L., 2010b, in Bertin G., de Luca F., Lodato G., Pozzoli R., Romé M., eds, American Institute of Physics Conference Series Vol. 1242, Plasmas in the Laboratory and the Universe: Interactions, Patterns, and Turbulence. AIP, pp 300–305

Ciotti L., Ziaee Lorzad A., 2018, MNRAS, 473, 5476

Ciotti L., Mancino A., Pellegrini S., Ziaee Lorzad A., 2021, MNRAS, 500, 1054

Cipollina M., Bertin G., 1994, A&A, 288, 43

Cordoni G., Milone A. P., Mastrobuono-Battisti A., Marino A. F., Lagioia E. P., Tailo M., Baumgardt H., Hilker M., 2020, ApJ, 889, 18

Da Costa G. S., Freeman K. C., 1976, ApJ, 206, 128

Davoust E., 1977, A&A, 61, 391

Dehnen W., 1993, MNRAS, 265, 250

Dejonghe H., 1987, MNRAS, 224, 13

Dickson N., Smith P. J., Hénault-Brunet V., Gieles M., Baumgardt H., 2024, MNRAS, 529, 331

Djorgovski S., Meylan G., 1994, AJ, 108, 1292

Dormand J., Prince P., 1980, Journal of Computational and Applied Mathematics, 6, 19

Eadie G. M., Webb J. J., Rosenthal J. S., 2022, ApJ, 926, 211

Einsel C., Spurzem R., 1999, MNRAS, 302, 81

Favata M., Hughes S. A., Holz D. E., 2004, ApJ, 607, L5

Ferraro F. R., et al., 2018, ApJ, 860, 50

Fujii M. S., Wang L., Tanikawa A., Hirai Y., Saitoh T. R., 2024, Science, 384, 1488

Gaia Collaboration et al., 2016, A&A, 595, A1

Gaia Collaboration et al., 2023, A&A, 674, A1

Gelman A., Rubin D. B., 1992, Statistical Science, 7, 457

Gelman A., Gilks W. R., Roberts G. O., 1997, The Annals of Applied Probability, 7, 110

Gelman A., Carlin J., Stern H., Dunson D., Vehtari A., Rubin D., 2013, Bayesian Data Analysis, Third Edition. Chapman & Hall/CRC Texts in Statistical Science, Taylor & Francis

Gieles M., Zocchi A., 2015, MNRAS, 454, 576

Gieles M., Balbinot E., Yaaqib R. I. S. M., Hénault-Brunet V., Zocchi A., Peuten M., Jonker P. G., 2018, MNRAS, 473, 4832

Giersz M., Heggie D. C., 1994, MNRAS, 268, 257

Giersz M., Leigh N., Hypki A., Lützgendorf N., Askar A., 2015, MNRAS, 454, 3150

Gilmore G., et al., 2012, The Messenger, 147, 25

Gomez-Leyton Y. J., Velazquez L., 2014, Journal of Statistical Mechanics: Theory and Experiment, 2014, 04006

Goodman J., Binney J., 1984, MNRAS, 207, 511

Goodman J., Weare J., 2010, Communications in Applied Mathematics and Computational Science, 5, 65

Göttgens F., et al., 2021, MNRAS, 507, 4788

Gratton R., Bragaglia A., Carretta E., D'Orazi V., Lucatello S., Sollima A., 2019, A&ARv, 27, 8

Greene J. E., Strader J., Ho L. C., 2020, ARA&A, 58, 257

Gross D. H. E., Ecker A., Zhang X. Z., 1996, arXiv e-prints, pp cond–mat/9607150

Gunn J. E., Griffin R. F., 1979, AJ, 84, 752

Haario H., Saksman E., Tamminen J., 2001, Bernoulli, 7, 223

Harris W. E., 1996, AJ, 112, 1487

Heggie D. C., 2014, MNRAS, 445, 3435

Heggie D., Hut P., 2003, The Gravitational Million Body Problem: A Multidisciplinary Approach to Star Cluster Dynamics. Cambridge University Press, Cambridge, UK

Heggie D. C., Mathieu R. D., 1986, in Hut P., McMillan S. L. W., eds, , Vol. 267, The Use of Supercomputers in Stellar Dynamics

Hénault-Brunet V., Gieles M., Sollima A., Watkins L. L., Zocchi A., Claydon I., Pancino E., Baumgardt H., 2019, MNRAS, 483, 1400

Hénault-Brunet V., Gieles M., Strader J., Peuten M., Balbinot E., Douglas K. E. K., 2020, MNRAS, 491, 113

Hunter C., 1977, AJ, 82, 271

Hunter C., 2001, MNRAS, 328, 839

Huntley J. M., Saslaw W. C., 1975, ApJ, 199, 328

Jindal A., Webb J. J., Bovy J., 2019, MNRAS, 487, 3693

Kamann S., et al., 2017, MNRAS, 473, 5591

Kamann S., et al., 2020, MNRAS, 492, 966

Katz J., 1980, MNRAS, 190, 497

King I. R., 1966, AJ, 71, 64

Kızıltan B., Baumgardt H., Loeb A., 2017, Nature, 542, 203

Kuzma P. B., Ferguson A. M. N., Varri A. L., Irwin M. J., Bernard E. J., Tolstoy E., Peñarrubia J., Zucker D. B., 2022, MNRAS, 512, 315

Landau L., Lifshitz E., 1976, Mechanics: Volume 1. Course of theoretical physics, Elsevier Science

Landau L., Lifshitz E., 2013, Statistical Physics: Volume 5. No. v. 5, Elsevier Science

Lanzoni B., et al., 2013, ApJ, 769, 107

Leanza S., et al., 2023, ApJ, 944, 162

Lee M. H., Goodman J., 1989, ApJ, 343, 594

Libralato M., et al., 2018, ApJ, 861, 99

Lützgendorf N., Kissler-Patig M., Noyola E., Jalali B., de Zeeuw P. T., Gebhardt K., Baumgardt H., 2011, A&A, 533, A36

Lynden-Bell D., 1967, MNRAS, 136, 101

MacKay D., 2003, Information Theory, Inference and Learning Algorithms. Cambridge University Press

Mackey A. D., Wilkinson M. I., Davies M. B., Gilmore G. F., 2008, MNRAS, 386, 65

Mancino A., Ciotti L., Pellegrini S., Giannetti F., 2023, MNRAS, 527, 9904

Mapelli M., 2017, MNRAS, 467, 3255

McLaughlin D. E., van der Marel R. P., 2005, ApJS, 161, 304

Merritt D., 1985, AJ, 90, 1027

Merritt D., Milosavljević M., Favata M., Hughes S. A., Holz D. E., 2004, ApJ, 607, L9

Meylan G., Mayor M., 1991, A&A, 250, 113

Meylan G., Mayor M., Duquennoy A., Dubath P., 1995, A&A, 303, 761

Michie R. W., 1963, MNRAS, 125, 127

Milne E. A., 1923, MNRAS, 83, 118

Miocchi P., 2006, MNRAS, 366, 227

Miocchi P., 2007, MNRAS, 381, 103

Miocchi P., 2010, A&A, 514, A52

Miocchi P., et al., 2013, ApJ, 774, 151

Monaghan J. J., Roxburgh I. W., 1965, MNRAS, 131, 13

Norris M. A., et al., 2014, MNRAS, 443, 1151

Noyola E., Gebhardt K., Bergmann M., 2008, ApJ, 676, 1008

Olver F. W. J., et al., 2022, NIST Digital Library of Mathematical Functions, http://dlmf.nist.gov/, Release 1.1.5, `http://dlmf.nist.gov/`

Pallanca C., et al., 2021, ApJ, 913, 137

Pallanca C., et al., 2023, ApJ, 950, 138

Peterson C. J., King I. R., 1975, AJ, 80, 427

Peuten M., Zocchi A., Gieles M., Gualandris A., Hénault-Brunet V., 2016, MNRAS, 462, 2333

Plummer H. C., 1911, MNRAS, 71, 460

Portegies Zwart S. F., Baumgardt H., Hut P., Makino J., McMillan S. L. W., 2004, Nature, 428, 724

Prendergast K. H., Tomer E., 1970a, The Astronomical Journal, 75, 674

Prendergast K. H., Tomer E., 1970b, AJ, 75, 674

Robert C., 2007, The Bayesian Choice: From Decision-Theoretic Foundations to Computational Implementation. Springer Texts in Statistics, Springer New York

Roberts G. O., Rosenthal J. S., 2009, Journal of Computational and Graphical Statistics, 18, 349

Schwarzschild M., 1979, ApJ, 232, 236

Sellwood J. A., 2024, MNRAS, 529, 3035

Smith B. L., 1975, Ap&SS, 35, 223

Sollima A., 2020, MNRAS, 495, 2222

Sollima A., Bellazzini M., Smart R. L., Correnti M., Pancino E., Ferraro F. R., Romano D., 2009, MNRAS, 396, 2183

Sollima A., Baumgardt H., Zocchi A., Balbinot E., Gieles M., Hénault-Brunet V., Varri A. L., 2015, MNRAS, 451, 2185

Sollima A., Baumgardt H., Hilker M., 2019, MNRAS, 485, 1460

Spitzer Lyman J., 1969, ApJ, 158, L139

Strader J., Chomiuk L., Maccarone T. J., Miller-Jones J. C. A., Seth A. C., Heinke C. O., Sivakoff G. R., 2012, ApJ, 750, L27

Tassoul J.-L., 1978, Theory of rotating stars. Princeton University Press

Tessore N., 2022, flt: Fast Legendre transform, `https://pypi.org/project/flt/`

Tiongco M. A., Vesperini E., Varri A. L., 2015, MNRAS, 455, 3693

Tiongco M. A., Vesperini E., Varri A. L., 2016, MNRAS, 461, 402

Tiongco M. A., Vesperini E., Varri A. L., 2017, MNRAS, 469, 683

Trager S. C., King I. R., Djorgovski S., 1995, AJ, 109, 218

Tremaine S., Richstone D. O., Byun Y.-I., Dressler A., Faber S. M., Grillmair C., Kormendy J., Lauer T. R., 1994, AJ, 107, 634

Tremou E., et al., 2018, ApJ, 862, 16

Van Dyke M., 1975, Perturbation methods in fluid mechanics. Parabolic Press, Stanford, CA, USA

Van Hese E., Baes M., Dejonghe H., 2011, ApJ, 726, 80

Vandervoort P. O., 1980, ApJ, 240, 478

Varri A. L., Bertin G., 2012, A&A, 540, 24

Vasiliev E., Baumgardt H., 2021, MNRAS, 505, 5978

Vesperini E., Varri A. L., McMillan S. L. W., Zepf S. E., 2014, MNRAS, 443, L79

Virtanen P., et al., 2020a, Nature Methods, 17, 261

Virtanen P., et al., 2020b, Nature Methods, 17, 261

Vitral E., Libralato M., Kremer K., Mamon G. A., Bellini A., Bedin L. R., Anderson J., 2023, MNRAS, 522, 5740

Volonteri M., 2010, A&ARv, 18, 279

Volonteri M., 2012, Science, 337, 544

Wang L., Spurzem R., Aarseth S., Nitadori K., Berczik P., Kouwenhoven M. B. N., Naab T., 2015, MNRAS, 450, 4070

Webb J. J., Leigh N. W. C., Serrano R., Bellovary J., Ford K. E. S., McKernan B., Spera M., Trani A. A., 2019, MNRAS, 488, 3055

Wen R. Y., Speagle J. S., Webb J. J., Eadie G. M., 2024, MNRAS, 527, 4193

Wilson C. P., 1975, AJ, 80, 175

Woolley R. V. D. R., 1954, MNRAS, 114, 191

Wrobel J. M., Nyland K. E., 2020, ApJ, 900, 134

Young P., 1980, ApJ, 242, 1232

Zocchi A., Gieles M., Hénault-Brunet V., Varri A. L., 2016, MNRAS, 462, 696

Zocchi A., Gieles M., Hénault-Brunet V., 2017, MNRAS, 468, 4429

Zocchi A., Gieles M., Hénault-Brunet V., 2019, MNRAS, 482, 4713 de Boer T. J. L., Gieles M., Balbinot E., Hénault-Brunet V., Sollima A., Watkins L. L., Claydon I., 2019, MNRAS, 485, 4906

van Albada T. S., 1982, MNRAS, 201, 939

van de Ven G., van den Bosch R. C. E., Verolme E. K., de Zeeuw P. T., 2006, A&A, 445, 513

van den Bosch R., de Zeeuw T., Gebhardt K., Noyola E., van de Ven G., 2006, ApJ, 641, 852

van der Marel R. P., Anderson J., 2010, ApJ, 710, 1063